UNIVERSITY OF CALIFORNIA
SANTA CRUZ

MULTIFERROCITY IN FLUOROPEROVSKITE THIN FILMS

A dissertation submitted in partial satisfaction of the
requirements for the degree of

DOCTOR OF PHILOSOPHY

in

PHYSICS

by

Amit KC

March 2018

The Dissertation of Amit KC
is approved:

Professor David Lederman, Chair

Professor David P. Belanger

Professor Frank (Bud) Bridges

Dean Tyrus Miller
Vice Provost and Dean of Graduate Studies

Table of Contents

List of Figures

List of Tables

Abstract

Multiferrocity in fluoroperovskite Thin Films

by

Amit KC

Recent computational work predicted orthorhombic antiferromagnetic $NaMnF_3$ to undergo a ferroelectric transition if an a = c structural distortion is imposed. Such a distortion may be achieved by epitaxial growth of $NaMnF_3$ on a cubic substrate in thin film form. It has been shown that the a = c distortion leads to the freezing of a soft polar mode resulting in a structural transformation from a non-polar *Pnma* to a polar $Pna2_1$ space group with a polarization of $P = 6\ \mu$ C/cm^2 along the long axis. A weak ferromagnetic phase and an amplification of magnetoelectric coupling are also expected in the strained films, with a magnetoelectric response comparable to Cr_2O_3.

In this work, I investigate multiferroicity in $NaMnF_3$ thin films. Epitaxial $NaMnF_3$ thin films were grown on cubic $SrTiO_3$ (001) single crystal substrates via molecular beam epitaxy (MBE). Thin film structural quality was investigated as a function of the substrate temperature and film thickness using X-ray diffraction (XRD), *in-situ* reflection high-energy electron diffraction (RHEED), and atomic force microscopy (AFM). The best films were smooth single phase grown at $250 - 300$ °C substrate temperatures with four different twin domains. In-plane magnetization measurements using a superconducting quantum interference device (SQUID) magnetometer revealed antiferromagnetic ordering with weak ferromagnetism below the Neel temperature $T_N = 66$ K. Reproducible room temperature ferroelectric switching by a

voltage-biased scanning probe was detected with preferred up (out-of-plane) polarization using piezoresponse force microscopy. An interesting 180° out-of-plane polarization flip by the application of an in-plane electric field was also observed.

For the exchange bias and dielectric studies, $NaMnF_3$ films were grown on 30 nm $SrRuO_3$ (001) layer, which was used as a ferromagnetic layer as well as a bottom electrode, and grown *via* pulsed laser deposition. After field cooling below the Neel temperature of $NaMnF_3$, hysteresis loops were measured as the function of temperature. A negative exchange bias was found with the blocking temperature (T_B) $\sim$ 45 K. The complex permittivity as a function of frequency measurements indicated a strong Debye-like relaxation. A power-law divergence of the characteristic relaxation time revealed an order-disorder phase transition at 8 K.

Acknowledgments

I would like to thank my advisor, Professor David Lederman, for his help throughout the graduate school. The discussions I had with him on the variety of topics have always been the source of guidance to me.

I would also like to thank Dr. Pavel Borisov who was always there for me whenever I needed help. We had many fruitful conversations on variety of subjects. I need to thank Professor Aldo Romero and Dr. Andrés C. Garcia-Castro for their theoretical works which provided the foundation for this dissertation, and the discussions we had were instrumental in driving the $NaMnF_3$ project forward. I am also grateful to our collaborators Professor Cheng Cen and Dr. Ming Yang for preforming and analyzing PFM measurements of the samples. I also have to thank Dr. Vladimir Shvartsman who help us interpret the dielectric measurements. Thanks to my colleagues, including Trent Johnson, Sercan Babakiray, Toyanth Joshi and Sophie Morley, with all of whom I often had insightful conversations.

I must thank my parents and family. My family's support has kept me inspired and motivated throughout the graduate school. I must also thank my wife, Binita, who has always been there for me.

Chapter 1

Introduction and Motivation

In recent decades, there has been a revival of interest [1] in the study of multifunctional materials where the same material shows different electronic or physical properties. Multiferroics constitute one of the most extensively studied multifunctional materials. In multiferroics, two or more long-range order co-exist: ferroelectricity, (anti-) ferromagnetism and/or ferroelasticity. The presence of simultaneous magnetic and dielectric orders provides flexibility in terms of possible applications. Magnetoelectric coupling can also allow for the control of magnetization $\mathbf{M}$ (electric polarization $\mathbf{P}$) using an electric field $\mathbf{E}$ (a magnetic field $\mathbf{H}$), which can be used for potential applications in efficient data storage, sensors and spintronic devices [1–5].

To date much of the effort has been directed towards engineering multiferroic oxides. However, there are other families of multiferroic materials such as fluorides that also have interesiting properties. For example, in the orthorhombic $BaMF_4$ family the M = Co and Ni compounds in bulk form are ferroelectric and antiferromagnetic [6]. While in most oxide perovskites ABO_3, the simultaneous presence of ferroelectric and

magnetic orderings is limited by conflicting requirements for the d^n electronic configuration of the transition metal in the B-site [7], ferroelectricity in $BaMnF_4$ is mainly due to geometric (topological) reasons [8]. Recent experiments showed that $BaCoF_4$ thin films are weakly ferromagnetic at low temperatures due to strain [9].

$NaMnF_3$ has an orthorhombic perovskite crystal structure and belongs to the *Pnma* space group. At room temperature, the lattice constants are $a_o = 5.751$ Å, $b_o = 8.008$ Å, and $c_o = 5.548$ Å [10]. The structure is distorted from the ideal cubic perovskite crystal structure due to the rotation and tilts of the MnF_6 octahedra. The bulk of $NaMnF_3$ has non-polar centrosymmetric ground state because the antiferrodistortive instability corresponding to the rotation and tilts of the MnF_6 octahedra dominates over weaker polar instabilities. However, recent computational work predicted a ferroelectric instability in $NaMnF_3$ originating from Na displacements (the A-site perovskite cation in the ABF_3 structure) (see figure 1.1). Computational work assuming that a cubic substrate forces the a and c lattice parameters to be equal to each other has shown that the soft polar mode B_{2u} freezes, resulting in a transformation to the polar $Pna2_1$ space group which causes a polarization of $P = 6$ $\mu C/cm^2$ along the long axis b [11]. Computational results also indicate that P can be enhanced by negative or positive strains (12 μCcm^2 at +5% strain 9 $\mu C/cm^2$ at −5% strain) [11, 12]. A weak ferromagnetic phase and amplification of magnetoelectric (ME) coupling are also expected in the strained films, with a ME response comparable to Cr_2O_3 (multiferroicity and magnetoelectricity in $NaMnF_3$ are discussed in depth in the introduction of chapter 4) [12]. Therefore, NMF is an attractive possibly ME material because its ferroelectricity can be modulated by strain and is not subject

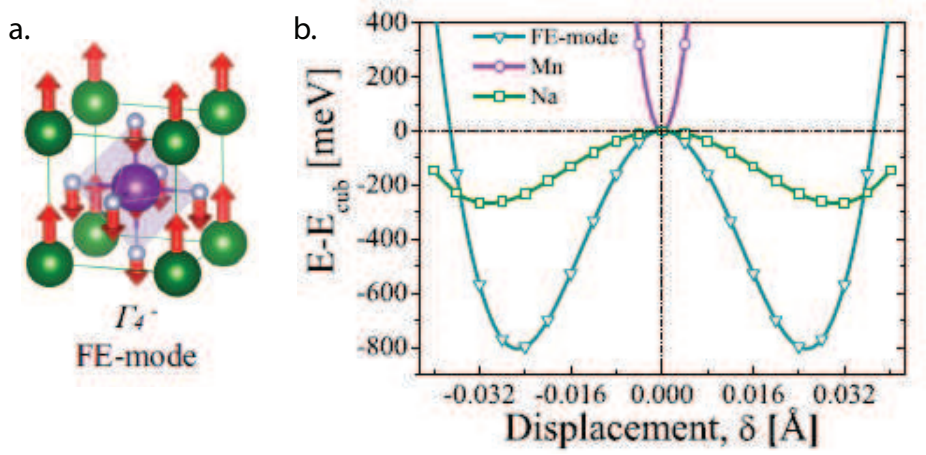

Figure 1.1: First principle calculation on $NaMnF_3$. (a) Ferroelectric soft mode (b) Energy as a function of displacement for NaMnF3 with a G-type antiferromagnetic order in each unit cell (color code: Na green, Mn purple, and F white spheres). Reproduced from references [11].

to the d^n rule because there is no displacement of the Mn ion from the center of the MnF_6 octahedra.

As an experimentalist, my task was to verify multiferrocity of $NaMnF_3$ in thin film form. Films with different thicknesses $NaMnF_3$ were grown on cubic $SrTiO_3$ substrate (a_{SrTiO_3} = 3.905 Å). As mentioned above, the growth of $NaMnF_3$ on a cubic substrate would most likely create epitaxial isotropic strain in-plane leading to $a = c$ distortion. This distortion is the key ingredient in $NaMnF_3$ that induces a soft ferroelectric mode.

My initial work focuses on structural, magnetic and electrical characterization of the bare $SrTiO_3$ substrates that were obtained per-polished. Using a superconducting quantum interference device (SQUID) magnetometer, zero-field cooled, field-cooled and thermo-remenant magnetizations were measured. The in-plane (electric field applied in-plane of the substrate surface) dielectric polarization as a function of an

electric field ($P - E$) of a single crystal $SrTiO_3$ substrate were measured at low temperature. In pure form $SrTiO_3$ is a well-known quantum paraelectric material. Another term that is commonly used to describe quantum paraelectric materials is incipient ferroelectrics because quantum fluctuation suppress the ferroelectric transition in such materials [13, 14]. However, in-plane $P - E$ loops were measured at low temperature in bare $SrTiO_3$ substrates with a saturation polarization of approximately 0.6 $\mu C/cm^2$ suggesting ferroelectric or relaxor ferroelectric nature. The likely origin of the polar nature in the substrates is speculated in the section 4.1.1. Further research is required to fully understand the origin of polar nature in these $SrTiO_3$ substrates. In practical terms, this means we can't measure an in-plane $P - E$ loops to explore ferroelectric polarization in the $NaMnF_3$ thin film unless the polarization is significantly higher than what is observed on the bare $SrTiO_3$ substrates.

To the best of our knowledge, $NaMnF_3$ has not been grown previously in thin film form. Therefore, in this work, the optimal growth condition is determined *via* X-ray diffraction (XRD), atomic force microscopy (AFM) and *in-situ* reflection high energy electron diffraction (RHEED). The best films were further structurally and magnetically characterized. Off-axis XRD scans and reciprocal space mapping were used to determine different $NaMnF_3$ domains present in the film as well as their lattice parameters while SQUID magnetometry was used to determine the magnetic nature of the film. Piezoresponse force microscopy was used to explore ferroelectric polarization in response to external and built-in electric fields.

For exchange bias and dielectric characterizations, $NaMnF_3$ films were grown on a 30 nm $SrRuO_3$ (001) layer used as a ferromagnetic layer as well as a bottom electrode

grown via pulsed laser deposition. After cooling down below the Néel temperature of $NaMnF_3$ in a field, magnetic hysteresis loops as a function of temperature were measured. Exchange bias field and blocking temperature of the system were investigated. For ferroelectric characterization, $P - E$ loops were measured at low temperatures which showed closed loops. However, there was absence of saturation polarization and a concave region in the loops. Materials with such "hysteresis loops" cannot be interpreted as ferroelectrics without further characterizations [15]. Next, dielectric spectroscopy was performed on the material. The real and imaginary parts of the dielectric constant were measured at different frequencies from room temperature to 10 K. An analysis of the complex permittivity revealed strong Debye-like relaxation contribution characterized by a distribution of relaxation times. Further analysis to understand the driving mechanism of the relaxation was carried out using Arrhenius, Vogel-Fulcher, and power law models.

Chapter 2

Background

2.1 Magnetization and Magnetic Susceptibility

Magnets have been used by people for over 2000 years since the discovery by the ancient Chinese of a special needle made from "lodestone" that points north-south when suspended. However, the true origin of the magnetism was unclear until the formulation of quantum mechanics. It is now understood that electronic phenomena which are "non-classical" play a critical role in nearly all magnetic effects in solids. Specifically, the electron's spin degree of freedom along with its orbital angular momentum is responsible for the magnetic moments in materials. Nuclear spins can also give rise to magnetic moments, but in general, they are weak in comparison to the magnetic moment of the electrons.

The magnetization $\mathbf{M}$ is the measure of magnetic dipole moment per unit volume. In electromagnetism, the relationship between $\mathbf{M}$, magnetic field, $\mathbf{H}$, and magnetic

induction, $\mathbf{B}$, is given by

$$M_i = \sum_{j=1}^{3} \chi_{ij} H_j \Longrightarrow B_i = \sum_{j=1}^{3} \mu_{ij} H_j = \mu_0 \sum_{j=1}^{3} (\delta_{ij} + \chi_{ij}) H_j, \tag{2.1}$$

where the proportionality constant μ_{ij} and χ_{ij} are magnetic permeability and susceptibility tensors, respectively, and μ_0 is magnetic permeability of free space. In the case of isotropic media, we may simply write

$$\mathbf{M} = \chi \mathbf{H} \Longrightarrow \mathbf{B} = \mu \mathbf{H} = \mu_0 (1 + \chi) \mathbf{H}. \tag{2.2}$$

Although χ is a dimensionless quantity, quite frequently, it is expressed in terms of $\mathrm{cm}^3\mathrm{mol}^{-1}$ (molar susceptibility), $\mathrm{cm}^3\mathrm{gm}^{-1}$ (mass susceptibility), and emu (volume susceptibility). In general, the magnetic response is rather weak ($\chi = \mathbf{M}/\mathbf{H} \sim 10^{-5}$) with the exception of ferromagnets. Moreover, thin films often have small magnetization signal. In such case, the magnetic moment is often expressed in units of Bohr magnetons per atomic site or unit cell, μ_B ($\mu_B = \frac{e\hbar}{2m_e} = 9.274 \times 10^{-21}$ erg/Oe). Diamagentic materials with $\chi < 0$ tend to repel magnetic flux. Paramagnetic materials with $\chi > 0$ tend to gather flux.

2.2 Magnetic order

Most of the materials found in nature do not show a presence of magnetic moment in the absence of an external magnetic field and are either diamagnetic or paramagnetic. However, there is a small subclass of magnetic materials that show spontaneous magnetic order. Such phenomena are classified as ferromagnetism and antiferromagnetism. For the most part, the electronic arrangements determine the magnetic nature

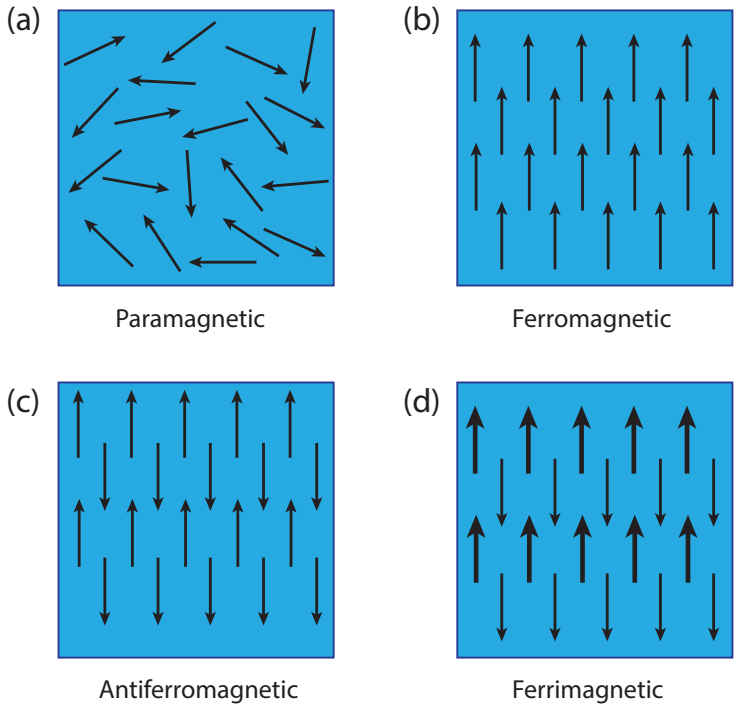

Figure 2.1: Different types of magnetic ordering in the materials. Arrows indicate magnetic dipole orientation. Inspired by reference [16].

of the atoms. Closed atomic orbitals have equal numbers of spin up and spin down electrons which result in diamagnetism, such as in noble gases. Similarly, if the outermost orbital electrons (valence electrons) are completely involved in the chemical bonding (covalent or ionic bond) then again atoms/ions become diamagnetic.

The interaction energy between the external field and a magnetic dipole is given by

$$U = -\boldsymbol{\mu} \cdot \mathbf{H}. \tag{2.3}$$

Due to such interaction with the external field, a non-interacting magnetic moment tends to align in the direction of the field. Such phenomenon is known as paramagnetism (figure 2.1(a)). All the materials that show paramagnetism normally follow

Curie's law [17–19] which is stated as:

$$\chi(T) = \frac{M(T)}{H} = \frac{C}{T}. \tag{2.4}$$

Here C ($\equiv \mathrm{N}\mu^2 \ /3k_B$ where N is the number of moments per unit volume) is known as the Curie constant.

2.2.1 Ferromagnetism, Antiferromagnetism and the Exchange Interaction

Many materials have interacting magnetic moments that can give rise to spontaneous magnetization. Based on the neighboring moment's interaction, the materials can be classified into ferromagnets, antiferromagnets, and ferrimagnets as shown in figure 2.1. In 1928, Heisenberg showed that the exchange interaction is the result of quantum mechanical phenomena and does not have a classical counterpart.

The origin of the exchange interaction can be understood by taking a simple example of two hydrogen atoms each with a single electron on outer shell. First, we can consider the wave function for a 2-electron system by multiplying the spatial and spin parts:

$$\Psi(1,2) = \psi(\mathbf{r}_1, \mathbf{r}_2)\chi(1,2) \tag{2.5}$$

where the subscripts 1 and 2 refer to the two electrons, $\psi(\mathbf{r}_1, \mathbf{r}_2)$ refers to spatial wave function without spin and χ refers to the spin wave function. The spatial wave function can have the following forms:

$$Symmetric : \psi_s(1,2) = \frac{1}{\sqrt{2}}[\phi_1(\mathbf{r}_1)\phi_2(\mathbf{r}_2) + \phi_1(\mathbf{r}_2)\phi_2(\mathbf{r}_1)] \tag{2.6}$$

$$Antisymmetric : \psi_a(1,2) = \frac{1}{\sqrt{2}}[\phi_1(\mathbf{r}_1)\phi_2(\mathbf{r}_2) - \phi_1(\mathbf{r}_2)\phi_2(\mathbf{r}_1)] \tag{2.7}$$

Electrons as fermions have an antisymmetric wave functions. Therefore, it may take either of the two forms (this is just another way of stating Pauli Exclusion principle):

$$\psi_i = \psi_s(1,2)\chi_a(1,2) \tag{2.8}$$

or

$$\psi_{ii} = \psi_a(1,2)\chi_s(1,2) \tag{2.9}$$

where χ_a is valid for electrons with antiparallel spin ($S = 0$, singlet state) and χ_s is when electrons spin is parallel ($S = 1$, triplet states). In this case, the interaction potential between the two atoms of the hydrogen, whose nuclei are designated by u and v, is given by the Hamiltonian

$$\hat{H}_{12} = \frac{e^2}{r_{uv}} + \frac{e^2}{r_{12}} - \frac{e^2}{r_{1v}} - \frac{e^2}{r_{2u}}, \tag{2.10}$$

where r_{uv} and r_{12} are the distances between the nuclei and electrons respectively, and r_{1v} and r_{2u} are distances between the nucleus and the electron. The energies can be obtained as follows:

$$E_i = A^2(K_{12} + J_{12}) \tag{2.11}$$

and

$$E_{ii} = B^2(K_{12} - J_{12}) \tag{2.12}$$

where

$$K_{12} = \int d^3r_1 d^3r_2 \phi_1^*(\mathbf{r}_1)\phi_2^*(\mathbf{r}_2)\hat{H}\phi_1(\mathbf{r}_1)\phi_2(\mathbf{r}_2), \tag{2.13}$$

$$J_{12} = \int d^3r_1 d^3r_2 \phi_1^*(\mathbf{r}_1)\phi_2^*(\mathbf{r}_2)\hat{H}\phi_1(\mathbf{r}_2)\phi_2(\mathbf{r}_1), \tag{2.14}$$

with A and B being normalization constants. K_{12} is called the direct Coulomb integral or Coulomb interaction energy and J_{12} is called the exchange integral [20].

The energies in expressions 2.11 and 2.12 can be rewritten in the operator form that expands to the whole material, not just neighboring sites but we are interested only in the spin-dependent term. The exchange Hamiltonian that models such interaction between the neighboring moments with spin operators $\hat{S}_i$ and $\hat{S}_j$ is given by

$$\hat{H} = -2\sum_{i,j} J_{ij}\hat{S}_i \cdot \hat{S}_j, \tag{2.15}$$

where the exchange constant J_{ij} measures the strength of exchange interaction between the magnetic sites [20]. On the other hands, the exchange Hamiltonian for short-range interaction limiting to nearest neighbors is

$$\hat{H} = -2\sum_{i}^{n}\sum_{j}^{u} J\hat{S}_i \cdot \hat{S}_j. \tag{2.16}$$

Here n is the total number of magnetic sites, and u is the number of nearest neighbors. J originates from the overlap of two electrons wave functions. Consequently, the sign of J represents important intrinsic phenomena: if J is positive, the exchange energy is lowest when there is a parallel alignment of the moments hence the material exhibits ferromagnetic behavior (figure 2.1 (b)). If J is negative, the exchange energy is lowest when there is an antiparallel alignment of the moments hence the material exhibits antiferromagnetic behavior (figure 2.1 (c)). However, such magnetic ordering disappears above some critical temperature which is designated by the Curie temperature (T_c) for a ferromagnet and the Néel temperature (T_N) for an antiferromagnet. Almost all the magnetic materials are paramagnetic above their critical temperature, and their susceptibility essentially follows the **Curie law**, Eq. 2.4. Hence, a simple

modified model of **Curie law** can be used to represent the magnetic susceptibility above the T_c. Such modification comes naturally in both ferromagnets and antiferromagnets due to the presence of a an effective exchange field H_E (intermolecular exchange interaction) as argued by P. Weiss (1907). The model is known as the **Curie-Weiss law** [19,20] where the magnetic susceptibility for ferromagnets is given by:

$$\chi = \frac{C}{T - T_C}. \tag{2.17}$$

Equation 2.17 satisfactorily describes the experimentally measured susceptibility of a ferromagnet for $T > T_C$. Similarly, the magnetic susceptibility for an antiferromagnet is given by:

$$\chi = \frac{C}{T + T_N}, \tag{2.18}$$

due to negative intermolecular exchange interaction between the neighboring magnetic sites.

Ferromagnets can retain memory once the applied external magnetic field is removed. Due to such a "memory effect", the measurement of magnetization as a function of external magnetic field shows hysteretic behavior and the curve obtained is called a hysteresis loop. A typical hysteresis loop of a ferromagnetic material is shown in figure 2.2. The dotted line is the initial magnetization curve. On increasing the magnetic field, the magnetization reaches its saturation, M_s. On subsequent decreasing of the magnetic field, the curve does not follow its initial magnetization curve and at $H = 0$, there is an offset from the origin called remanence magnetization, M_r. The magnetization of these kinds of materials generally goes to zero at $\pm H$ called coercive field, H_c.

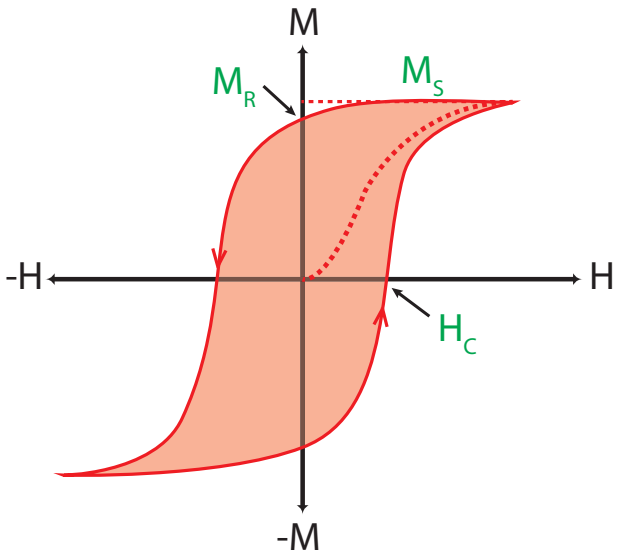

Figure 2.2: Typical hysteresis loop of a ferromagnetic material.

2.2.2 Classification of Antiferromagentism

In a complex system such as a perovskite crystal, there can exist different classes of antiferromagnetism. Most of the antiferromagnetic material can be classified into three classes: A-, C-, and G-type. B-type is regarded as a class with ferromagnetic ordering [21]. In the case of A-type, inter-planer spin ordering is antiferromagnetically aligned while intra-planar is ferromagnetically aligned. In the case of C-type, inter-planer spin ordering is ferromagnetically aligned while intra-planar is antiferromagnetically aligned. And in the case of G-type, both inter-, and intra-planar spin ordering is antiferromagnetically aligned. Different types of magnetic spin orderings are shown in figure 2.3.

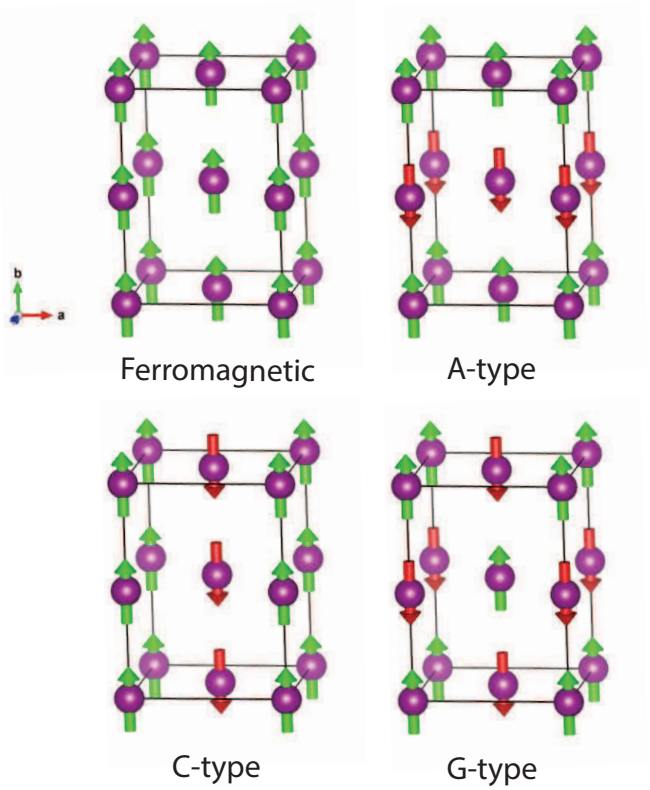

Figure 2.3: Types of spin ordering in perovskite oxides/fluorides. Inspired by reference [21].

2.2.3 Magnetic Anisotropy

Magnetism arises from the exchange interaction between interacting electrons which is independent of the direction along which magnetization aligns. However, it has been experimentally found that magnetism often depends on the direction of the applied magnetic field. Such an anisotropic effect is due to the electron spin degree of the freedom coupled with its spatial direction, also called spin-orbit coupling, $H_{SO} \propto \mathbf{L} \cdot \mathbf{S}$. The spin-orbit coupling tends to align magnetization along specific crystallographic axes or easy axes; such a phenomenon is known as magnetic anisotropy. The energy that directs such alignment is called magnetocrystalline anisotropy en-

ergy (MAE). MAE is responsible for many magnetic properties such as magnetic hardness and softness, magnetic domain wall structure, magnetic nanostructure (e.g., skyrmion), and transport properties (e.g., sping-orbit torque, anomalous hall effect).

In general, anisotropy energy can be expanded into power series of direction cosines (α_1, α_2 and α_3) relative to the crystal axes:

$$E_{crystal}(\mathbf{M}) = b_0 + \sum_{i=1}^{3} b_i \alpha_i + \sum_{i,j=1}^{3} b_{i,j} \alpha_i \alpha_j + \sum_{i,j,k=1}^{3} b_{i,j,k} \alpha_i \alpha_j \alpha_k + ... \tag{2.19}$$

From the equation 2.19, the energy contribution related to magnetization direction in different system can be obtained, for example, in a cubic system it takes a form,

$$E_{crystal}(\mathbf{M}) = K_0 + K_1(\alpha_1^2\alpha_2^2 + \alpha_2^2\alpha_3^2 + \alpha_3^2\alpha_1^2) + K_2\alpha_1^2\alpha_2^2\alpha_3^2 \tag{2.20}$$

where coefficients K_0, K_1, K_2... are the linear combination of tensor components of b. Usually, the anisotropy energy is dependent on the temperature. Therefore, coefficients are permitted to vary with temperature to account for such temperature dependence of anisotropy energy.

2.2.4 Antisymmetric Exchange

In some antiferromagnetic materials, there is a presence of weak ferromagnetism due to spin canting (see figure 2.4) such as in α-Fe_2O_3 between $263 < T < 945$ K [22]. Dzialoshinsky proposed that spin canting is possible between the neighboring spins, $\mathbf{S}_i$ and $\mathbf{S}_j$, when there is antiparallel spins alignment [23]. The interaction can be expressed by

$$H_{DM} = \mathbf{D} \cdot (\mathbf{S}_i \times \mathbf{S}_j), \tag{2.21}$$

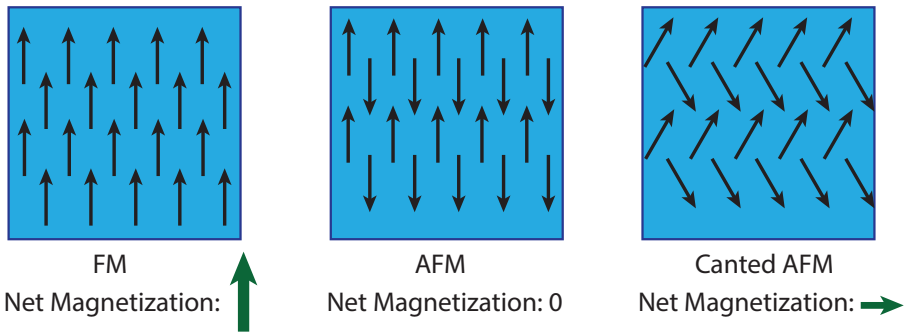

Figure 2.4: Ferromagnetic (FM), antiferromagnetic (AFM), and canted AFM moment spin configurations. Black arrows show the magnetic dipole orientation and green arrows show the direction of net magnetization.

where the constant vector **D** is constrained by symmetry. Later Moriya explained the origin of spin canting by two mechanisms [24, 25]. The first mechanism involves crystalline field along with spin-orbit coupling acting on nonequivalent sites. The second one involves the spin-orbit coupling and the superexchange interaction (the magnetic interaction between two neighboring ions transferred via a third ligand). The expression 2.21, therefore, is also called Dzialoshinskii-Moriya Interaction.

2.2.5 Exchange Bias

Exchange bias is the exchange interaction at the interface of a ferromagnet (FM) and an antiferromagnet (AFM). It was first observed by Meiklejohn and Bean in ferromagnetic Co particle with partially oxidized CoO shell [26]. After a FM-AFM system is cooled in the field below the Néel temperature of AFM, there is a horizontal shift (generally in a negative field) of the hysteresis loop from its usual center around zero field. This phenomenon is called exchange bias or exchange anisotropy (please refer to figure 2.5 for the schematic representation). However, the effect disappears

near the Néel temperature of the AFM confirming the role of AFM layer in such anisotropic behavior [26–28].

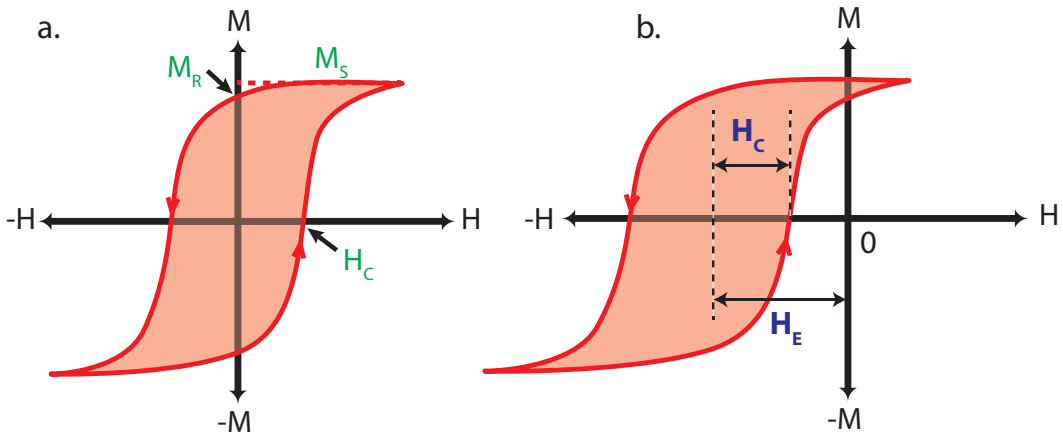

Figure 2.5: Schematic diagrams showing hysteresis loop in FM (a) and exchange anisotropy in a FM-AFM bilayer (b). Exchange bias is normally accompanied by an increase in the coercive field H_c.

Since its first discovery by Meiklejohn and Bean, exchange bias has been observed in many systems as such small particles: Ni-NiO [29], Fe-FeO [30], and FeCo-FeCoO [31], inhomogenous materials: $Fe_{1-x}Zr_x$ [32], and thin film bilayers such as FeF_2-Fe [33] and NiMn-NiFe [34]. Excahnge bias has a lot of technological applications including but not limited to magnetic recording [35], spin valves [36] and random access memory [37].

Figure 2.6 is the schematic representation of exchange bias showing exchange interaction between the spins of FM and AFM. When the FM-AFM system is in $T_N < T < T_C$ with the external field applied, the FM spins line up with field while AFM is still in its paramagnetic state (figure 2.6 (i)). After the system is cooled in the field below the Néel temperature, the first monolayer of the spins at AFM aligns parallel to the spins of FM at the interface. However, spins below the first

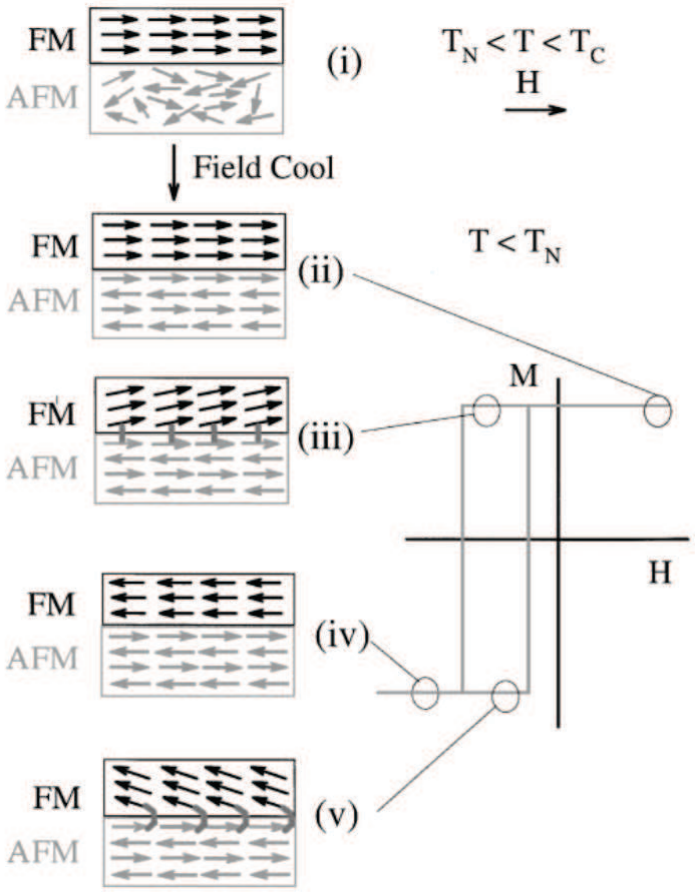

Figure 2.6: Schematic diagram of exchange bias on FM-AFM bilayer: (i) shows the case of $T_N < T < T_C$ where FM is magnetized below T_C while the AFM is paramagnetic (ii-v) show different stages of exchange bias hysteresis loop after field cool process usually below T_N. Reproduced from reference [28].

monolayer follows AFM spin order to minimize ground state energy with zero net magnetization. With the reversion of the external field, the FM spins start to rotate towards the field. However, due to AFM anisotropy, the spin in the AFM layer remains frozen until big enough field is applied to overcome the torque exerted by spin coupling at the interface. It also implies that FM spins have unidirectional anisotropy with one stable configuration. The unidirectional anisotropy behaves like

an internal biasing field which leads to the horizontal shift of the hysteresis loop along the field axis [26–28]. Exchange bias usually disappears above a certain temperature referred as the blocking temperature (T_B) which is usually close but below the Néel temperature of the AFM.

In the phenomenological approach of the exchange bias (the simplest case with the coherent rotation of the magnetization), FM anisotropy can be neglected (also supported by experiments), thus the energy per unit area of an exchange bias system can be written as [27, 28]:

$$E = -HM_{FM}t_{FM}\cos(\theta - \beta) + K_{AFM}t_{AFM}\sin^2(\alpha) - J_{int}\cos(\beta - \alpha) \tag{2.22}$$

where M_{FM} is the saturation magnetization, t_{FM} and t_{AFM} are the thickness of FM and AFM layers, K_{FM} and K_{AFM} is the anisotropy of FM and AFM layer respectively, and J_{int} is the interfacial coupling constant. β and α are the angles of magnetic rotation for FM and AFM respectively, and θ is the angle between the applied field and FM anisotropy. Minimizing the above relation 2.22 with respect to β and α yields:

$$H_E = \frac{J_{int}}{M_{FM}t_{FM}}. \tag{2.23}$$

This result indicates the shift in the hysteresis loop along the field axis. In most of the systems, it has been found that the exchange bias is roughly proportional the thickness of the FM layers [28] ($H_E \propto 1/t_{FM}$). However, such relation does not hold for a thinner (usually few nm) FMs, possibly due to discontinuous FM layer ([28] references within).

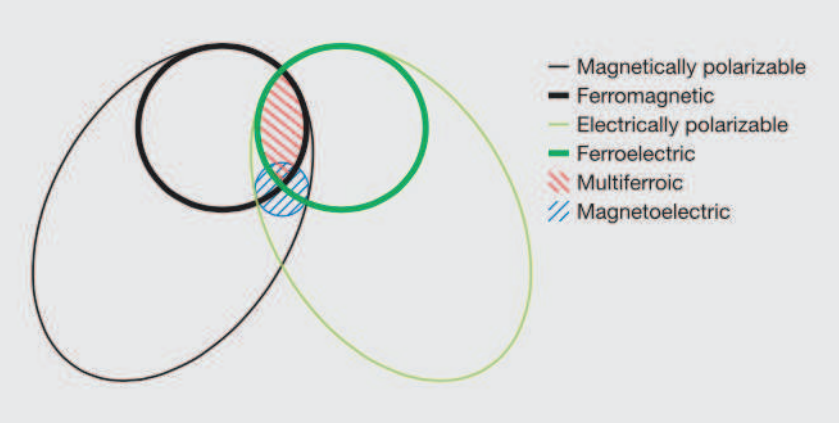

Figure 2.7: The relationship between multiferroic and magnetoelectric. Reproduced from reference [2].

2.3 Multiferroics

Ferroics [38] are the materials that show long-range order at a macroscopic level, hence forming domains with a peculiar orientation that can be switched by opposite field (e.g., ferromagntic, ferroelectric, and ferroelastic). While magnetism (including ferromagnetism) has been explored for more the 2000 years, ferroelectricity was only discovered in the last century [39]. Moreover, in the past 50-60 years, there has been much work aimed at understanding of both ferromagnetism and ferroelectricity. One of the expanding fields has been that of multiferroic.

The term multiferroic refers to the material that shows the coexistence of two or more long-range order parameters in a single- or multi-phase. This also includes antiferroic order (e.g., antiferromagnetism and antiferroelectism). Ferromagnetism and ferroelectricity can occur independently in material but have conflicting requirement [7] which is why multiferroics are rare in nature.

2.3.1 Ferroelectricity

Ferroelectricity is characterized by the presence of spontaneous polarization that can be switched with an external electric field. This phenomenon is analogous to ferromagnetism (e.g., Fe, Ni, Fe_2O_3) where the material shows a spontaneous magnetic dipole even in the absence of an external magnetic field as discussed in section 2.2.

Due to the spontaneous appearance of an electric dipole moment, a ferroelectric crystal breaks inversion symmetry. In other words, there is an absence of centrosymmetry in the crystal. There are 32 crystal classes of which 21 are non-centrosymmetric. Out of 21 non-centrosymmetric crystal, 20 exhibit the formation of an electric dipole under stress, such crystals are termed as piezoelectrics. Out of 20 piezoelectric crystal classes, 10 show spontaneous polarization or electric dipole moment; such properties are usually temperature dependent [40]. This class of materials is therefore referred as pyroelectrics. In the case of a ferroelectric crystal, the spontaneous polarization disappears above a thermodynamic phase transition temperature known as the Curie temperature, T_c.

Similar to their magnetic counterparts, ferroelectrics show hysteretic behavior when polarization is measured as the function of external electric field. With the increase of the electric field, the polarization reaches its saturation, P_s. With the decrease of the electric field, the curve does not follow the initial polarization curve, and at $E = 0$, there is an offset from the origin called the remanence polarization, P_r. The polarization in these kinds of materials usually goes to zero at electric field values $\pm E_c$ called coercive field.

For most of the ferroelectric crystals, the highest symmetry phase, which nor-

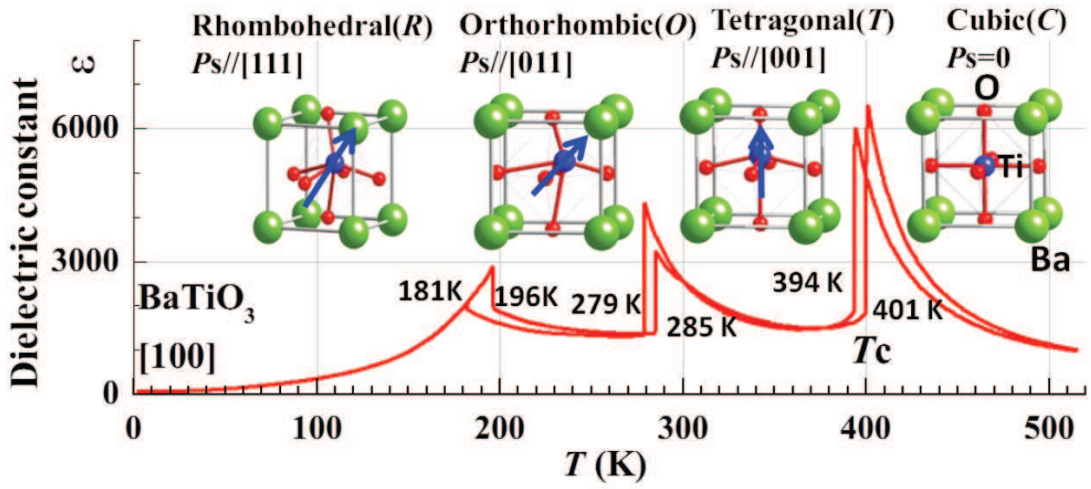

Figure 2.8: Dielectric permittivity vs temperature of the $BaTiO_3$ single crystal [41]. There are changes in spacial symmetry due to Ti displacement which is shown in the schematics.

mally exists at the highest temperature, is non-polar although the structure might melt before reaching it. A typical ferroelectric material possesses spontaneous polarization P^s due to structural distortion that decreases with increasing temperature T. For example, figure 2.8 shows dielectric permittivity as a function of temperature for $BaTiO_3$. As shown in the diagram (figure 2.8 top portion), the high temperature phase is a symmetric cubic phase, and as the temperature is decreased, it goes through a series of structural distortions with lower symmetry phases giving rise to polarization. The polarization often disappears discontinuously (like $BaTiO_3$) and sometimes continuously at Curie point T_c. However, not all polar crystal classes belong to the lower crystal symmetry than non-polar classes, hence transition from non-polar to polar phases as a function of increasing temperature, though rare, do occur. Most ferroelectrics show spontaneous polarization with decreasing temperature, $\mathrm{d}P^s/\mathrm{d}T$

> 0.

Soft Mode

Ferroelectric materials are mainly categorized into two classes- displacive and order-disorder. The distinction is made from the crystal's paraelectric phase. If the paraelectric phase is microscopically non-polar (atomic displacement around the non-polar site), then the transition is displacive, but if it is non-polar only after averaging (atomic displacement around some double or multi-well sites), then the transition is of the order-disorder type. Both transitions are usually associated with the condensation of soft (low frequency) optical phonon modes. In case of the displacive transition, the soft mode shows propagating dynamics in the crystal whereas in the case of order-disorder it has a diffusive nature. The displacive soft mode is a damped optical phonon with small quasi-harmonic motion about their mean-free path. The diffusive soft mode is not really a phonon but a large amplitude thermal hopping motion between the wells [17, 40].

2.3.2 Magnetoelectric

Though rare in nature, some materils show coupling between their electric and magnetic order parameter. Such a phenomenon is known as the magnetoelectric effect. The magnetoelectric effect can be formulated from the free energy (F) [1]

$$F(\mathbf{E},\mathbf{H}) = F_0 - P_i^s E_i - M_i^s H_i - \frac{1}{2}\epsilon_0\epsilon_{ij}E_iE_j - \frac{1}{2}\mu_0\mu_{ij}H_iH_j - \alpha_{ij}E_iH_j - \frac{1}{2}\beta_{ijk}E_iH_jH_k - \frac{1}{2}\gamma_{ijk}H_iE_jE_k - ... \quad (2.24)$$

Here **E** and **H** are the electric and magnetic fields. Similarly, P^s and M^s are spontaneous polarization and magnetization, while ϵ_0 is permittivity of the free space and ϵ_{ij} is relative permittivity second rank tensor. The magnetic counterpart μ_0 is the permeability of free space and μ_{ij} is the relative permeability second rank tensor. The sixth term describes the linear magnetoelectric coupling *via* the second rank tensor, α_{ij}. Higher order magnetoelectric effects are represented by β and γ. Using the above expression 2.24, polarization and magnetization are obtained by differentiating F with respect to **E** and **H** respectively [1],

$$P_i(\mathbf{E}, \mathbf{H}) = P_i^s + \epsilon_0 \epsilon_{ij} E_j + \alpha_{ij} H_j + ... \tag{2.25}$$

$$M_i(\mathbf{E}, \mathbf{H}) = M_i^s + \mu_0 \mu_{ij} H_j + \alpha_{ij} E_i + ... \tag{2.26}$$

Multiferroics have gained much attention in the last two decades because of their potential technological applications [1,2]. Though ferromagnetism and ferroelectricity have independent origins in the material, their co-existence can lead to other novel properties that are not present in either state. Moreover, the coupling between the electric and magnetic order parameters allows manipulation of the polarization with a magnetic field and the modification of the magnetization with an electric field.

2.4 Dielectric relaxation

When a dielectric material is placed in an external electric field **E**, a non-zero polarization **P** is induced because of the formation of a macroscopic dipole moment. The relation between the applied external **E** and **P** can be expressed by

$$P_i = \varepsilon_0 \chi_{ij} E_j, \tag{2.27}$$

where $\varepsilon_0 = 8.854 \times 10^{-12}$ F·m^{-1} is the dielectric permittivity of the vacuum and the proportionality constant χ_{ij} is the dielectric susceptibility tensor. For the case of uniform and isotropic media, the expression in 2.27 takes the simpler form

$$P = \varepsilon_0 \chi E. \tag{2.28}$$

Dielectric relaxation refers to the lag with which the electrical polarization **P** of the material response to the applied external electric field as the electric dipoles slowly reorient in response to the field and the polarization reaches equilibrium. This can be expressed in terms of relaxation function, $\Phi(t)$:

$$P(t) = P_s[1 - \Phi(t)]. \tag{2.29}$$

The relaxation function obeys a simple exponential law i.e. $\Phi = \exp(-t/\tau)$ [42]. Here P_s is the final static value of the polarization which is obtained after turning on the external electric field **E** for a long time, t $\rightarrow \infty$. However, due to thermal motion, when the external field is removed, the polarization is expected to decays as shown in figure 2.9 and the expression 2.30.

$$P(t) = P_s\Phi(t) = P_s \cdot \exp(\frac{-t}{\tau}). \tag{2.30}$$

By differentiating equation 2.29, the rate of change of field-induced polarization can be expressed as

$$\frac{dP(t)}{dt} = P_s\frac{e^{-t/\tau}}{\tau}. \tag{2.31}$$

Both time- or frequency- domain measurements of the dielectric response are possible though frequency-domain measurements are preferred for many applications. Equation 2.31 is used for time domain experiments of the dielectric relaxation by

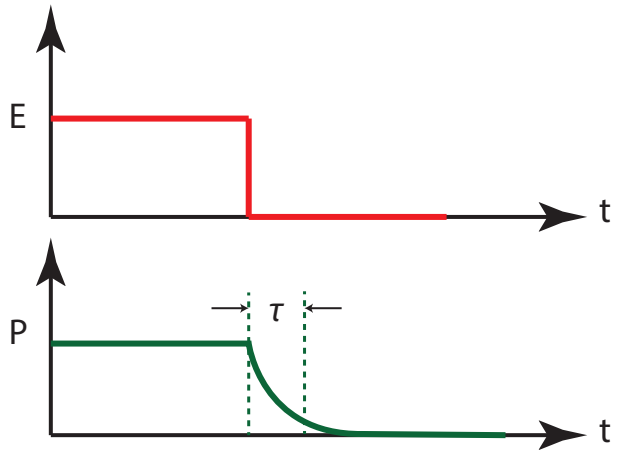

Figure 2.9: Dielectric relaxation after the removal of the external electric field.

step-function or pulsed electric fields. Due to the characteristic relaxation time of the material, when a periodic harmonic (sinusoidal) electric field $\mathbf{E}$(t) ($E_s \cdot \sin\omega t$) with angular frequency $\omega = 2\pi f$ is applied, the output polarization does not respond instantaneously but appears to be shifted by some angle represented as a phase difference. Therefore, in the frequency-domain complex quantities like the susceptibility,

$$\chi^*(\omega) = \chi'(\omega) - i\chi''(\omega) \tag{2.32}$$

and relative dielectric permittivity,

$$\varepsilon^*(\omega) = \varepsilon'(\omega) - i\varepsilon''(\omega) = 1 + \chi^*(\omega) \tag{2.33}$$

can be used to conveniently describe dielectric relaxation. [Note: $\varepsilon_0\varepsilon^*(\omega)$ is called permittivity usually denoted by just ε, and ε_r is used in some literature to denote complex relative permittivity].

The polarization in the time-domain $P(t)$ or frequency-domain $P(\omega)$ can be switched

back and forth using a Fourier transformation so that

$$P(\omega) = \int_0^\infty P(t) \cdot \exp(-iwt) \cdot dt = P_s \int_0^\infty \exp(\frac{-t}{\tau}) \cdot \exp(-iwt) \cdot dt \tag{2.34}$$

From the equation 2.34, it follows that at a very low frequencies ($\omega \to 0$), the total polarization arises primarily from the static polarization. The solution for the above integral is

$$P(\omega) = \frac{P_s \cdot \tau}{1 + i\omega\tau} \tag{2.35}$$

Similarly, in frequency-domain, equation 2.28 becomes:

$$\mathbf{P}(\omega) = \varepsilon_0 \chi(\omega) \mathbf{E}, \tag{2.36}$$

The susceptibility becomes static susceptibility at zero frequency i.e. $\chi_s = P_s/(\varepsilon_0 E_s)$ for $\omega \to 0$. Using a complex conjugate, $1 - i\omega\tau$, in equation 2.35 and combining the result with equations 2.32 and 2.36, the real and imaginary parts of χ can be written as

$$\chi'(\omega) = \frac{1}{\varepsilon_0} \cdot \frac{\chi_s}{1 + \omega^2\tau^2}, \tag{2.37}$$

$$\chi''(\omega) = -\frac{1}{\varepsilon_0} \cdot \frac{\chi_s \cdot \omega\tau}{1 + \omega^2\tau^2}, \tag{2.38}$$

For the first order system, the dielectric response in the frequency domain is obtained by a Laplace transform [43]

$$\varepsilon^*(\omega) = \varepsilon_\infty + \frac{\varepsilon_s - \varepsilon_\infty}{1 + i\omega\tau}, \tag{2.39}$$

where ε_∞ = dielectric constant at high frequency and

ε'_s = limiting low-frequency dielectric constant.

As such, the real part of the dielectric constant is given by

$$\varepsilon'(\omega) = \varepsilon_\infty + \frac{\varepsilon_s - \varepsilon_\infty}{1 + \omega^2\tau^2}, \tag{2.40}$$

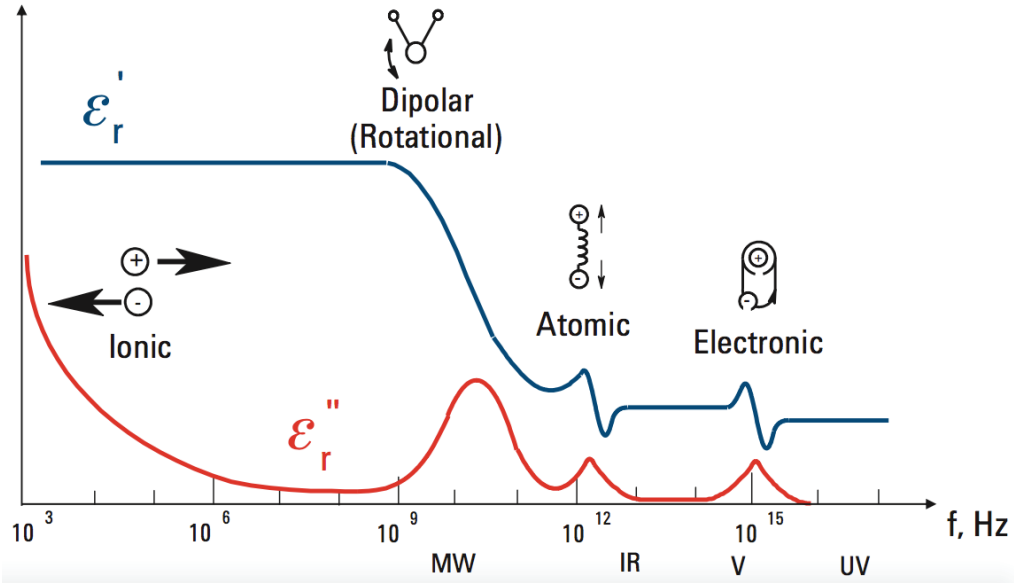

Figure 2.10: Frequency response of dielectric mechanisms. Reproduced from reference [44].

and the imaginary part of the dielectric constant is given by

$$\varepsilon''(\omega) = (\varepsilon_s - \varepsilon_\infty)\frac{\omega\tau}{1+\omega^2\tau^2}. \tag{2.41}$$

Several mechanisms (such as dipolar, ionic, atomic and electronic) may be responsible for the dielectric behavior (permittivity) at the microscopic or mesoscopic level (figure 2.10). Each of these mechanisms has its characteristic "cutoff" frequency unique to the dielectric material. As the frequency increases, the faster mechanisms contribute to the real part of dielectric while the slower mechanism dies off. At the characteristic "cutoff" frequency, there will be a corresponding peak at the imaginary part of dielectric (loss factor) [44].

2.4.1 Debye relaxation and Cole-Cole plot

The ideal Debye relaxation (Debye 1929) has a single relaxation time that can be obtained by rearranging 2.40 and 2.41 as

$$[\varepsilon' - \frac{\varepsilon_s - \varepsilon_\infty}{2}]^2 + (\varepsilon'')^2 = [\frac{\varepsilon_s - \varepsilon_\infty}{2}]^2 \tag{2.42}$$

Hence a plot of ε' vs. ε'' produces a semi-circle with center $[\frac{\varepsilon_s - \varepsilon_\infty}{2}, 0]$ and radius $\frac{\varepsilon_s - \varepsilon_\infty}{2}$. Such a plot is referred as Cole-Cole plot [45]. In the case of the presence of a distribution of relaxation times the Cole-Cole dispersion law [46] is modified to

$$\varepsilon(f) = \varepsilon_\infty + \frac{\varepsilon_s - \varepsilon_\infty}{1 + (i2\pi f\tau)^\beta}, \tag{2.43}$$

where β $(0 < \beta \leq 1)$ is the width of relaxation time distribution. For a single relaxation time $\beta = 1$.

Chapter 3

Experimental Procedures

3.1 Thin film growth

3.1.1 Molecular Beam Epitaxy

Molecular Beam Epitaxy (MBE) is a growth technique that uses localized beams of atoms or molecules as a source of constituents to be deposited on the surface of single crystal substrate under ultra-high vacuum (UHV). Usually the substrate is kept at an elevated temperature that provides enough thermal energy to the arriving constituents so that they can migrate or order themselves according to the crystal structure of the substrate. This is called epitaxial growth. The UHV environment provides a contaminant- and collision-free path for the beam of constituents to the surface of the substrate. In a UHV environment, the velocities of residual gases (v_g) are much smaller than the velocity of beam constituents (v_b), and the mean free path

is given by

$$L_b^{-1} = \pi n_g d_{bg}^2 + \sqrt{2}\pi n_b d_b^2, \tag{3.1}$$

with $d_{bg} = (d_g + d_g)/2$, where n_b and d_b are the concentration and diameter of the molecules in the constituent beam, and n_g and d_g are the concentration and diameter of the residual gas in the chamber, respectively [47]. If typical experimental numbers for expression 3.1 are plugged-in then the mean free path of the beam L_b is several times or even an order of magnitude larger than the distance between the deposition surface and the source of the beam. The chilled walls or cryo-panels usually filled with liquid nitrogen act as an absorbent to remove digressing contaminants from the system.

A MBE growth chamber typical consists of many components for the growth of materials and for *in-situ* characterization. Some of these components include:

1. Effusion cell and electron-beam with source materials
2. Shutters for the sources and substrates
3. Actuation mechanism for the substrate/sample
4. Substrate/sample heater
5. Appropriate vacuum pumps such as ionpump and cryopump
6. Beam flux monitor (quartz crystal monitor)
7. Mass spectrometer or residual gas analyzer (RGA)

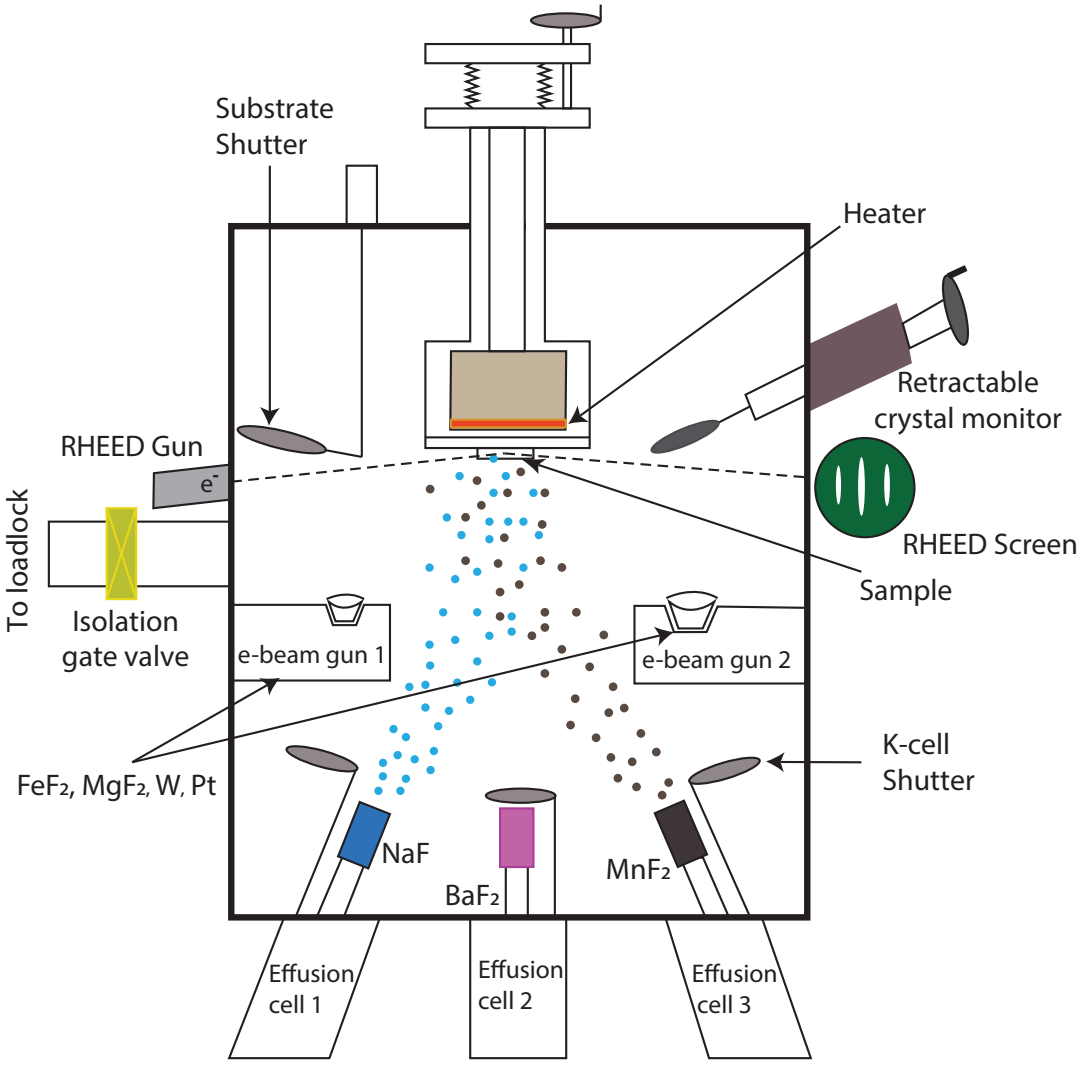

Figure 3.1: The schematics of MBE used for the growth of $NaMnF_3$ thin film at UCSC.

8. Characterization tools such as reflection high energy diffraction (RHEED), low-energy electron diffraction (LEED), auger electron spectroscopy (AES) and others.

A schematic of MBE chamber used for the growth of $NaMnF_3$ at UCSC is shown in figure 3.1.

For a typical growth, a source material kept inside a high-grade non-reactive crucible (such as pyrolytic boron nitride, alumina, or graphite) is radiatively heated by a resistive heating filament until it sublimates. Several layers of Ta foil surround the crucible for radiative shielding and efficient heating. Meanwhile, the temperature measured by a thermocouple, which is in direct contact with the crucible, is used as feedback for proportional-integral-derivative (PID) controller to efficiently control the temperature of the materials inside the crucible. Such PID control allows precise control of the intensity of the flux which is essential for co-deposition of materials. It is also essential to have shutters for sources and substrate which are engaged whenever particular beam flux is unwanted.

NaF and MnF_2 Rates

The incoming beam flux from the source is measured using a quartz crystal microbalance (QCM) at the sample growth position. QCM works using the principle that the amount of mass added to a quartz crystal electrode is proportional to the resulting shift in resonant frequency of the oscillator [48]. For the stoichiometric growth of $NaMnF_3$, 1 mole of NaF has to react with 1 mole of MnF_2 according to the following chemical equation:

$$\mathrm{NaF} + \mathrm{MnF_2} \rightarrow \mathrm{NaMnF_3}, \tag{3.2}$$

which also means flux (ϕ) of NaF should be equal to flux of MnF_2 i.e.

$$\phi_{NaF} = \phi_{MnF_2}. \tag{3.3}$$

The flux of atoms or molecules can be written as:

$$\phi[\text{molecules}/\text{Å}^2 \cdot \text{s}] = Rate[\text{Å}/\text{s}] \times n[\text{molecules}/\text{Å}^3] \tag{3.4}$$

with

$$\text{n} = N_A \times \rho/M, \tag{3.5}$$

where N_A is Avogadro's number (=6.022×10^{23} mol^{-1}), and ρ and M are the density and molecular weight of the materials respectively. It is more precise and practical to directly measure the thickness of material deposited on microbalance over time, i.e., the rate of arrival of molecules per second than beam flux using a QCM. To calculate the correct deposition rates for NaF and MnF_2 to get stoichiometric $NaMnF_3$, equation 3.4 can be rewritten in terms of the NaF (R_{NaF}) and MnF_2 (R_{MnF_2}) rates as

$$R_{NaF} = \frac{\phi_{NaF}}{n_{NaF}} \tag{3.6}$$

and

$$R_{MnF_2} = \frac{\phi_{MnF_2}}{n_{MnF_2}}. \tag{3.7}$$

Now dividing equation 3.6 by equation 3.7 and using equation 3.3 and 3.5, the relative rates can be expressed as

$$\frac{R_{NaF}}{R_{MnF_2}} = \frac{n_{MnF_2}}{n_{NaF}} = \frac{\rho_{MnF_2}}{\rho_{NaF}} \times \frac{M_{NaF}}{M_{MnF_2}} \tag{3.8}$$

After plugging in the densities and molar mass of the respective materials in equation 3.8, the numerical result is

$$\frac{R_{NaF}}{R_{MnF_2}} = \frac{3.980 gm/cm^3}{2.556 gm/cm^3} \times \frac{41.987 gm/mol}{92.934 gm/mol} = 0.703 \tag{3.9}$$

Therefore, the rate of NaF has to be 70.3% of that of MnF_2 for stoichiometic growth of $NaMnF_3$ films.

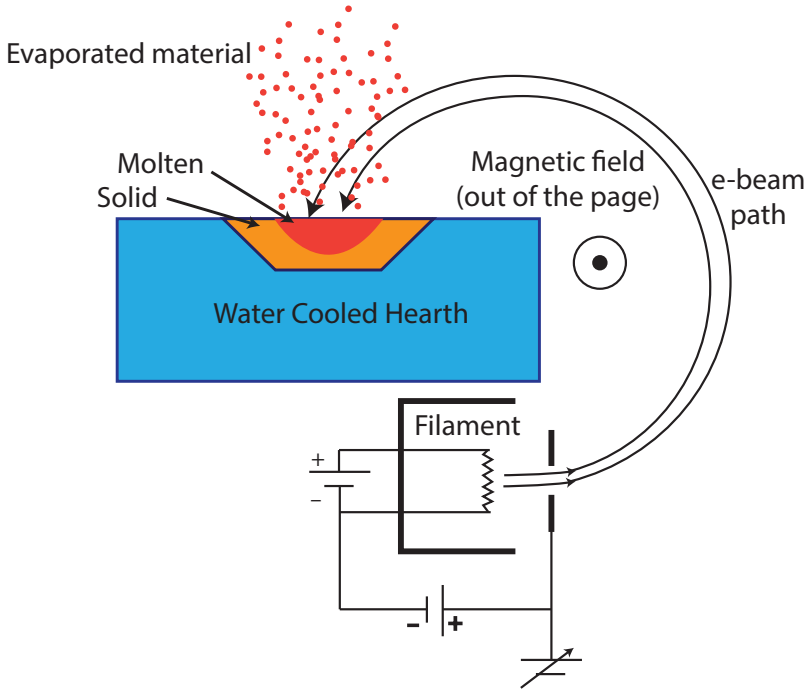

Figure 3.2: Schematic representation of e-beam evaporator.

Electron-Beam Evaporation

Another thin film growth mechanism which is used in this thesis is electron-beam (e-beam) evaporation. MBE chamber used for the growth of $NaMnF_3$ in UC Santa Cruz is equipped with two such e-beam guns manufactured by MDC vacuum products LLC (see figure 3.1).

E-beam evaporation can be used to evaporate a source material with a high melting point where k-cells usages are less feasible. An electron beam emitted by a filament at high voltage (5 keV) is bent into an arc using permanent magnets onto a crucible with the source material. The kinetic energy is transferred from the e-beam to the source material, heating the material until it melts or sublimates and evaporates

towards the substrate.

3.1.2 Pulse Laser Deposition

Since the late 1980s, pulse laser deposition (PLD) has been widely used as a powerful synthesis technique due to its success in fast and reproducible oxide film growth [49]. There has been a significant development in the technique since the 80s, and it has found a place in a wide variety of material growth (such as semiconductors, insulators, metals, and polymers) not just oxides. An advantage of PLD over other techniques is that if a multielement target is used, the resulting thin film will have the same stoichiometry.

PLD is based on physical vapor deposition (PVD) with some similarities to both molecular beam epitaxy and sputtering [49]. A focused laser pulse with sufficiently high energy density is used to ablate or vaporize a small amount of the target material into a plasma plume as shown in the figure 3.3. The directional plume acts as a material flux for the thin film growth. Using a laser with ultra-violet (UV) wavelength and nanosecond pulses, it is possible to eject small volume while other nearby areas are still intact in the target. The heat affected zone is determined by the thermal diffusion length l_{th} as

$$l_{th} = 2\sqrt{\alpha \tau_p} \tag{3.10}$$

where τ_p is the period of the pulse and α is the thermal diffusivity given by $\alpha = \frac{\kappa}{\rho c_p}$ where κ is the thermal conductivity, ρ is the mass density and c_p is the specific heat capacity [50, 51].

For this research, $SrRuO_3$ was grown on top of $SrTiO_3$ *via* PLD. $SrRuO_3$ is a con-

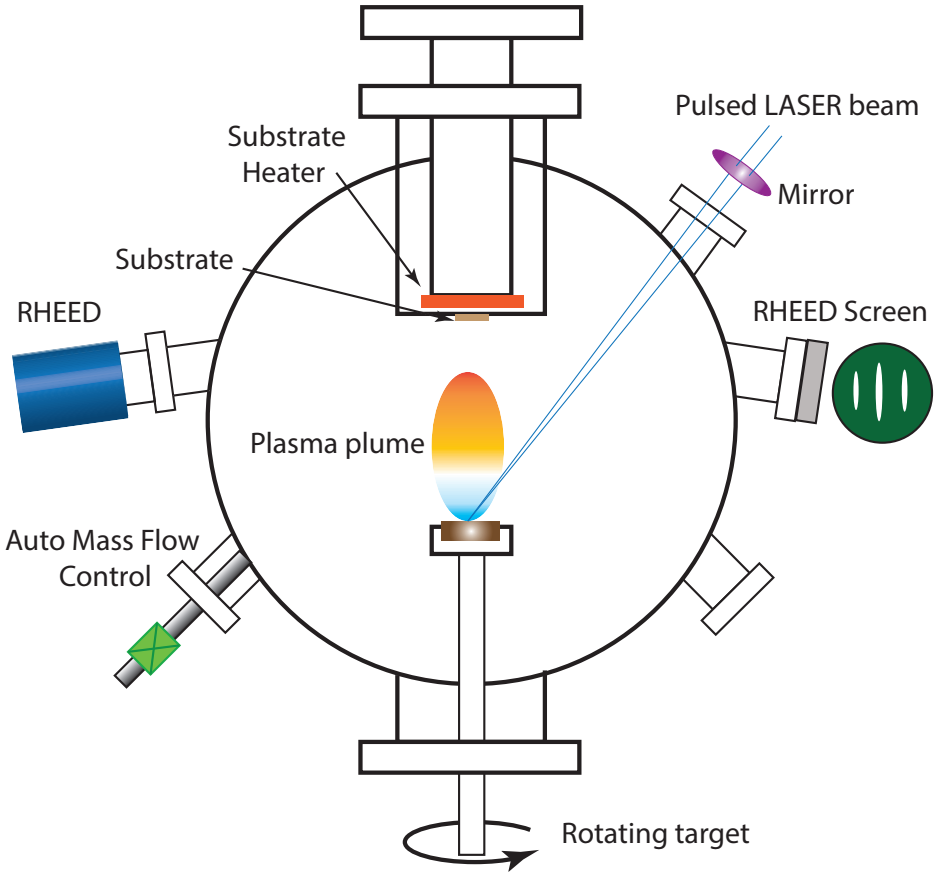

Figure 3.3: Schematic of PLD. Various components have been labeled.

ducting perovskite oxide material which is ferromagnetic below 160 K [52]. $SrRuO_3$ grows epitaxially on $SrTiO_3$ [52,53] and in this project was used as a bottom electrical contact for perpendicular electrical measurements. Its magnetic properties were also measured to determine exchange bias, as discussed in chapter 5. The PLD system manufactured by Neocera was equipped with a KrF excimer laser ($\lambda = 248$ nm) from Coherent Inc. The PLD chamber was also equipped with automatic gas mass flow controls and automatic turbo pump which allows for the precise control of the background pressure. An *in-situ* RHEED system manufactured by STAIB Instruments

was used to monitor film growth.

3.2 Patterning: Photolithography

Photolithography is a process of transferring patterns from a mask to the sample by exposing a light-sensitive polymer (photoresist) to ultraviolet (UV) light. The photoresist can be classified as positive or negative, depending on how it reacts with UV light. Positive resists when exposed to the UV light become weakened and can be easily removed during the development process. However, negative resists when exposed to the UV light become rigid and less soluble; therefore, it forms the reverse of the mask patterns on the sample [54]. Patterning sample or wafer using photolithography normally involves four steps: 1) spinning the sample with photoresist to form a uniform top layer, 2) Soft-baking to remove solvent from the photoresist and to increase resist adhesion to the sample, 3) aligning sample to the mask and exposing resist to the UV light, 4) developing the pattern by flooding the sample with a developer solution [54].

For the patterning of our samples, AZ 5214 E photoresist was used as a positive process. The photoresist was spun on the samples at 4000 rpm for 60 s to attain a uniform thickness of about 1 μm. The samples were then immediately "soft-baked" at 95 °C on a hot plate for 45 s. For the UV light exposure, Karl Suss MA6 mask aligner with a wavelength of 320 nm was used. The photo-mask was kept in direct contact with the samples after the alignment. The samples were exposed to a dosage of 100 mJ/cm^2 before developing them in a bath of AZ 300 MIF developer solution for about 15-30 s.

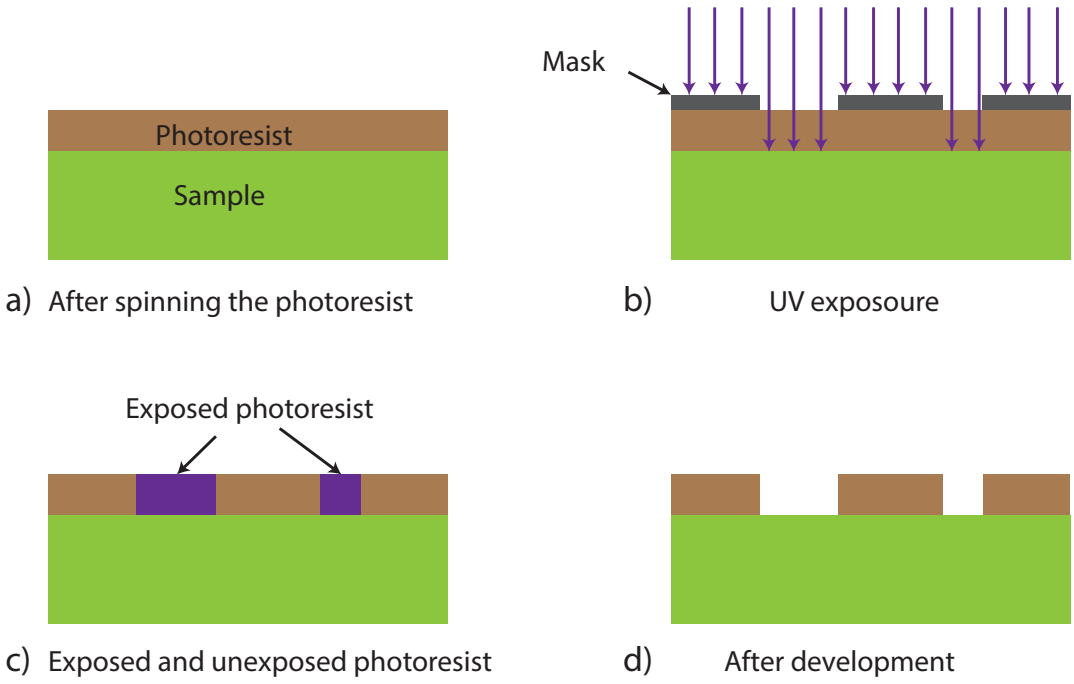

Figure 3.4: Schematic representation of the photolithography steps: a) Photoresist is spun to create a uniform layer. b) Photo-mask is kept in direct contact with the resist during the UV exposure. c) The exposed region becomes easily soluble due to chemical weakening (positive process). d) Developer solution removes the exposed resist.

3.3 Characterization

3.3.1 Reflection High Energy Electron Diffraction

Reflection high energy electron diffraction (RHEED) is a powerful surface analysis technique used to monitor the surface structure and the quality of thin film *in-situ* in a vacuum growth chamber. In a typical RHEED, an electron beam with high energy typically between 10-50 keV is incident at a grazing angle (< 3 deg.) on the sample surface. The beam is then diffracted by the first few planes of the crystal lattice due to its small penetration depth. A schematic image of RHEED geometry is shown in

figure 3.5. Due to the RHEED sensitivity limited to the few layers below the surface, the sampling volume is approximately a two-dimensional area which degenerates to one-dimensional rods pointing normal to the sample surface in reciprocal space [55]. When these continuous rods cross the surface of the Ewald sphere, a specular spot is created as shown in the schematic 3.5. The RHEED analysis on NMF was carried *in-situ* by RH 15 RHEED system manufactured by STAIB Instrument, Inc with operating voltage of 15 keV corresponding to $\sim$ 0.1 Å de Broglie wavelength and current of 1.5 A.

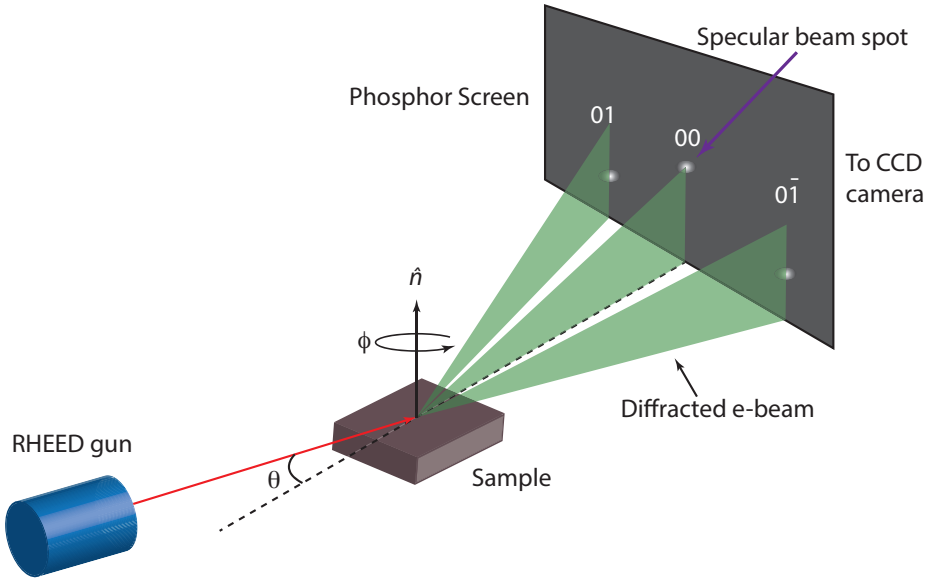

Figure 3.5: Schematic image of RHEED geometry used in the MBE and PLD systems.

3.3.2 Atomic Force Microscopy

Atomic force microscopy (AFM) is a technique that maps surface topography of a sample with very high resolution and accuracy. AFM is quite unique with respect to other microscopy as it does not use light or an electron beam to create the images.

It uses a probe with a sharp tip that physically "feels" sample surface to map out the height.

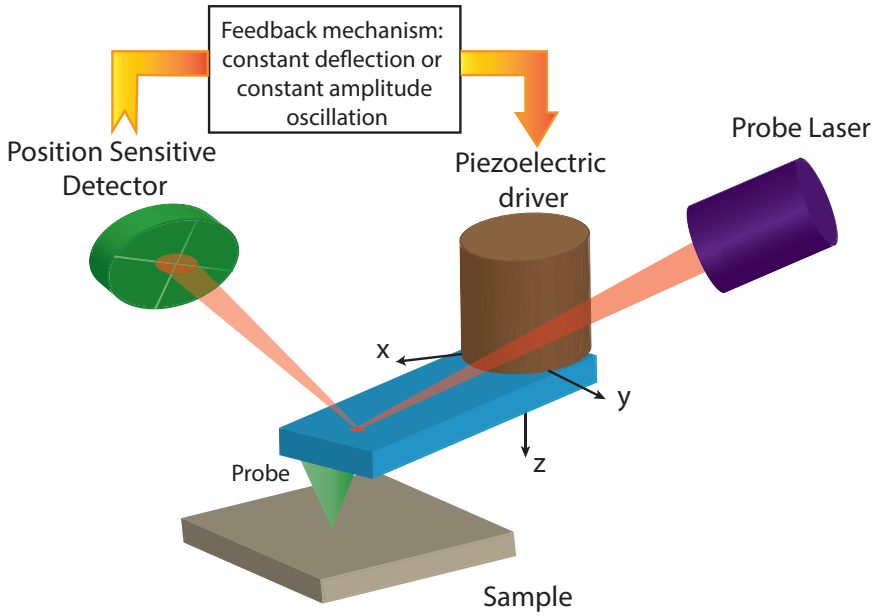

Figure 3.6: Schemtaic of AFM operation.

The basic AFM setup consists of a probe with sharp tip, high precision piezoelectric driver, a laser, photodiode, and position sensitive detector (PSD) (see AFM schematic figure 3.6). As sharp cantilever tip is brought in proximity to the sample surface, an electrostatic force between the sample surface and tip causes the cantilever to bend [56]. The amount of bending in the cantilever is usually measured by the shift in the reflected laser spot from the top of cantilever onto the PSD. There are two modes of imaging that are commonly used to obtain the topography of the sample: tapping and contact mode. In contact mode, the vertical deflection between the tip and the sample surface is kept constant by a feedback mechanism. In the case of tapping mode, a piezoelectric drives the cantilever in an oscillatory motion and the

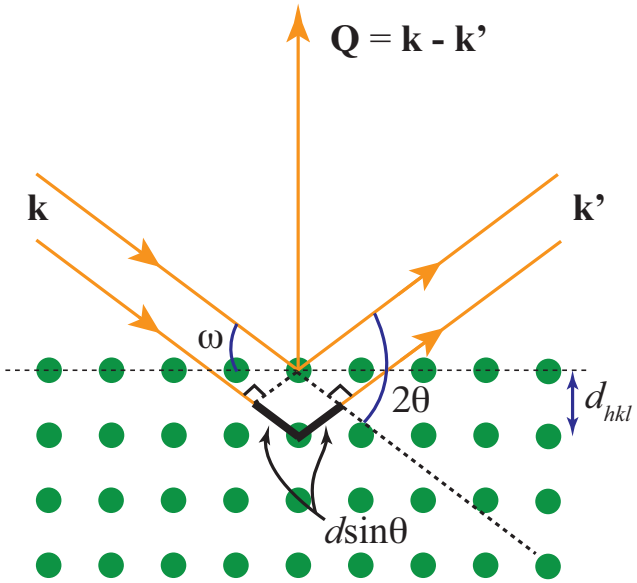

Figure 3.7: Schematic of X-ray diffraction by parallel lattice planes separated by d in a crystal. ω and 2θ are the position of the X-ray source and the detector respectively. $\boldsymbol{k}$ and $\boldsymbol{k'}$ are the incident and diffracted wave vectors respectively.

output signal from the photodetector is converted into the amplitude and phase of the cantilever oscillation. As such, the feedback mechanism keeps the force constant in the contact mode and the oscillation amplitude constant in the tapping mode.

3.3.3 X-ray Diffraction

A non-destructive technique that is widely used to characterize powder or crystalline samples is X-ray diffraction (XRD). It is used to determine various structural information such as composition, epitaxy, thickness, strain, mosaic spread, and preferred orientation.

Modern crystallography uses X-ray tubes to generate X-rays. The tube is surrounded by insulating glass and is composed of a metallic target (usually heavy metal

like copper or tungsten) and a tungsten filament which are separated by about a centimeter. A fairly large potential difference on the order 50 kV is applied between the filament and target. The high energy electrons emitted by the filament (cathode) are accelerated towards the target (anode). The impinging electrons produce X-rays directly due to sudden deceleration (*Brehmsstrahlung*) or indirectly by knocking out inner shell electrons of the target which fall back into a vacant shell emitting X-rays determined by the electron energy level (characteristic radiation).

The X-rays used for crystallography have a characteristic wavelength comparable to the atomic distance within crystalline solids. This allows diffraction of monochromatic X-rays beams. Moreover, whenever the Bragg condition (expression 3.11) is satisfied, a diffraction peak is observed due to the constructive interference of the beam scattered by the set of lattice planes.

For a parallel lattice plane separated by d_{hkl} (where hkl is Miller indices for the denoting planes), the path difference between the adjacent plane is $2d\sin\theta$ (where θ is the angle of the incident beam with respect to the plane). Constructive interference for the beam occurs when the path difference between the adjacent planes is an integer multiple of the wavelength of the X-rays, λ, as given by Bragg's law

$$n\lambda = 2d_{hkl}\sin\theta \tag{3.11}$$

$NaMnF_3$ thin films for this research were characterized by two different Rigaku X-ray diffraction (XRD) system. The one used in WVU was a rotating anode X-ray generator with a graphite bent crystal monochromator optimized for Cu K_α radiation, while the one used in UCSC (Scott Oliver Lab) was a Rigaku SmartLab system equipped with a Ge(220) two-bounce monochromator incident optics with Cu $K_{\alpha 1}$

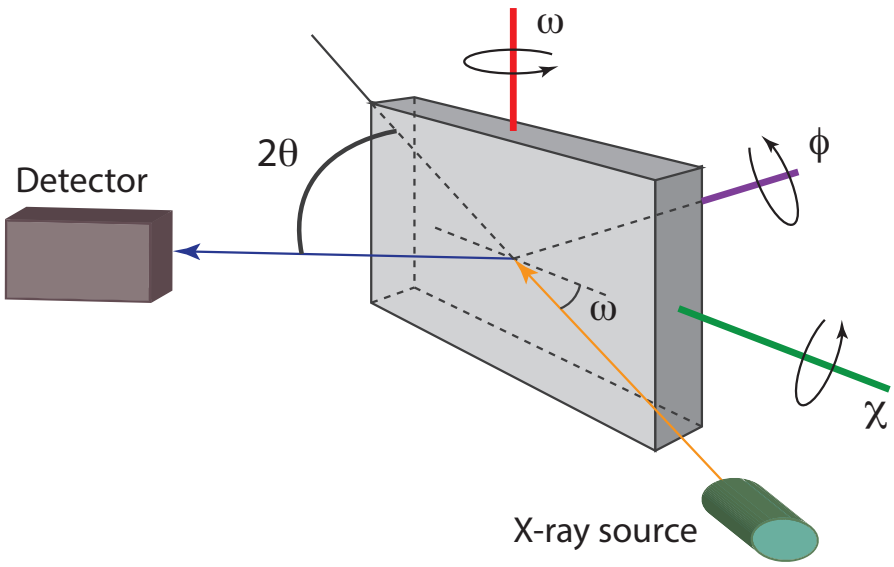

Figure 3.8: Schematic representation of a sample on four circle (2θ, ω, ϕ, and χ) goniometer.

radiation.

An efficient and precise method of performing XRD is a using four circle geometry (2θ, ω, ϕ and χ) as shown in the figure 3.8. Different types of scans employed to probe the structural parameters of the films are listed as follows:

1. Symmetric $\omega - 2\theta$ measurement:

   - Symmetric $\omega - 2\theta$ measurement allows the precise determination of the lattice parameter of the planes that are parallel to the sample surface normal vector and is measured by coupled $\omega - 2\theta$ scan. The diffracted beam intensity is measured by setting ω half of 2θ i.e. $\omega = \theta$. This method is also called out-of-plane XRD as the scan is parallel to the scattering vector shown in figure 3.7.

   - Such a scan provides crucial information about the preferred growth orien-

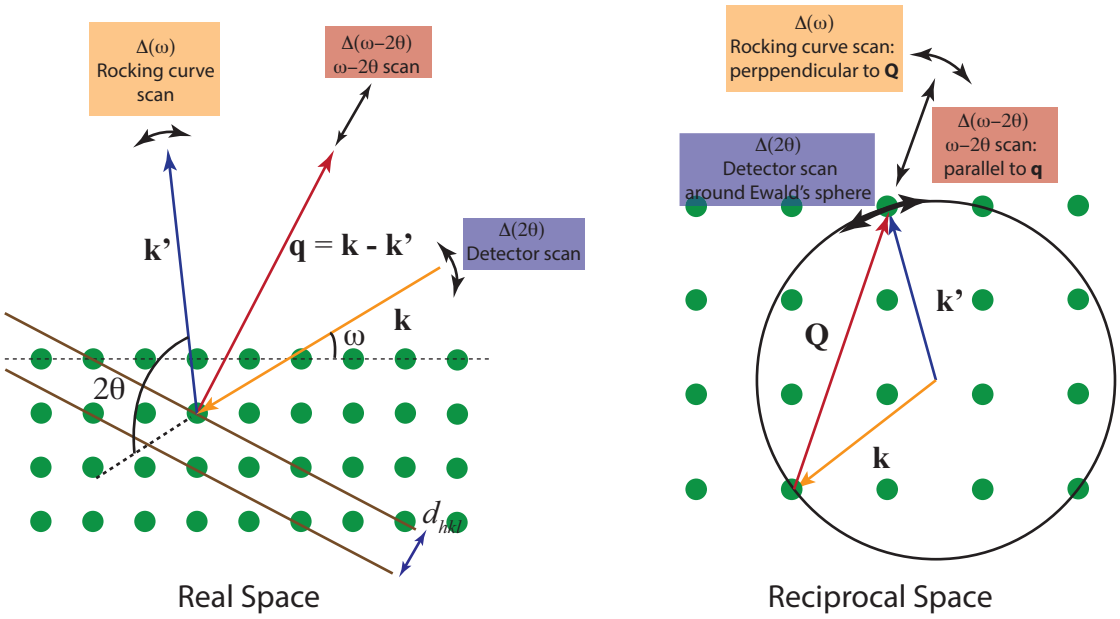

Figure 3.9: An illustration of the type of XRD scans in real and reciprocal space.

tation, phase, impurities, lattice strain, stress and out-of-plane grain size of the film.

2. Rocking curve measurement:

   - The diffracted beam intensity is measured by setting 2θ constant while ω sweeps a segment of the circle perpendicular to the scattering vector as shown in figure 3.9.
   - Such a scan provides crucial information on mosaicity, defects, crystalline quality and texture of the film.

3. In-plane scan:

   - The diffraction from the lattice planes at an angle to the surface of the

sample is probed. The measurements can be performed due to the reflection from the in-plane component of the scattering vector. It involves adjusting the sample to the tilt angle χ and performing the ϕ scan. A modified version of ω - 2θ (also called "asymmetric ω - 2θ" or "off-axis ω - 2θ") can also be performed after optimizing all the angles involved.

- The information from such scan can be used to determine epitaxy, lattice parameters, texture, mosaic spread, and defects.

3.3.4 X-ray Reflectometry

When the angle of incidence of the incoming X-ray beam is small (< 10 degree), the beam cannot penetrate deep into the material but is totally reflected due to the optical scattering from the material. Such specular behavior of the x-ray beam is known as X-ray reflectivity (XRR). The measurement geometry is the same as symmetric ω - 2θ scan as shown in figure 3.7. As solids have a refractive index of slightly smaller than one, the incoming x-ray beam at a small angle goes through total external reflection. Meanwhile, the reflectivity from a thin film leads to X-ray beam intensity oscillations called "Keissig fringes" when intensity is measured as the function of angle. This is due to alternating constructive and destructive interference of the reflected beam [57]. Reflectivity data can be fitted to obtain precise thickness and roughness of the surface as well as the interfacial information about the sample. The open source software such as GenX [58] can be used to fit the data.

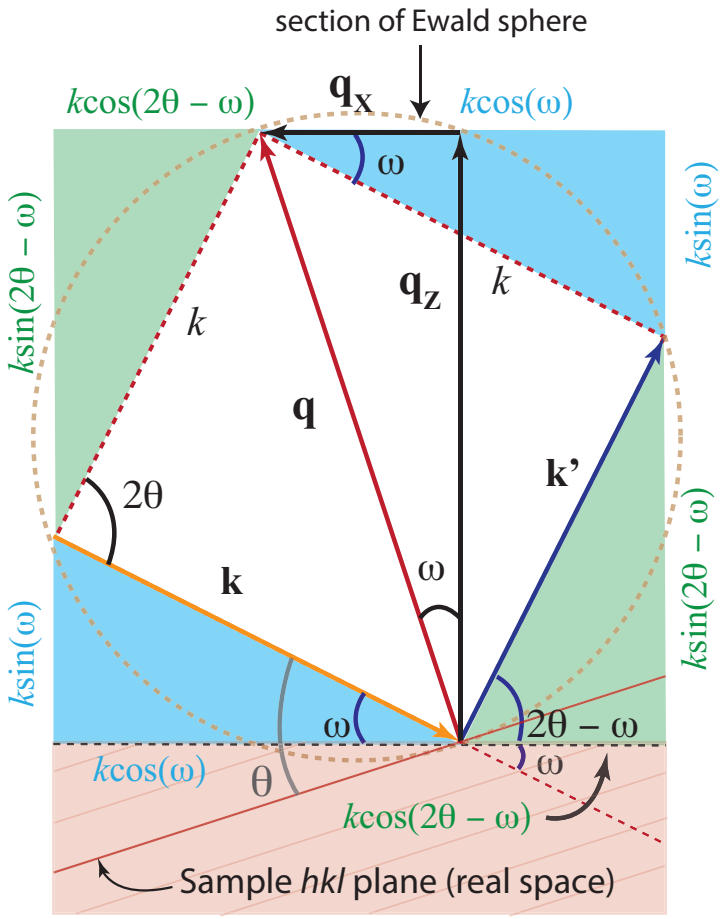

Figure 3.10: Schematic representation of the relationship between the scattering vector and the angles of incidence and detection.

3.3.5 Reciprocal Space Map

Since X-rays non-destructively interact with the atoms, they can be used to determine average atomic positions in the crystal. However, the interpretation of the X-rays diffraction patterns by using the Bragg's law is very tedious. The concept of the reciprocal lattice and Ewald or reflecting sphere are on the other hand quite elegant and easy to use. The convenience of the reciprocal lattice is that the change

in the scattering vector, **k'-k**, must be equal to some reciprocal lattice vector **G**,

$$\Delta \mathbf{k} = \mathbf{G}, \tag{3.12}$$

due to the Bragg scattering from a periodic lattice where **G** and d_{hkl} are related by $d_{hkl} = 2\pi/|\mathbf{G}|$ [17]. A geometrical way of representing the diffraction condition is called Ewald construction. Using the Bragg diffraction condition, a sphere of radius k can be defined as shown in the figure 3.10 [Note: $|\mathbf{k}| = |\mathbf{k'}|$ and $|\mathbf{k}| = \text{const.}$]. Such a sphere is called Ewald sphere.

As mentioned above, the condition for the diffraction peak to occur is intuitive and simple to visualize in **q** space. It is, therefore, more convenient to use the in-plane component q_x and out-of-plane q_z of the scattering vector then the relation between the instrumental coordinates ω and 2θ. From the figure 3.10, components of the scattering vectors have the following relation with instrumental coordinates:

$$\begin{aligned} q_x &= k[\cos(\omega) - \cos(2\theta - \omega)], \\ q_z &= k[\sin(\omega) + \sin(2\theta - \omega)]. \end{aligned} \tag{3.13}$$

where $k = 2\pi/\lambda$ is the magnitude of the scattering vector. Reciprocal space mapping is performed in such a way that the intensity map of the q space is obtained around the Bragg reflection. There are two different ways of recording a reciprocal space map: (1) keeping $\omega/2\theta$ constant and subsequent rocking curve measurements or by (2) keeping ω constant and subsequent $\theta/2\theta$ measurements; the latter method was used for recording the reciprocal space map of $NaMnF_3$.

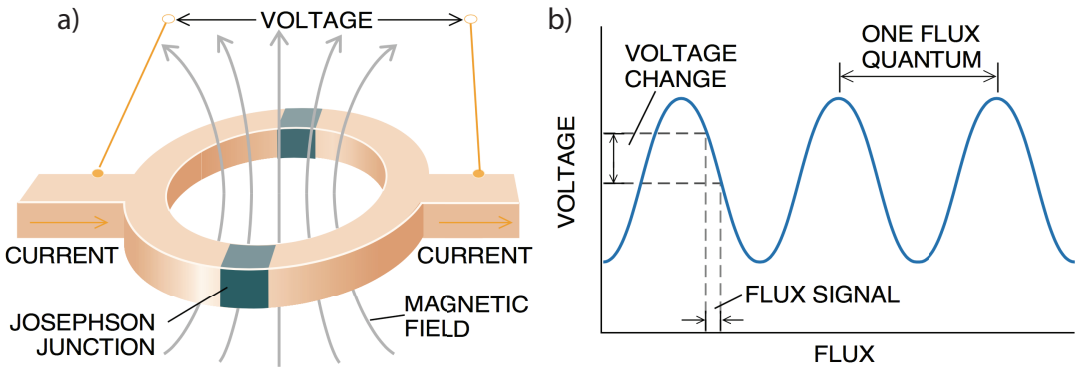

Figure 3.11: DC SQUID illustration and principle: (a) Shows two Josephson junctions which form DC SQUID. (b) Shows the output voltage as a function of applied field. It is possible to measure the change in voltage due to corresponding (tiny) change in the flux. Reproduced from reference [60].

3.3.6 Magnetometry

All the magnetization measurements were carried out using MPMS SQUID (Magnetic Property Measurement System using a Superconducting Quantum Interference Device) manufactured by Quantum Design, Inc. It is the most sensitive method of magnetization measurement. SQUIDs are made out of two weakly coupled superconductors separated by a thin insulation barrier. The junction between the superconductors is known as Josephson junction [59]. There are SQUIDs with one and two Josephson junctions also known as RF- and DC-SQUIDs respectively. A DC-SQUID was used to measure NMF samples so only it will be described in detail. Figure 3.11 (a) shows the schematic representation of the DC-SQUID. A change in magnetic flux through the ring causes the critical current to increase and decrease successively since the current adds to the measuring current in one junction and subtracts in the other [60, 61]. The difference in measuring current results in a voltage difference between the junctions. One oscillation period is an individual flux quanta [flux quanta

$(\phi_0) = \frac{h}{2e} = 2.07^{-15}$ Tm^2] shown in figure 3.11 (b).

In practical magnetometry, the SQUID is coupled via a superconducting circuit consisting of two oppositely wound coils (also called a gradiometer) in series. One coil is magnetically coupled to the SQUID whereas the other one (also called pick-up coil) is used to sense the flux. The oppositely wound coils cancel out stray fields and are sensitive to the gradient of the magnetic field, not the field itself [60]. The system used in this thesis makes use of a second-derivative gradiometer that reduces background drift caused by the relaxation in the magnetic field of SQUID magnet. The gradiometer with the superconducting magnet is housed in the sample chamber which can be cooled down to liquid He temperature.

3.3.7 Ferroelectric Tester

Polarization vs. electric field ($P-E$) measurements are routinely used to characterized ferroelectric materials. A $P-E$ loop of a sample is a plot of induced charge or polarization versus the applied external field at a particular frequency. Ferroelectric materials show a "memory effect" similar to ferromagnets. Therefore, the applied field has a non-linear effect on the polarization giving rise to hysteretic behavior in the sample. Such hysteretic $P-E$ loop can further be used to study saturation polarization (P_s), remanent polarization (P_r) and coercive field (E_c) of the ferroelectric material.

One of the earliest methods of measuring $P-E$ loops was devised by Sawyer and Tower in 1930 [64]. A schematic of a Sawyer-Tower circuit is shown in the figure 3.12 (a). In this method, the sample is connected in series with a large reference

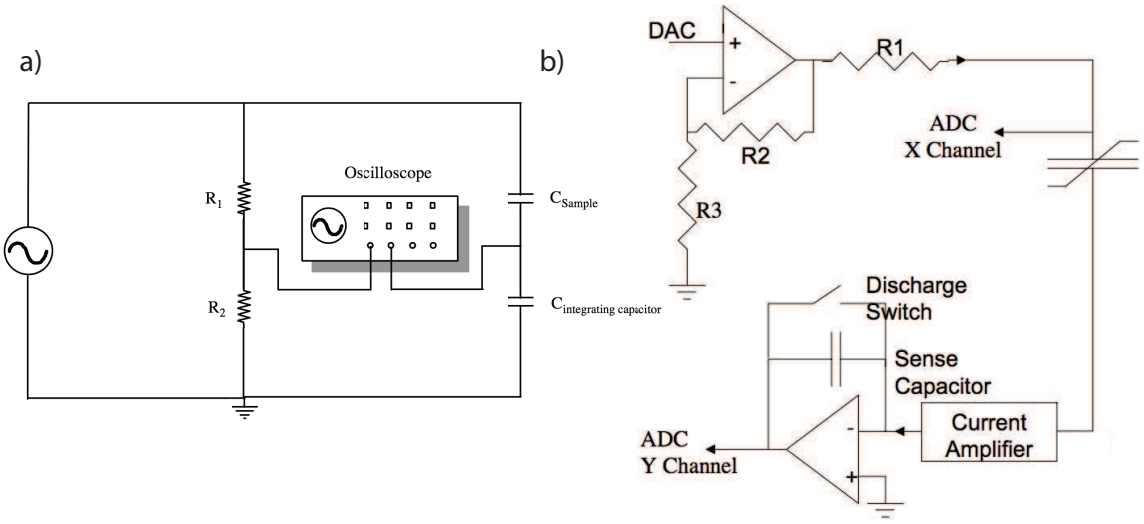

Figure 3.12: (a) Schematic of a Sawyer Tower circuit for P-E loop measurements. Reproduced from reference [62]. (b) Schematic of test path used in ferroelectric tester [63].

capacitor, and the field is controlled by a resistive divider. The large capacitor is used to integrate current into charge. By measuring the voltage drop across the reference capacitor, it is possible to determine the charge/polarization (as $Q = CV$) on the sample. However, this method does not take into account the conductivity of the capacitor, so it is mostly ideal for low loss capacitor. Another method is to use operational amplifiers as a current to voltage converter with a capacitor in the feedback loop [62]. The charge is computed by careful integration of the current with respect to time. However, the smaller current requires the use of current amplification. This technique is widely used in commercially available ferroelectric testers. Figure 3.12 (b) shows one example of a test path for ferroelectric tester used for this research. The ferroelectric properties were tested by Precision LC100 Ferroelectric Tester manufactured by Radiant Technology.

3.3.8 Piezoresponse Force Microscopy

All ferroelectric materials are also piezoelectrics. They exhibit deformation (elongation, contraction or shear) under an external electrical field. Therefore, it is possible to locally switch the polarization with Piezoresponse Force Microscopy (PFM). PFM measures the surface displacements due to piezoelectric effects induced by an applied electric voltage using a conductive tip. The piezoelectric coefficient of the ferroelectric domain relates to the spontaneous polarization P_s via the following expression [65]

$$d_{ij} = \epsilon_{il} Q_{jlk} P_{sk}, \tag{3.14}$$

where ϵ_{il} is the dielectric constant and Q_{jlk} is the electrostriction coefficient. A uniform electric field applied along the polar direction results in the elongation of the domains with polarization parallel and contraction of the domain with polarization opposite to the applied field. The field-induced strain (S) can be written as [66]

$$S = \frac{\Delta Z}{Z} = \pm d_{33} E, \tag{3.15}$$

where

$$\Delta Z = \pm d_{33} V. \tag{3.16}$$

Here Z and ΔZ are the sample thickness and deformation respectively and V is the applied voltage. The $\pm$ sign represents piezoelectric coefficients with opposite domains (parallel and antiparallel). In the case of transversally isotropic materials such as perovskite ferroelectrics, $d_{ij} \approx d_{33}$ [66]. A voltage modulation approach allows imaging of the dynamic piezoresponse with high sensitivity. An AC voltage $V_{ac} = V_0 \cos(\omega t)$ is applied to the surface of the ferroelectric sample with a conducting tip, and the deformation is measured using a standard lock-in technique by detecting

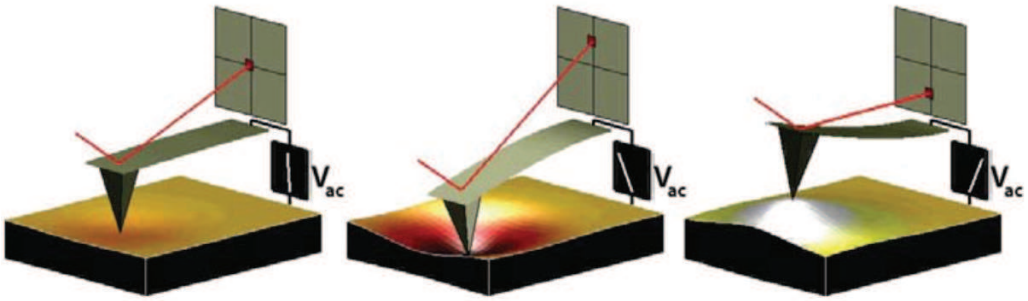

Figure 3.13: Schemtaic of PFM operation. In response to the application of an external electric field, the sample deforms locally which causes a cantilever deflection. Such response is due to the piezoelectric properties of the sample [67].

the vertical deflection of the tip as shown in the figure 3.13. The piezoelectric response of the sample is detected as the first harmonic component of the tip deflection (normal surface vibration, vertical piezoresponse) to obtain domain maps of amplitude and phase

$$\Delta Z = d_{33} V_0 \cos(\omega t + \phi), \tag{3.17}$$

where ϕ is the phase difference between the applied voltage and piezoresponse, and provides information on the polarization direction of the domain. The positive domain (polarization vector oriented downward) will vibrate in phase ($\phi = 0°$) with the applied modulation voltage whereas the negative domain (polarization vector oriented upward) will vibrate in counter phase ($\phi = 180°$) with the applied modulation voltage [67].

PFM measurements on $NaMnF_3$ were performed at room temperature using Asylum Research MFP-3D AFM system. Platinum coated Si cantilevers (Olympus OMCL-AC240TM) were used as a conducting tip in the measurements.

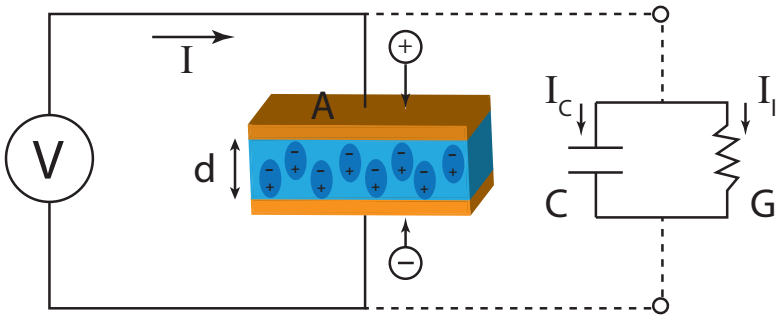

Figure 3.14: Parallel plate capacitor in an AC field (inspired by [44]).

3.3.9 Dielectric Measurement

A dielectric is a good insulating material that has an ability to store energy. A DC electric field will polarize the dielectric material by inducing dipole moments towards the field. The induce dipole moments by the field increase the capacitance by offsetting charges at the electrodes (decreases the effective electric field between the electrodes). The capacitance between the electrodes with the dielectric material is proportional to the dielectric constant. The capacitance of a parallel-plate capacitor with the dielectric material can be expressed as

$$C = \epsilon C_0, \tag{3.18}$$

with

$$C_0 = \epsilon_0 \frac{A}{d}, \tag{3.19}$$

where ϵ is dielectric constant or permittivity of the material, ϵ_0 is the permittivity of free space (vacuum), C and C_0 are capacitance with and without the dielectric, and A and d are the area of the capacitor plates and the distance between them.

When a sinusoidal AC field is applied across the capacitor with a dielectric, the

total current is made up of charging current I_c and loss current I_l [44] (see figure 3.14) which are related to the dielectric constant. Mathematically this can be expressed as

$$I = I_c + I_l = V(i\omega C + \frac{1}{R}). \tag{3.20}$$

We also know $\epsilon = \epsilon' - i\epsilon''$. Now substituting expressions 3.18 and 3.19 into equation 3.20, we get the total current as

$$I = V(\omega C_0 \epsilon'' + i\omega C_0 \epsilon' + 1/R). \tag{3.21}$$

The total current is made-up of real and imaginary parts

$$\begin{aligned} I'(\omega) &= \omega C_0 \epsilon'' V + V/R \\ I''(\omega) &= \omega C_0 \epsilon' V. \end{aligned} \tag{3.22}$$

The real and imaginary parts of the current are usually obtained from the direct measurement of the sample. Expression 3.23 can be easily manipulated to obtain an expression for the real and imaginary parts of the dielectric constant

$$\begin{aligned} \epsilon' &= \frac{I''(\omega)}{\omega}\frac{1}{C_0 V} \\ \epsilon'' &= [I'(\omega) - I(0)]\frac{1}{\omega C_0 V}, \end{aligned} \tag{3.23}$$

where $I(0)$ is due to DC conductance (current through the dielectric when $\omega \to 0$).

The dielectric measurement on NMF sample was performed using a SR 7265 Dual Phase DSP lock-in amplifier manufactured by Stanford Research used with a current sensitive preamplifier model 181 manufactured by Princeton Applied Research. Though the frequency range of the device is from 1 mHz to 250 kHz, measurements were performed from 100 Hz to 100 kHz since there was a drift in the measurements at the higher frequency. All the measurements were carried out using a small AC

voltage of 10 mV and 100 mV. Measurements were performed only on the $NaMnF_3$ film which was grown on top of $SrRuO_3$.

Chapter 4

Multiferroicity on $NaMnF_3$ Thin Films grown on $SrTiO_3(001)$

4.1 $SrTiO_3$

$SrTiO_3$ (STO) is an extensively studied material in solid state physics and material science mostly due to its interesting lattice dynamics at low temperatures. STO is a cubic perovskite at room temperature with $Pm\bar{3}m$ space group and undergoes a structural transition to an *I4/mcm* tetragonal phase below 110 K [68, 69] due to condensation of a soft phonon mode. Very subtle tilting of Ti-O octahedra (see figure 4.1 (d)) leads to almost doubling of the c-axis during the structural transition [68].

Another interesting property of STO at low temperatures is the increase of dielectric constant. The dielectric constant of STO starts to peak at around 35 K and level off at around 4 K as $T \to 0$ [70] due to quantum fluctuations of the po-

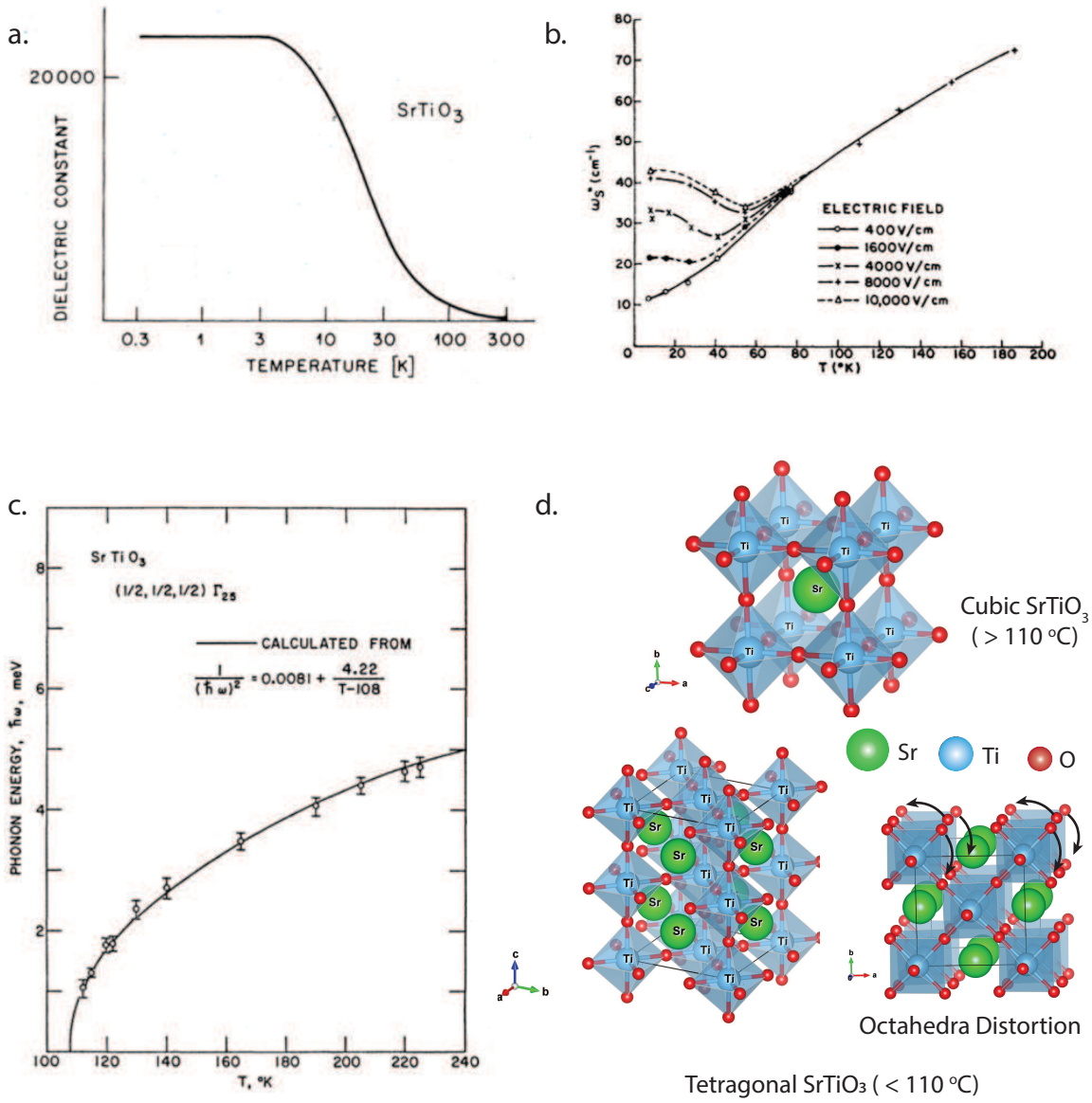

Figure 4.1: Properties of bulk $SrTiO_3$: (a) Quantum paraelectric properties below 4 K [70], (b) Condensation of soft mode as a function of temperature at various applied fields [71], (c) Temperature dependence of Γ-mode above the structural transition [68] d) Structural transition from cubic $Pm\bar{3}m$ to tetragonal $I4/mcm$. Arrows show the octahedra tilts and distortions. Inspired by [68].

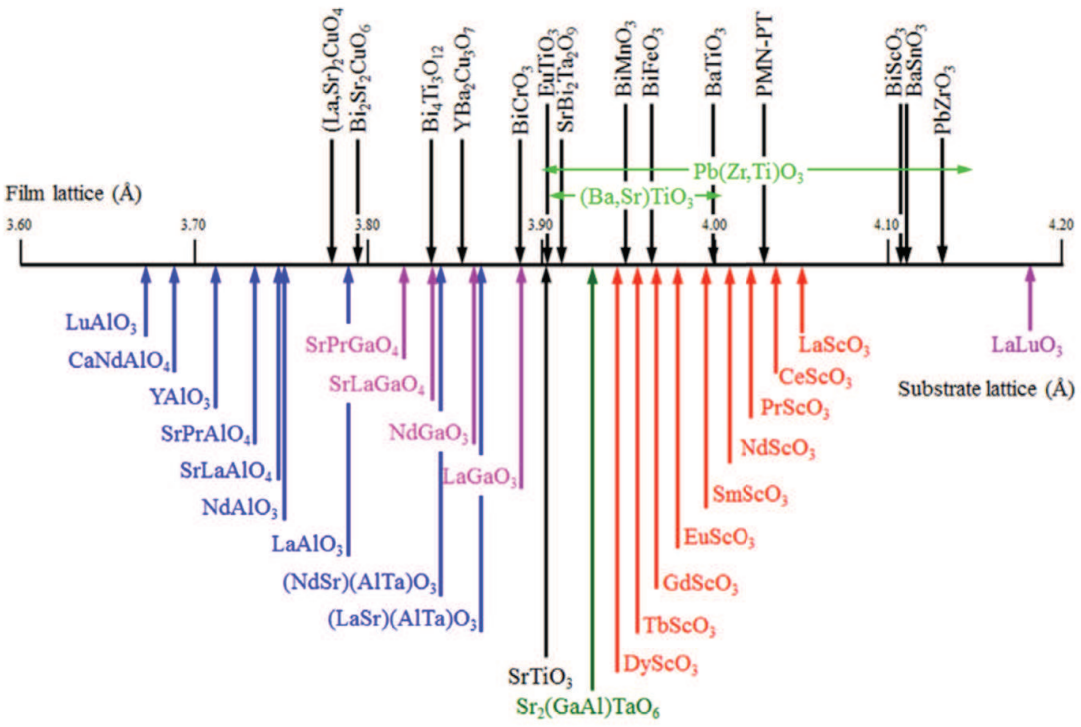

Figure 4.2: Pseudocubic lattice parameter of perovskite and perovskite-related films and substrates. Reproduced from reference [75] and reference within.

sitions of Ti ions in the unit cell [70]. However, the ferroelectric transition in STO is suppressed [70–72]; it is quantum paraelectric material. STO is also also called an incipient ferroelectric due to the soft mode behavior which causes it to approach ferroelectric transition as $T \to 0$. Quantum paraelectric phase is very sensitive to the lattice dynamics. A small change in the lattice can induce ferroelectric transition. Interestingly in the bulk STO, ferroelectricity has been induced by Ca doping [73] and electric [71] or mechanical stress [74].

At room temperature, STO has cubic lattice parameter of 3.905 Å. It is an ideal substrate for many perovskite films (see figure 4.2). Distorted perovskite $NaMnF_3$ has pseudocubic lattice parameter of 3.995 Å. As such, the growth of $NaMnF_3$ on

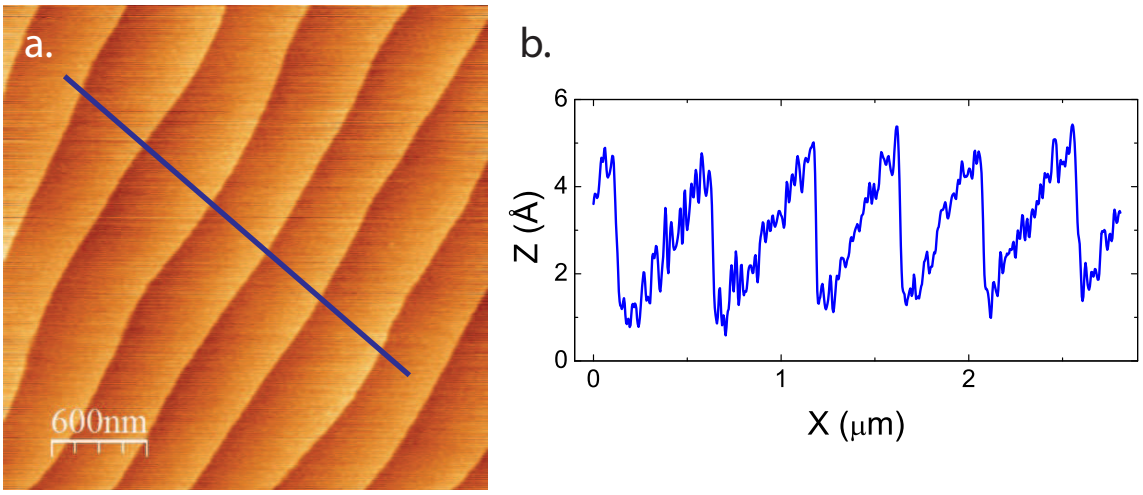

Figure 4.3: AFM topography on STO after thermal annealing and DI water treatment: (a) 3 μm $\times$ 3 μm image of STO. Blue line is drawn in the image to extract the line profile. (b) Line profile showing the terraces height of unit cell of STO.

STO would have a compressive strain of around 2.3%.

4.1.1 Structural, Magnetic and Electrical Characterizations

One side polished $10\times5\times1$ mm^3 STO(001) single crystal substrates were obtained from MTI Crop. An atomically flat surface on the substrate is one of the critical steps in the thin film growth to prepare well-characterized samples with reproducible results. Moreover, a well-defined interface between substrate and film can lead to some novel properties present neither in the thin film nor in the substrate materials. For example, two dimensional electron gas has been observed in $SrTiO_3/LaAlO_3$ interface [76]. In 1994, Kawasaki et al. showed that atomically flat surface on STO(100) with terraces of unit cell height can be prepared with buffered NH_4F-HF (BHF). Moreover, the surface had a single termination of a TiO_2 layer. Such well-defined surface provided atomically regulated epitaxial growth for complex oxide [77].

Typically the atomically flat surface on STO is prepared by acid based etchant [77, 78]. With these acid-based methods, there are always some safety issues one has to consider. However, in 2012 Connell et al. showed an acid-etchant-free technique to prepare the atomically flat surface with single TiO_2 termination on STO(001) and STO(111). This method involves two thermal annealing steps with water leaching step in between [79]. In the first step, STO is annealed in air at 1000 °C for an hour. Substrates are then leached in DI water for 30 seconds. At the final step, substrates are again annealed in air at 1000 °C for an hour. Commercially available STO has both SrO and TiO_2 termination on the surface. However, becuase only SrO is water soluble [80], it is possible to obtain just TiO_2 terminated STO surface with thermal annealing and DI water treatment.

Figure 4.3 (a) shows the 3 μm $\times$ 3 μm AFM topography image of atomically flat STO substrate prepared using an acid-free method. The surface topography shows the formation of terraces with typical width from 300 to 800 nm which is consistent with data presented by Connell et al. and other acid-based methods. Most importantly, the step height was found to be the same height of STO unit cell, i.e., 3.9 Å (please see the line profile graph figure 4.3 (b)). The RMS roughness of the surface was found to be typically around 1.4 Å. This shows that the new acid-free method of preparing atomically flat STO(001) substrate purposed by Connell et al. is reproducible.

Figure 4.4 shows RHEED and XRD of the bare STO(001) after the surface treatment. XRD does not show any impurities peaks. RHEED pattern shows specular spots with visible Kikuchi lines which indicates the surface of the STO is very smooth after the surface treatment.

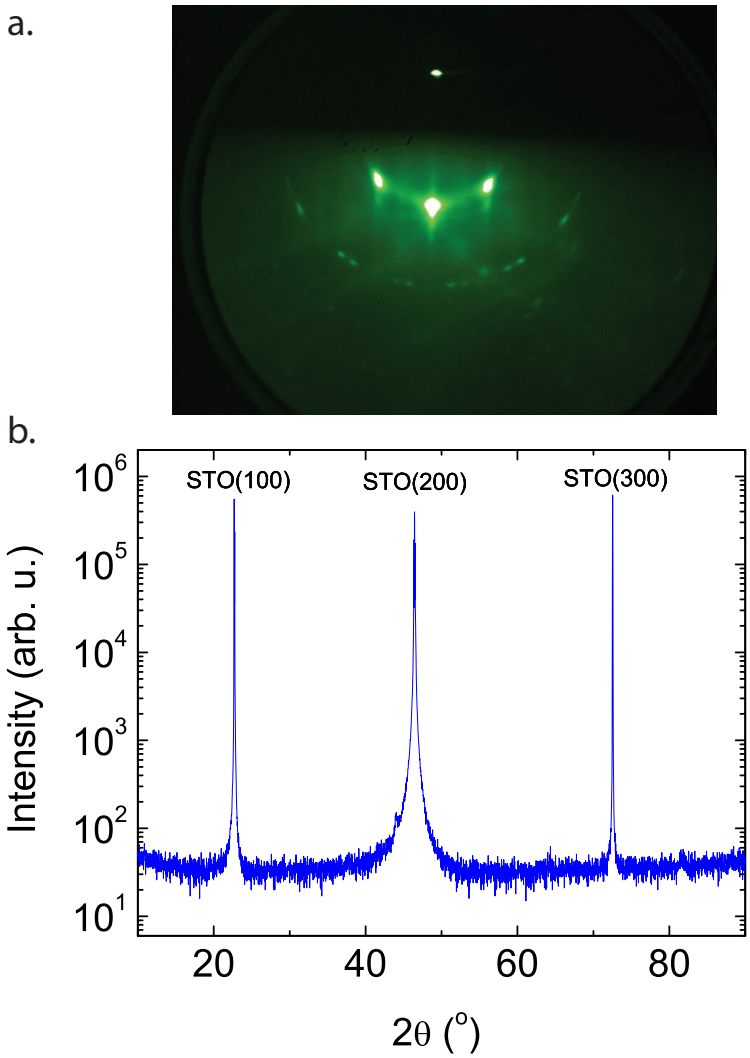

Figure 4.4: Structural characterization of STO after thermal annealing and DI water treatment: (a) RHEED image just before NMF growth (b) X-ray diffraction on blank STO.

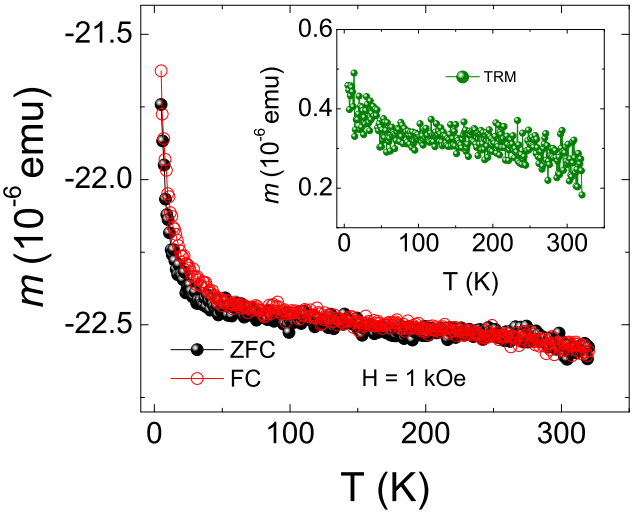

Figure 4.5: Magnetic characterization of precut $10 \times 5 \times 1$ mm^3 STO(001). Magnetic moment m as a function of temperature: ZFC and FC curves showing some magnetic nature at a low temperature most likely due to the presence of magnetic impurities. Inset show TRM measurement.

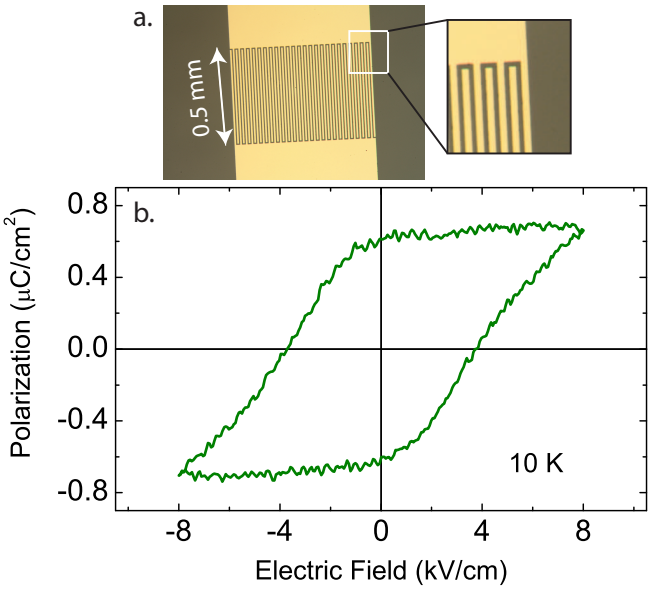

Figure 4.6: Ferroelectric characterization on precut $10 \times 5 \times 1$ mm^3 STO(001) substrate: (a) Microscope image of interdigitated electrodes on STO surface for in-plane ferroelectric measurements. The fingers have 0.5 mm length and 5 μm gap. (b) Averaged remanent polarization vs. electric field at 10 K with the remanent polarization of 0.6 μC/cm^2.

The temperature-dependent magnetization measurements on STO were carried out by first cooling the samples from room temperature to 5 K in $H = 0$, and then measuring the magnetic moment m as a function of T in $H = 1$ kOe applied in-plane along the STO [001] direction while warming up to 320 K (zero-field cooled, ZFC). Then the measurements were continued while cooling in the same H down to 5 K (field cooled, FC). Subsequently, the thermoremanent magnetization (TRM) was measured while warming in $H = 0$. Figure 4.5 shows FC and ZFC measurements. The ZFC-FC curves track each other without any significant splitting (or hysteresis) in the temperature range measured. At low temperature ($< \ 100\ K$), these curves show small Curie-like upturn ($1/T$ dependence). The upturn is most likely due to the presence of different sources of magnetic impurities (such as Fe, Co, and Ni) close to ppm level in the substrate [81]. TRM measurement (figure 4.5, inset) does not show any unusual signal and remains below 5×10^{-7} emu range throughout the temperature measured. However, it was found that the diamagnetic background slightly differs from one substrate to another, but the qualitative nature of ZFC, FC, and TRM curves remained the same.

Our plan was to grow $NaMnF_3$ on STO(001) to check whether the films are ferroelectric. As such, Pt interdigitated electrodes were transferred to STO surface using photolithography (see picture 4.6 (a)) before growing 50 nm of $NaMnF_3$. Polarization vs. electric field was measured using Precision LC ferroelectric tester. Measurements were performed at low temperature to minimize leakage current. The remanent hysteresis loops were measured to avoid any non-ferroelectric switching effect from the sample and the cables. The sample showed sizable hysteresis loop with remanent

polarization (P_r) ~ 0.5 μC/cm^2. The loops develop until 50 K, but above this temperature, no sizable loop could be measured. Hysteresis loops were again measured on bare STO to check whether the switching signals are from the substrate. Surprisingly, STO was found to have hysteresis loop with even larger remanent polarization ($P_r \sim 0.6$ μC/cm^2) at 0.1 kHz at 10 K (figure 4.6 (b)). The coercive field (P_c) was determined to be 3.7 kV/cm. The shape and size of the hysteresis loops (P_c and P_r) were independent of applied frequency, and sizable loops were measured until 50 K. These results indicate that STO substrates have ferroelectric or relaxor ferroelectric behavior which contradicts the quantum paraelectric nature of bulk STO. It has been previously shown that STO can be ferrelectric by doping [73, 82, 83] or a minute Sr deficiency [84]. Previous studies have shown that the small perturbation created in the lattice by chemical or mechanical stress is enough to bring about structural instabilities (soft phonon mode freezes) in the quantum paraelectric state of STO, thus driving the system through a ferroelectric transition [73, 74, 82, 85]. Such phenomena have also been observed in structurally similar quantum paraelectric $KTaO_3$ [86–88]. The presence of defects and magnetic impurities (as indicated in the low-temperature region of the magnetic measurement, figure 4.5) most likely contributed to the polar nature of these STO substrates. However, further investigation is needed to understand the ferroelectric nature of the substrate with the in-plane electric field.

4.2 $NaMnF_3$

Perovskite crystals (ABX_3: X = O or F) represent one of the most widely studied material group with many technological applications [6, 89]. The range of proper-

ties include but is not limited to (anti-) ferroelectricity [7], (anti-) ferromagnetism [90], multiferroicity [91], magnetoelectricity [92], piezoelectricity [93] and metal-to-insulator transitions [94]. $NaMnF_3$ (NMF) is a distorted orthorhombic perovskite at room temperature and belongs to *Pnma* space group. The distortion from ideal perovskite is due to tilt and rotation in MnF_6 octahedra [10]. Ratuszna et al. reported the experimental orthorhombic lattice parameters as: $a_o = 5.751$ Å, $b_o = 8.008$ Å, and $c_o = 5.548$ Å. In the pseudo-cubic unit cell, the corresponding lattice parameters are $a_{pc} = c_{pc} = \sqrt{a_o^2 + c_o^2}/2 = 3.995$ Å and $b_{pc} = b_o/2 = 4.004$ Å. The tilting in the octahedra using Glazer notation [95, 96] has the sequence $a^- b^+ a^-$ in NMF. The sequence of the symbols corresponds to the tilt along the crystallographic axes, in other words, first tilt along a, second along b and third tilt along c. The superscripts indicate tilts of subsequent layers of octahedra such that zero tilt as '0', in-phase tilt as '+' and anti-phase tilt as '-'. Repeating characters in the sequence represent the same amplitude of tilt. In case of NMF, MnF_6 octahedra tilt along a and c have equal magnitude and are in-phase whereas tilt in b is anti-phase. In addition to the octahedra tilts and distortion, there is A-site (Na) displacement in NMF. This kind of system is commonly referred as $GdFeO_3$-type perovskite.

The common type of structural distortions in perovskite give rise to the ferroelectricity (B-cite off-centering such as in $BaTiO_3$, figure 2.8) and deformation of BX_6 octahedra (*Pnma* space group, figure 4.7 (a)). However, there is a stiff competition between these two type of deformations. The antiferrodistortive zone boundary instability corresponds to the tilts and rotation of the BX_6 octahedra and tries to suppress ferroelectricity in perovskite structure [97, 98]. As a result, there are few

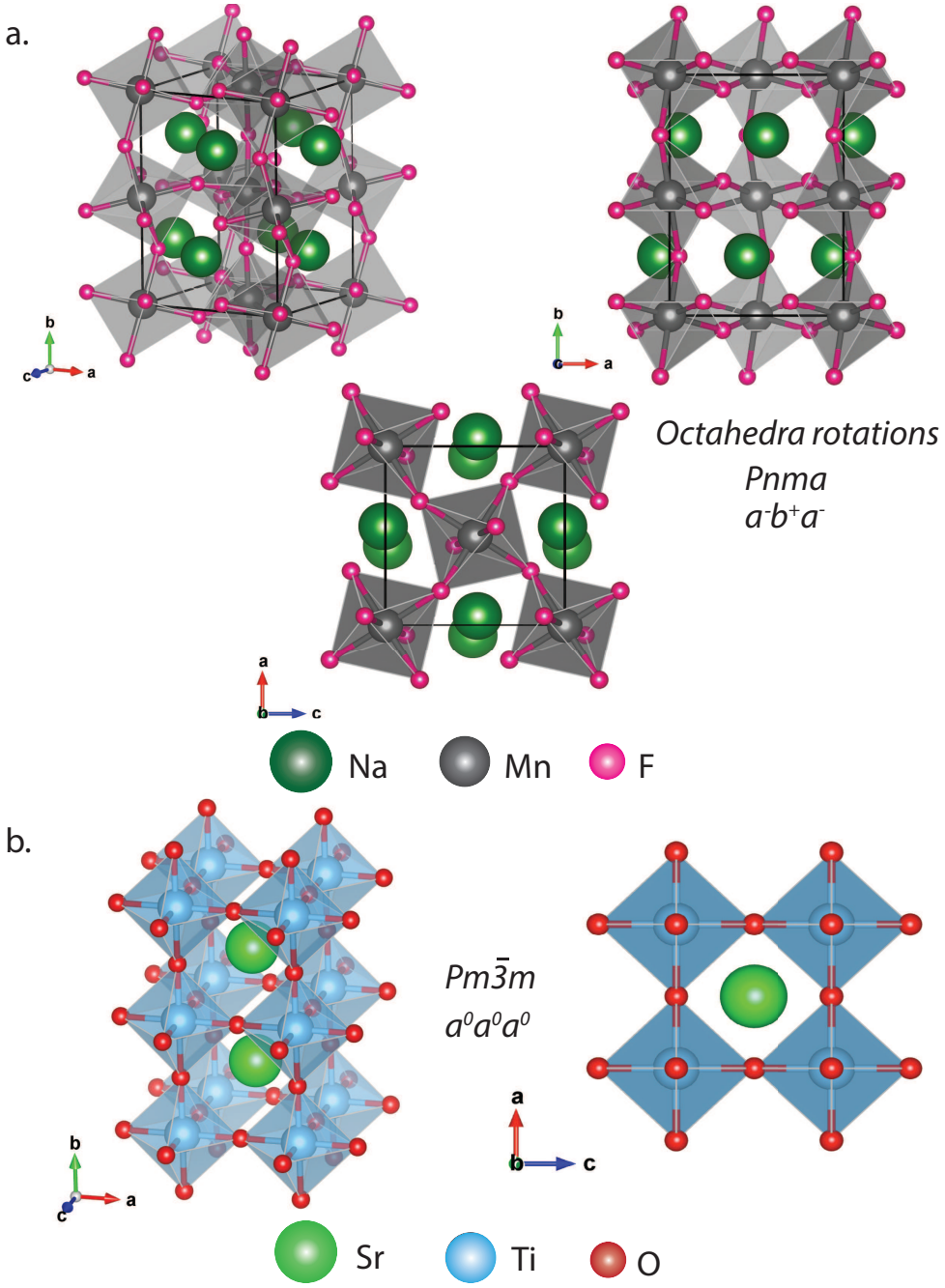

Figure 4.7: Comparison of perovskite with and without octahedra tilts. (a) $NaMnF_3$ octaherdra tilts are one of the most commonly occurring structural distortions in perovskite with the corresponding Glazer tilt sequence, $a^-b^+a^-$. (b) Cubic $Pm\bar{3}m$ perovskite ($SrTiO_3$) with corresponding Glazer pattern, $a^0a^0a^0$, has no tilts. Here on the left two unit cell of $SrTiO_3$ along b crystallographic axis is shown for comparison with an orthorhombic $NaMnF_3$ unit cell.

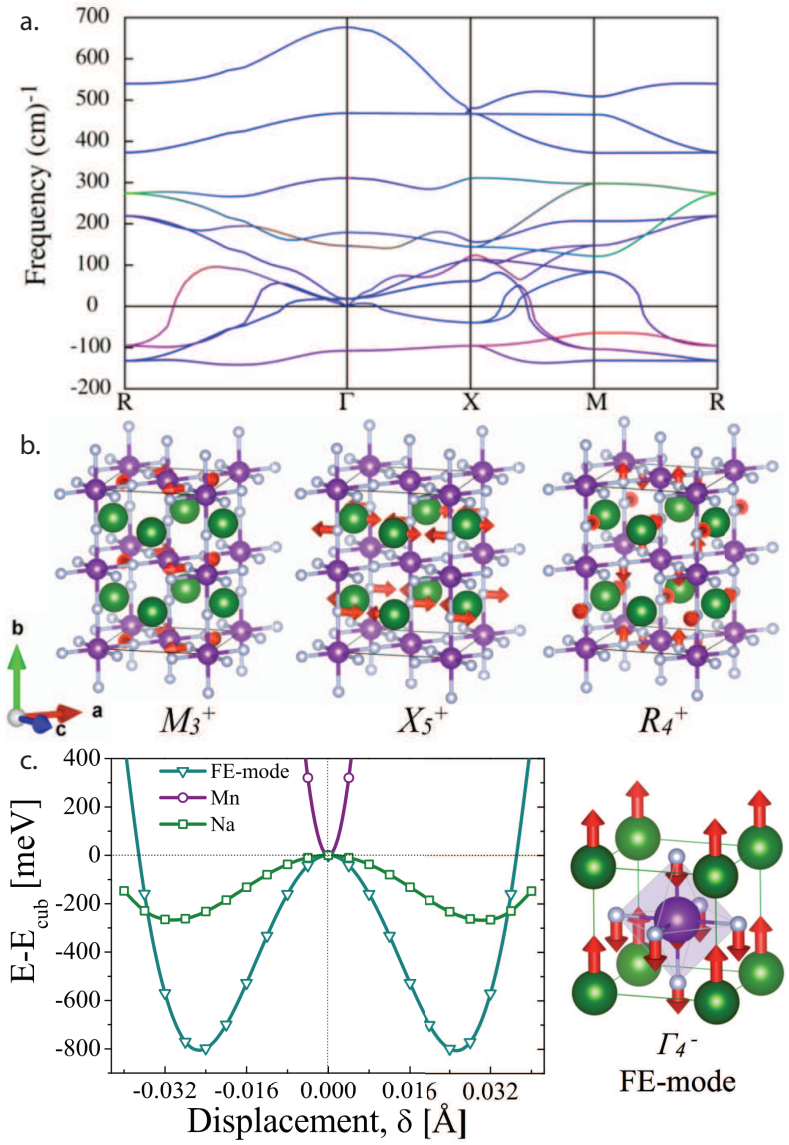

Figure 4.8: (a) Phonon-dispersion curves of cubic $NaMnF_3$. The instabilities are at points M, R, X, and Γ. The M and R instabilities correspond to octahedral rotations. The X instabilities correspond to the antipolar displacement of A-cation whereas the Γ-point instability corresponds to a polar/ferroelectric distortion. The branch colors are assigned according to the contribution of each atom to the dynamical matrix eigenvector: red for Na, green for Mn, and blue for F. (b) the eigendisplacements at M, X, and R for the modes that contribute most to the fully relaxed ground state are shown. (c) Energy as a function of displacement for $NaMnF_3$ for three different displacement patterns: The purple, green and blue lines correspond to eigendisplacement of Mn ion, Na atom and the FE soft mode (also shown in the right) respectively. Reproduced from reference [11].

perovskite ferroelectrics. Similar to oxide counterparts, such competition in ABF_3 can be expressed in terms of tolerance factor t,

$$t = \frac{R_{A-X}}{\sqrt{2}R_{B-X}}. \tag{4.1}$$

where R_{A-X} and R_{B-X} are the bond lengths of $A-X$ and $B-X$ in ABX_3 structure [99]. Therefore, t is the measure of ionic size effect on ABX_3 material. In perovskites with t < 1 (e.g., $0.78 < t$ belongs to $R3c$ space group and $0.78 < t < 0.88$ belongs to $Pnma$ group; both of which are the non-polar group), the octahedra deformation suppresses the ferroelectricity whereas for $t \sim 1$, opposite is true, i.e., ferroelectricity suppresses the antiferrodistortive instabilities [11, 97].

A recent computation work by Garcia-Castro et al. showed that NMF has a soft ferroelectric mode if lattice parameter $a = c$. Such condition, for example, can be achieved by growing epitaxial NMF thin films on an appropriate cubic substrate. Figure 4.8 shows the phonon dispersion curves of cubic NMF from first principle calculations. In its ground state, NMF embraces the $Pnma$ structure due freezing-in a combination of the rotation instabilities at the Brillouin zone boundary M and R points (which are antiferrodistortive out-of-phase and in-phase octahedra rotations, respectively). However, figure 4.8 shows that NMF cubic phase is unstable due to the presence of zone-center (Γ-point) instability which leads to polar/ferroelectric distortion. Such zone-center instability is absent in the $Pnma$ phase of NMF. Surprisingly, this soft mode remains unstable until R point [11].

The soft polar mode B_{2u} freezing results in a structural transformation from the non-polar $Pnma$ to the polar $Pna2_1$ space group which causes a polarization of $P =$ 6 μC/cm^2 along the long axis b. Choosing 0% strain reference as $a_r = \frac{a_o+c_o}{2}$ (where

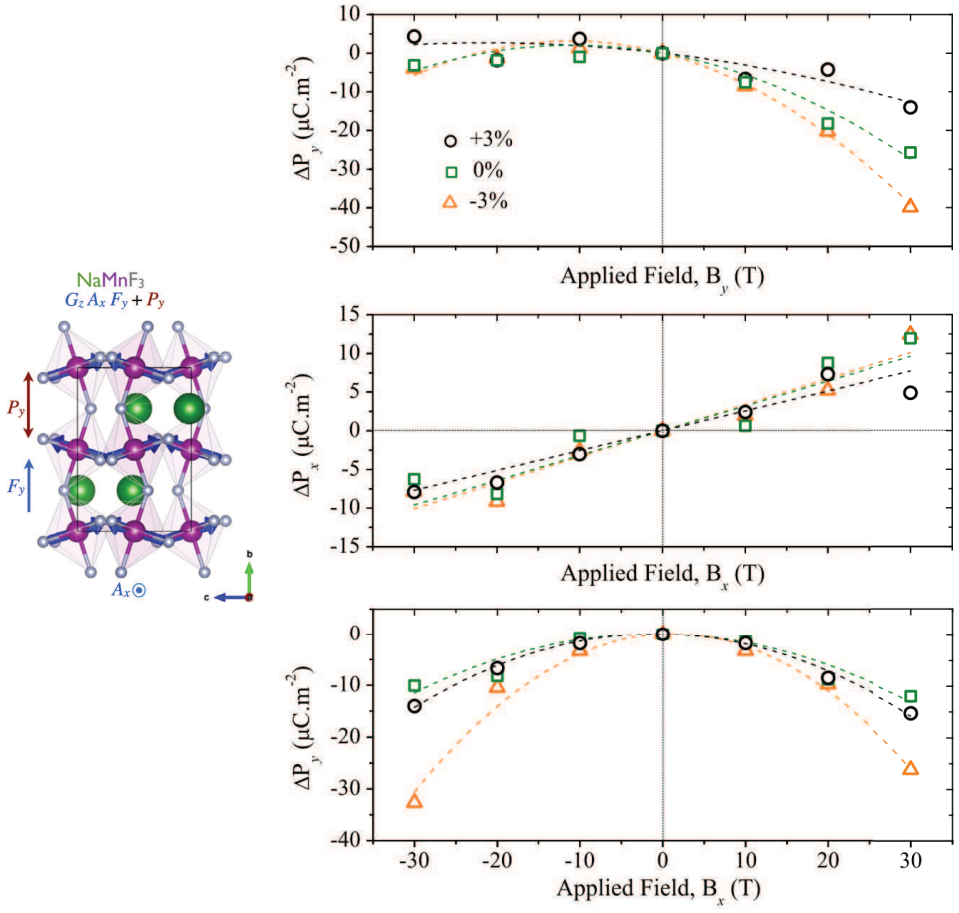

Figure 4.9: Change of polarization (ΔP_i) as a function of magnetic field in strained $Pna2_1$ NMF phase. Non-linear behaviors were observed for field applied along x and y directions. Reproduced from reference [11].

a_o and c_o are the relaxed lattice parameter of $Pnma$ phase), it was also shown that P can be enhanced by negative or positive strains (12 μCcm^2 at +5% strain 9 μC/cm^2 at -5% strain) [11, 12].

In bulk, NMF exhibits G-type antiferromagnetism (all the neighboring moments are antiparallelly aligned in the unit cell, see figure 2.3) of the Mn magnetic moments centered within tilted MnF_6 octahedra, with additional weak ferromagnetic canting [10, 100, 101]. The Néel temperature has been reported to be $T_N = 66$ K [100–105].

Interestingly, quantitative magnetization measurement on bulk NMF has not yet been reported to the best of our knowledge.

The ferroelectricity in the NMF cubic phase is due to the displacement of A-site Na ion. The eigendisplacement η of Na at the zone center is computed to be 0.174 whereas it just 0.003 Å for Mn ion [11]. Due to the presence of antiferromagnetic and ferroelectric long-range ordering, NMF is multiferroic under isotropic epitaxial strain. As dicussed earilier in the chapter 1, in most of the materials with perovskite structure, the simultaneous presence of magnetic and electric order is limited by conflicting requirements for the d^n electronic configuration of the transition metal in the B-site [7]. Ferroelectricity in perovskite favors d^0 (empty d-shell) electronic configuration in B-site metal ion (for example, in the case of Ti_4^+, Nb_5^+, and Ta_5^+). The unoccupied d states in these transitional metal ion tend to hybridize with neighboring ions which support off-centering of the B-site ion in the unit cell. In contrast, long-range magnetic ordering requires partially filled d-shell. Due to such conflicting requirements, there are very few magnetoelectric materials. However, ferroelectricity in cubic NMF has a geometric origin (Na displacement in the unit cell due to the geometrical effect), it is, therefore, likely to have a magnetoelectric effect.

Figure 4.9 shows the calculated change of polarization as a function of the magnetic field by Garcia-Castro et al. Both linear and non-linear magnetoelectric effects were observed depending upon the direction of the applied magnetic field along the crystallographic axis. Surprisingly, non-linear contributions dominate over the linear response, and the later one is comparable to the magnetoelectric effect observed in Cr_2O_3.

In order to test the computational predictions, NMF films were grown *via* MBE. Growth optimization was performed at different substrate temperatures to obtain the best quality films. The crystallography of the substrate and film surfaces was monitored *in-situ* using reflection high energy electron diffraction (RHEED). Further crystallographic characterization was carried out *ex-situ* using X-ray diffraction (XRD) and X-ray reflectivity (XRR) techniques using a rotating anode source with a graphite bent crystal monochromator optimized for Cu K_α radiation. The surface morphology was studied by the atomic force microscopy (AFM). The best films were then further characterized via Reciprocal space mapping (RSM), SQUID magnetometry and piezo-response force microscopy (PFM).

4.3 Experimental Procedures

4.3.1 Growth

One side polished pre-cut ($10 \times 5 \times 1$ mm^3) STO(100) single crystal substrate obtained from MTI Crop. was used for this work. The STO surface was prepared as discussed in section 4.1.1. The growth of NMF was performed in MBE chamber using Knudsen cells (also called K-cells). NaF (99.99%) and MnF_2 (99.99%) were co-deposited to get stoichiometric NMF (please refer to section 3.1.1 for NaF and MnF_2 rates calculations). The rate of NaF was maintained at 70% of the MnF_2 rate during the growth ($R_{NaF}/R_{MnF_2} = 0.7$). The normal operating temperature of NaF and MnF_2 K-cells were $740-750$ °C and $770-780$ °C, and generated fluxes $\sim$ 0.028 Å/s and $\sim$ 0.040 Å/s respectively. Usually, the temperature of MnF_2 K-cell was kept

constant while slightly adjusting NaF K-cell temperature to get appropriate ratio of the rates. The rates were individually measured using QCM at the growth position.

Materials were co-deposited at elevated substrate temperatures to obtain epitaxial growth. To the best of our knowledge, there is no previously reported growth of NMF in thin film form which motivated us to perform growth optimization to achieve the best quality films. Same thickness (50 nm) films of NMF were grown at substrate temperature T_s ranging from 200 °C to 450 °C in 50 °C steps. The quality of the substrate and film surfaces was monitored *in-situ* using reflection high energy electron diffraction (RHEED). XRD and AFM were also used to determine the best growth conditions.

4.4 Result and Discussion

4.4.1 Structural Characterization

Figures 4.10 and 4.11 show the RHEED and AFM images of the 50 nm NMF films grown at different substrate temperature T_s. RHEED pattern indicates that the film surface and crystallinity degraded when the growth temperature was increased beyond 350 °C (figure 4.10). The films grown at T_s = 250 °C - 350 °C show streaky RHEED pattern which suggests the film is crystalline and coherent. However, the appearance of ring-like structures along with spots indicates rougher polycrystalline films at higher T_s. AFM images revealed the presence of large grains (almost $\sim$1 μm in width, and as tall as 50 nm) on the surface of the films grown at higher T_s (please see figure 4.11). Films grown at lower temperatures show a flat island-like structure

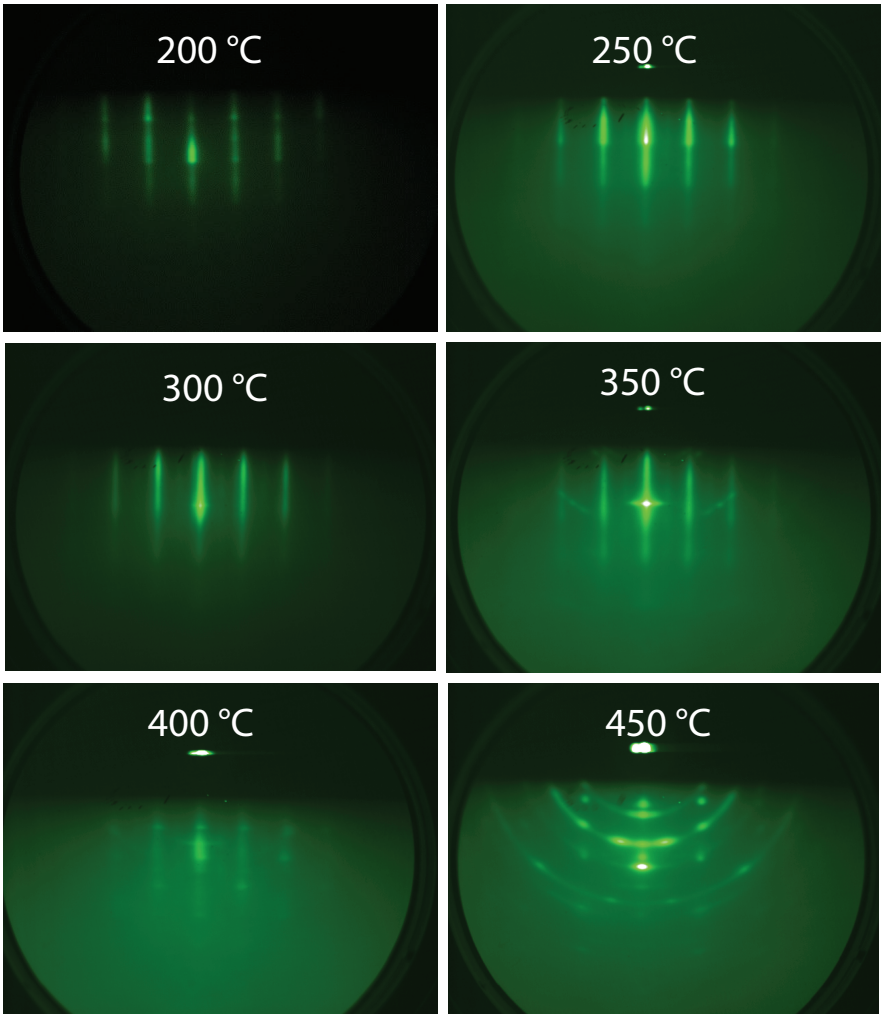

Figure 4.10: RHEED images of NMF films grown at different substrate temperatures. Above 300 °C, the patterns become spottier, and eventually circles appear at 450 °C. This indicates that the samples become rougher with increasing growth temperature, and eventually they become polycrystalline.

with trenches. These results indicate the surface, as well as the structural quality, degrades with the increase of substrate temperature.

In the following discussion, crystallographic directions and planes corresponding to Miller indices labeled as $[hkl]_{pc}$ and $(hkl)_{pc}$ correspond to the pseudo-cubic perovskite structure, while those labeled as $[hkl]_o$ and $(hkl)_o$ correspond to the orthorhombic

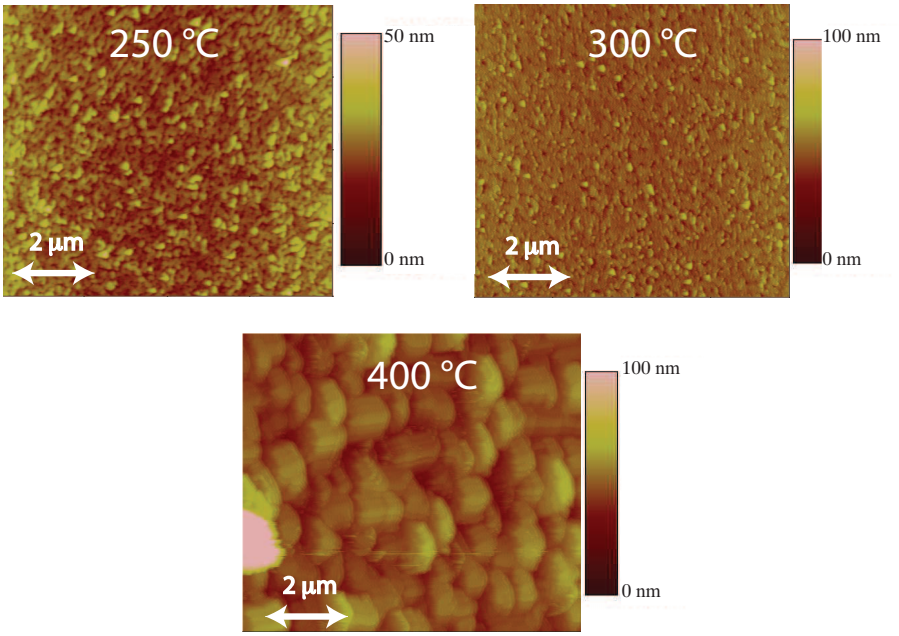

Figure 4.11: 10×10 μm^2 AFM topography images of NMF film grown at different substrate temperatures. Samples grown at 300 °C or less were smooth whereas films grown above 300 °C were very rough with big grains.

structure. Please see figure 4.12 (b)) to make a distinction between orthorhombic (o) and pseudo-cubic (pc) unit cell of NMF.

Films were further characterized using XRD. Figure 4.12 (a) shows out-of-plane XRD of the 50 nm films grown at different T_s. Films favored $[100]_{pc}$ out-of-plane growth orientation, same as the substrate. XRD shows intense reflections from $(100)_{pc}$, and $(200)_{pc}$ planes in all the films except on the one grown at the highest T_s (450 °C). However, films deposited at higher T_s (>300 °C) also reorientated along $[100]_o$ and $[110]_o$ directions in addition to $[100]_{pc}$, suggesting polycrystallinity on those films. $[100]_{pc}$ orientation is equivalent to both $[010]_o$ and $[101]_o$ of NMF. This observation is consistent with ring-like features seen on RHEED images on the films grown at higher T_s. Films grown at higher T_s were also found to have a broader

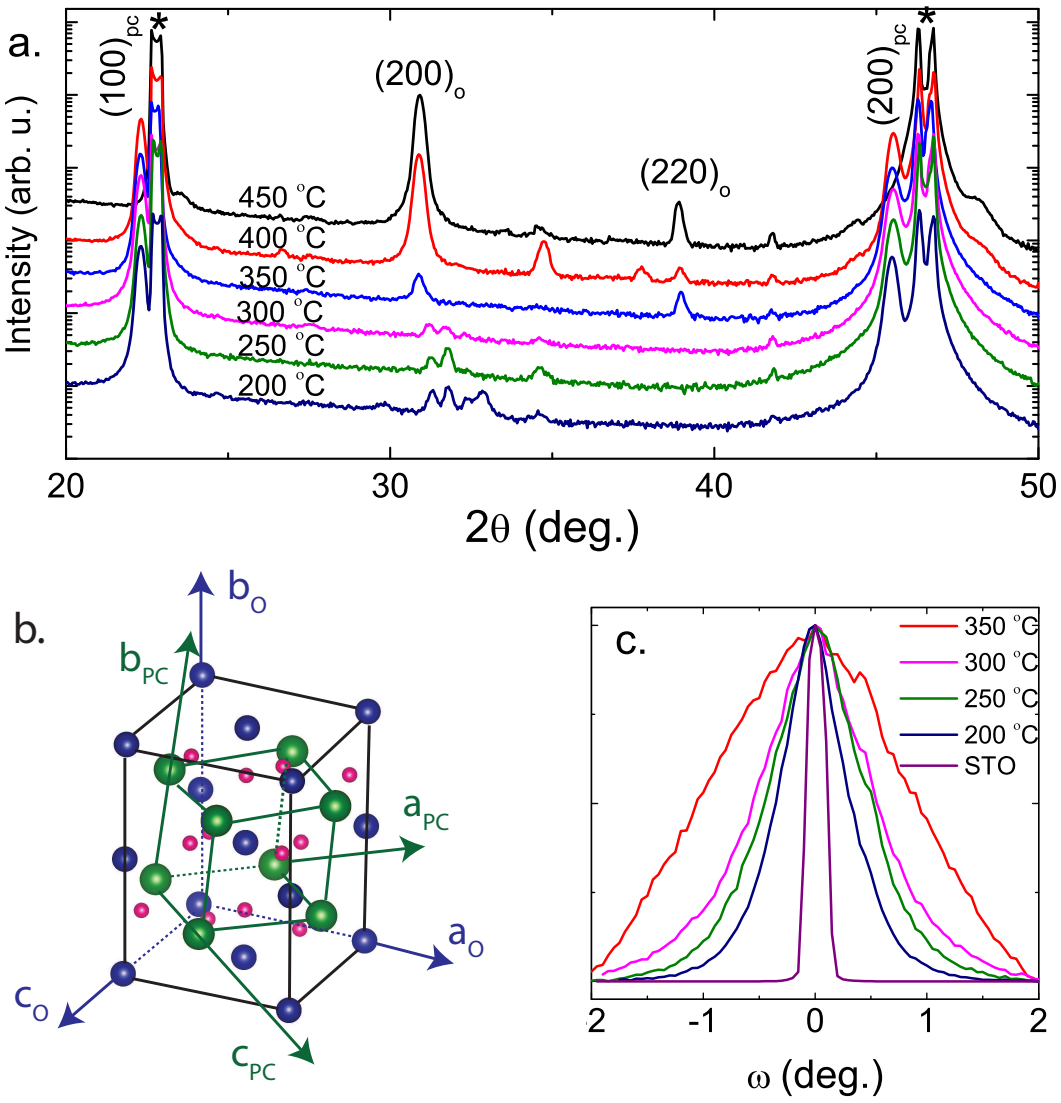

Figure 4.12: (a) Out-of-plane XRD vs. the growth temperatures of 50 nm NMF films grown on STO(100). Asterisk marked peaks are (100) and (200) peaks of STO. Note: double peaks seen in the substrate peak is due to the saturation of the intensity in the detector. (b) Schematic of NMF structure showing both orthorhombic (blue) and pseudocubic (green) unit cells [Na (green), Mn (blue) and F (pink)]. (c) Rocking curve of NMF films around $(200)_{pc}$ peaks.

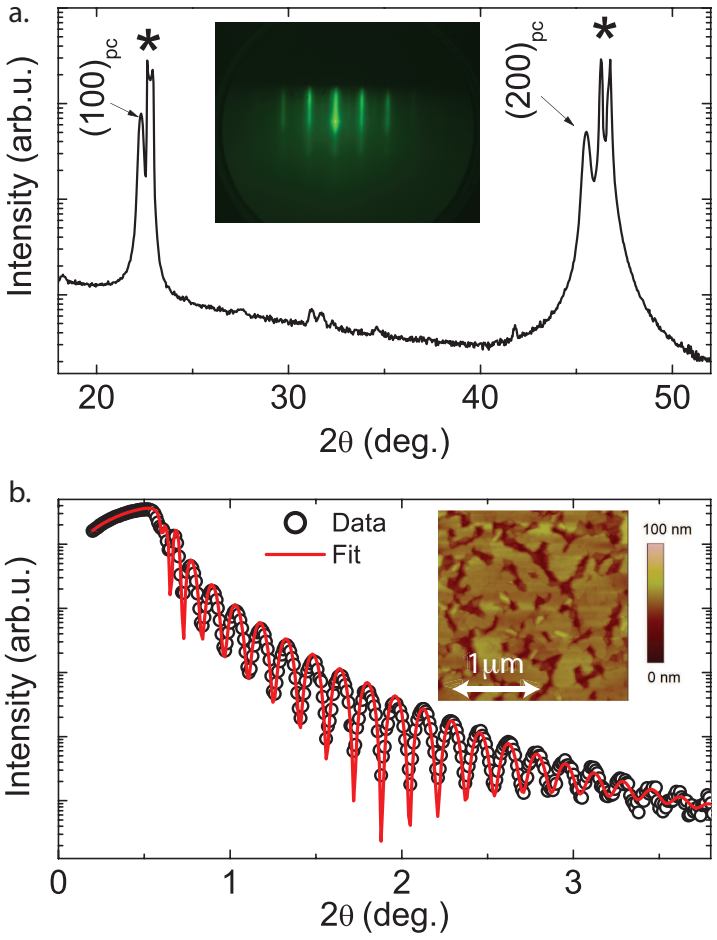

Figure 4.13: Out-of-plane XRD (a), XRR (b), RHEED (inset in a) and AFM (inset in b) of the 50 nm NMF film grown at 300 °C.

full width half maximum (FWHM) of rocking curves (figure 4.12 (c)). For example, film grown at 250 °C had FWHM of 1.01° while film grown at 350 °C had 2.87° with the Lorentzian fit which indicates the mosaic spread of the film increases while crystallinity decreases with a rise of the growth T_s. The rocking curve around the STO (200) substrate peak is also shown. The relatively broad (FWHM = 0.15°) rocking curve of the substrate peak is due to the limitation of instrument resolution. Note: double peaks in figure 4.12 (a) and marked by an asterisk correspond to substrate Bragg peaks distorted by saturation of the detector.

The best films grew between 250 °C − 300 °C as determined by RHEED, XRD, and AFM. Figure 4.13 (a) shows out-of-plane XRD film grown at 300 °C. XRR (figure 4.13 (b)) shows Kiessing fringes, and the data fit using GenX software indicates film thickness and roughness to be 51.8 nm and 0.41 nm respectively. AFM topography image (figure 4.13 (b) inset) of the film shows that the surface has very deep tranches ($\sim 20 - 25$ nm deep) but with smooth tops. The surface roughness of the 2×2 μm^2 image was found to be 7.7 nm because of island topography.

In order understand details of epitaxy, strain and growth orientation, XRD ϕ, off-axis $\theta - 2\theta$ and reciprocal space mapping (RSMing) scans were performed. Interestingly, only the reflections from orthorhombic *Pnma* phase of the film could be observed, indicating the absence of an $a = c$ distortion in the film. The reflections associated with b_o-axis pointing out-of-plane [NMF(010)/STO(001)] as well as in-plane [NMF(101)/STO(001)] domains were identified in the same film [the corresponding $(010)_o$ and $(101)_o$ lattice parameters are virtually identical and is equivalent to $(100)_{pc}$]. The out-of-plane lattice parameters were found to be 3.990 ± 0.001 Å,

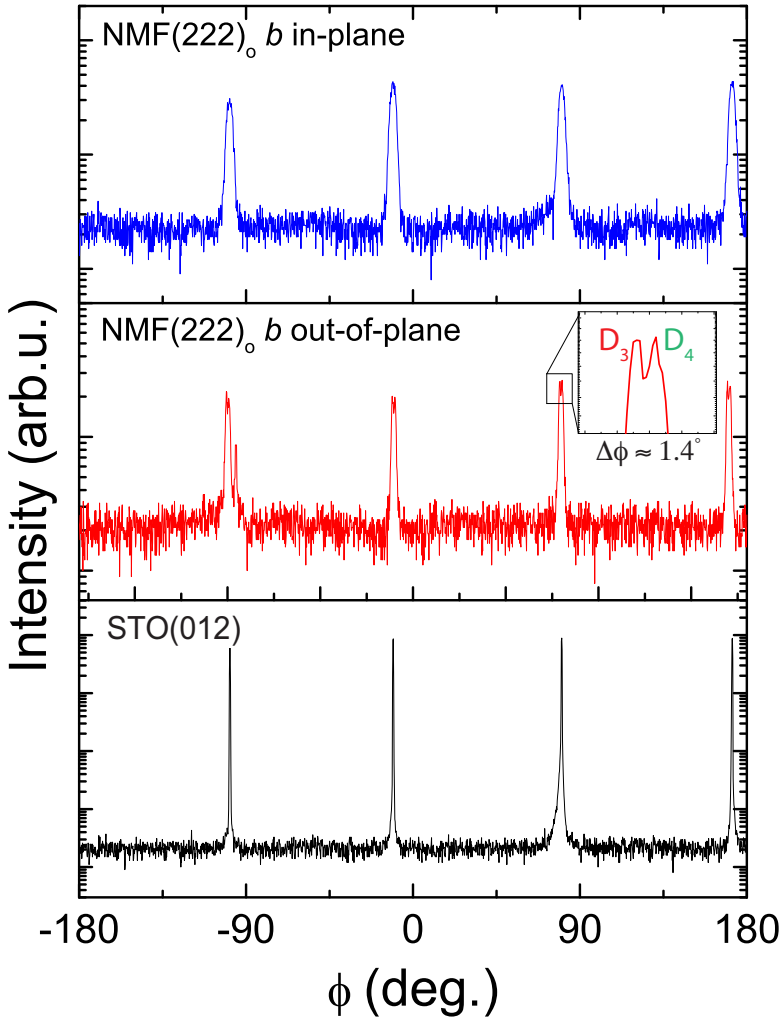

Figure 4.14: ϕ-scans of 50 nm NMF film on STO(001): ϕ-scans corresponding to (012) reflections (black curve, bottom panel) of the substrate, $(222)_o$ reflections of the NMF(010) domain (red, middle panel), and NMF(101) (blue, top panel) domain with χ (the angle between the scattering vector and surface normal) = 26.57°, 63.50°, and 26.50°, respectively. Middle panel inset shows a closeup of the NMF(010) domain indicating twinning of the $(222)_o$ planes.

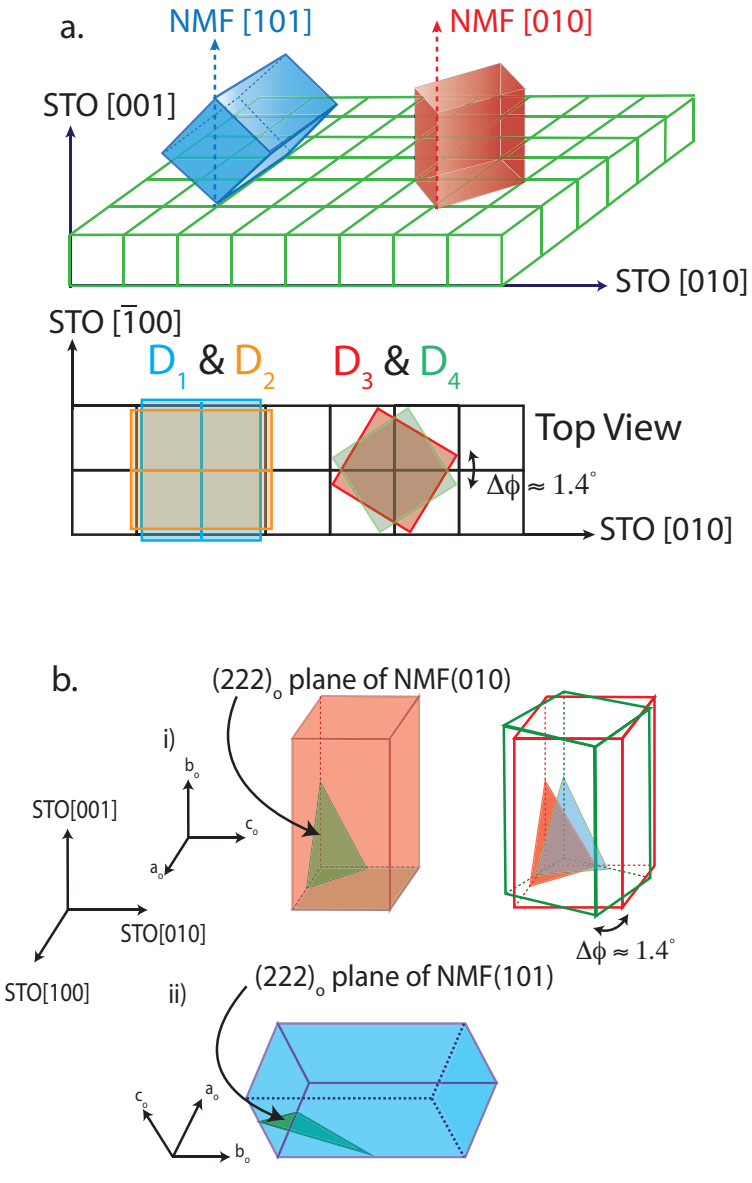

Figure 4.15: Schematic representation of the epitaxial orientation: (a) NMF(101) and NMF(010) domains on STO(001) with top views (bottom) as determined from ϕ-scans. (b) $(222)_o$ planes of the NMF(010) (i) (right figure shows twining of the (010) domain) and NMF(101) (ii) domains with their respective χ angle on STO(001).

Table 4.1: 2θ and χ angles for different planes of cubic STO(001) and orthorhombic ($Pnma$) NMF domains.

	Planes	2θ [deg.]	χ [deg.]
STO	(012)	52.36	26.57
	(103)	77.17	18.43
	(203)	90.76	33.69
NMF(101) domain	(222)	51.10	26.50
	(042)	56.67	65.09
	(323)	75.19	18.39
	(262)	87.98	56.24
NMF(010) domain	(222)	51.10	63.50
	(042)	56.67	35.82
	(323)	75.19	71.61
	(260)	79.08	24.86
	(062)	79.69	25.68
	(262)	87.98	33.76

3.984 ± 0.004 Å, 3.982 ± 0.002 Å, 3.986 ± 0.001 Å and 3.984 ± 0.002 Å for the NMF samples grown at T_s 200 °C, 250 °C, 300 °C, 350 °C and 400 °C respectively using Nelson-Riley fit. Systematic errors from the instrument were avoided by using expression $\Delta d/d = K(\cos^2\theta/\sin\theta)$ to fit data obtained using XRD. Extrapolating the calculated lattice parameter against $\cos^2\theta/\sin\theta$ with linear fit yields true lattice constant [106].

It should be noted that the angle χ (tilt angle with respect to the surface normal)

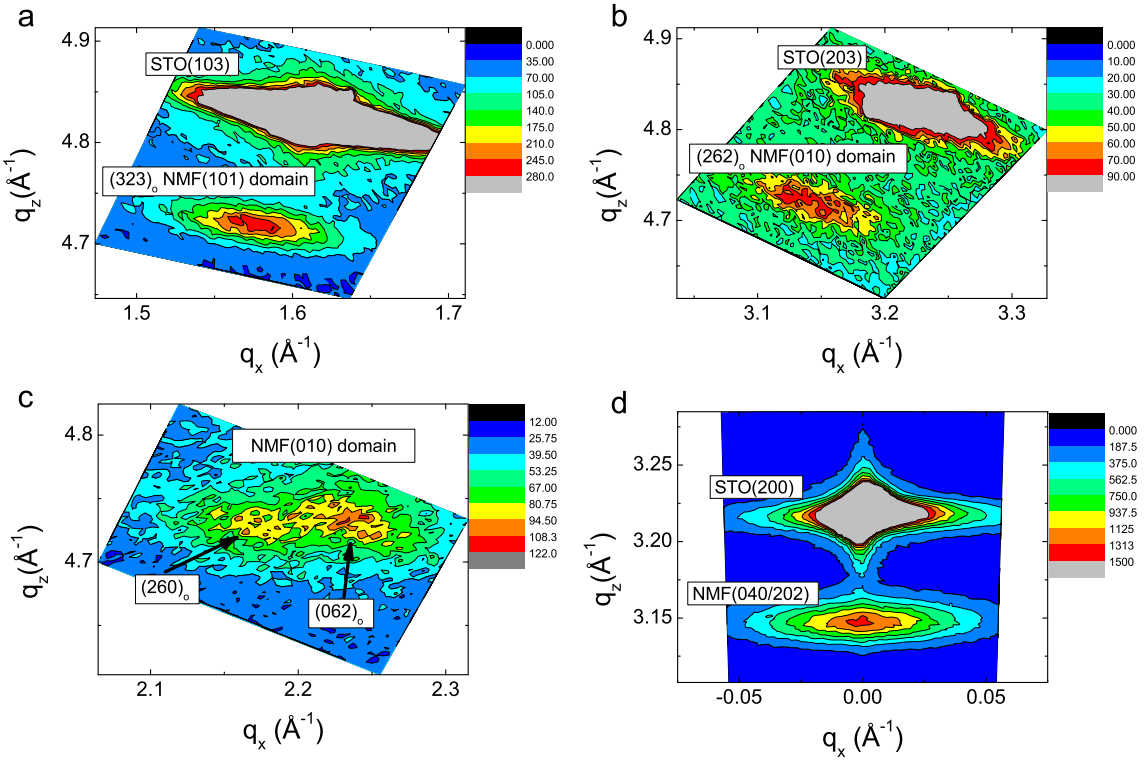

Figure 4.16: Reciprocal space maps of 50 nm NMF on STO: (a) Reciprocal space map (RSM) around $(323)_\circ$ plane of NMF with (101) out-of-plane orientation, i.e., NMF(101) domain. (b) RSM around $(262)_\circ$ plane of NMF with (010) out-of-plane orientation, i.e., NMF(101) domain. (c) RSM around $(260)_\circ$ and $(062)_\circ$ reflections of NMF(010) domain. (d) RSM around $(040)/(202)_\circ$ plane of NMF, i.e., along the q_z (out-of-plane orientation).

Table 4.2: Lattice parameters obtained from figure 4.13 (a) and figure 4.17

	NMF(101) domain (Å)	NMF(010) domain (Å)	Bulk (Å)
a	5.86 ± 0.02	5.76 ± 0.05	5.757
b	8.04 ± 0.01	7.980 ± 0.001	8.008
c	5.45 ± 0.01	5.57 ± 0.04	5.548

is different for NMF(010) and NMF(101) domains. For example, $(222)_o$ plane of NMF(010) domain the χ angle is 26.50° whereas for NMF(101) domain it's 63.50°. Please refer figure to 4.15 (b) for illustration. This implies probing same plane of different NMF domains requires different tilts of sample stage before the ϕ, off-axis $\theta - 2\theta$ and RSM scans. This allowed for the unique identification of (010) and (101) domains using in-plane scans. Please refer to table 4.2 for the appropriate χ and 2θ angles of planes for different NMF domains on STO(001) that were used for ϕ, off-axis $\theta - 2\theta$ and RSM scans.

Figure 4.14 shows the ϕ-scans of the $(222)_o$ reflection of the NMF(101) and NMF(010) domains along with (012) reflections of the substrate. In both NMF domains, four peaks separated by 90° were observed, meaning that two NMF phases with orthogonal b_o axes were present. For NMF(010) domains, the orthorhombic a_o and c_o axes $\parallel$ STO [110]. For NMF(101) domains, the b_o axis commensurately aligns $\parallel$ STO [010] and $[\bar{1}00]$ (labeled D_1 and D_2 in figure 4.15 b, top view). This indicated the NMF(010) and NMF(101) domains grew on STO square lattices corresponding to $a\sqrt{2} \times a\sqrt{2}$ and $2a \times 2a$ respectively ($a = 3.905$ Å) as shown in figure 4.15. Similar epitaxies of orthorhombically distorted perovskite oxide films on STO have been

reported elsewhere [107–110]. For the NMF(010) domains, each $(222)_o$ reflection was additionally comprised of two peaks separated by 1.4° (figure 4.14 middle panel inset). Therefore, each NMF(010) domain was actually comprised of two in-plane twin domains rotated by 1.4° about the surface normal with respect to each other (labeled D_3 and D_4 in figure 4.14 (a) middle panel inset and 4.15 (a) top view).

Figure 4.16 shows the reciprocal space maps (RSMs) of the different NMF domains. Figure 4.16 (a) shows the reflection around the $(323)_o$ plane for b_o in-plane, i.e., NMF(101) domain, along with the (103) reflection from the substrate. Similarly, figure 4.16 (b) shows the reflection around $(262)_o$ plane for b_o out-of-plane, i.e., NMF(010) domain, along with (203) reflection from the substrate. Furthermore, the presence of $(260)_o$ and $(062)_o$ reflections, as seen in figure 4.16 (c) for NMF(010) domain show a difference in a_o and c_o lattice parameters confirming the orthorhombic nature in NMF(010) domain. In addition, reflection of $(240)_o$ and $(042)_o$ planes at $56.04 \pm 0.05°$ and $56.74 \pm 0.05°$ respectively (figure 4.17 (d)) in NMF(010) domain further solidifies the claim. The reflection of $(240)_o$ and $(042)_o$ planes at $55.66 \pm 0.02°$ and $56.95 \pm 0.01°$ respectively (figure 4.17 (b)) of NMF(101) domain shows the absence of $a_o = c_o$ distortion in the NMF(101) domain. Therefore, both NMF(010) and NMF(101) domains are orthorhombic. Figure 4.16 (d) shows the out-of-plane RSM near the STO (002) reflection.

Lattice parameters for each domain were obtained from the out-of-plane $\theta - 2\theta$ scan of the $(040)_o/(202)_o$ reflection (figure 4.13 (a)) and in-plane $\theta - 2\theta$ scans of $(042)_o$ and $(222)_o$ reflections for corresponding domains in figure 4.17. See table 4.2 for computed lattice parameters. For NMF(101) domain, the lattice parameters a_o

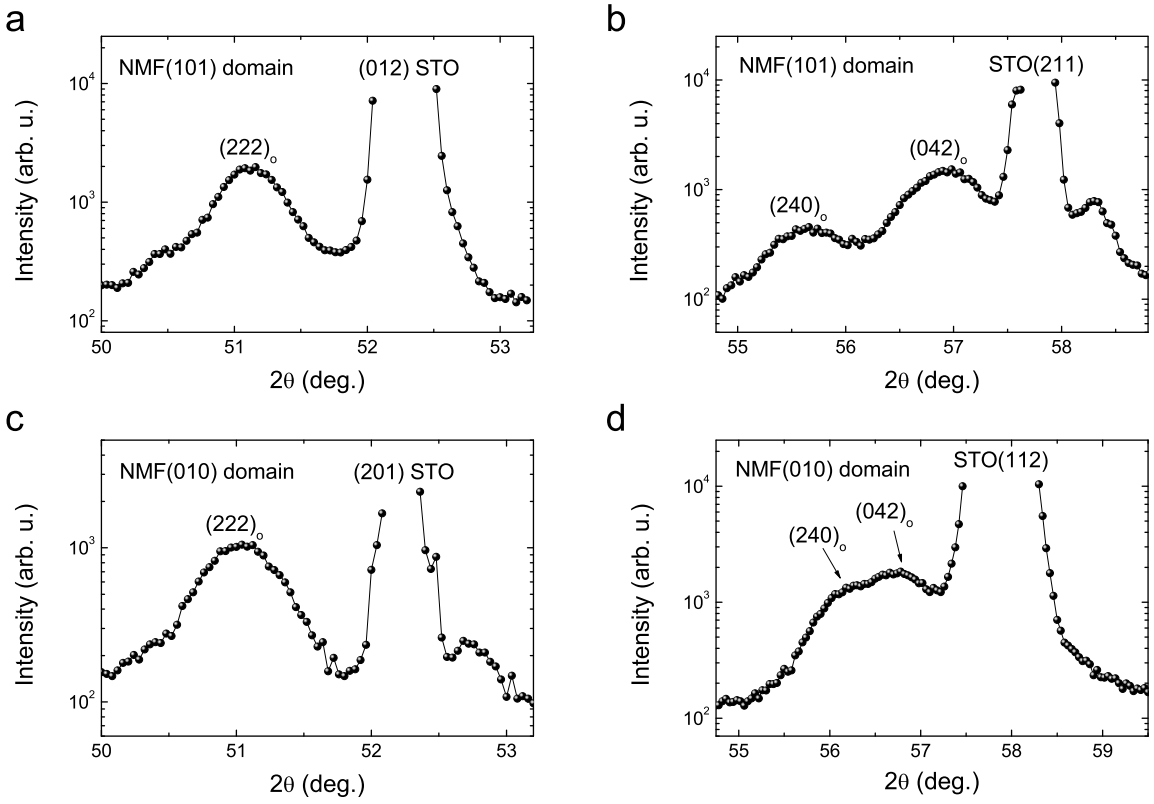

Figure 4.17: Off-axis $\theta - 2\theta$ scan of NMF on STO: (a) $\theta - 2\theta$ scan around $(222)_\circ$ peak of NMF(101) domain with $\chi = 63.50°$. (b) $\theta - 2\theta$ scan around $(042)_\circ$ peak of NMF(101) domain with $\chi = 65.09°$. (c) $\theta - 2\theta$ scan around $(222)_\circ$ peak of NMF(010) domain with $\chi = 26.50°$. (d) $\theta - 2\theta$ scan around $(042)_\circ$ peak of NMF(010) domain with $\chi = 35.82°$.

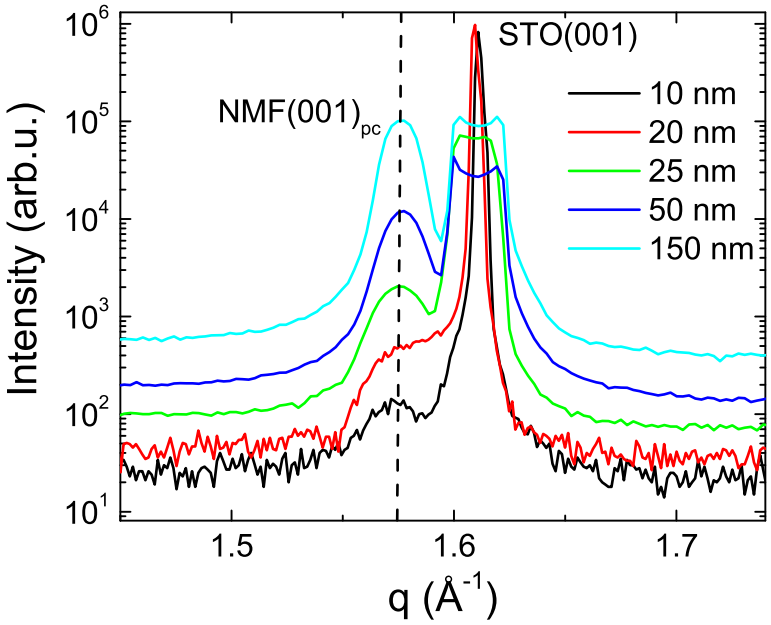

Figure 4.18: XRD graphs of NMF films with different thicknesses.

and $c_\circ$ had the same $\approx 2\%$ strain but with opposite sign; that is, $a_\circ$ had a tensile strain whereas $c_\circ$ had a compressive strain, while $b_\circ$ remained relaxed. It should be noted that the measured unit cell volume of 257 ± 2 Å^3 agrees with that of the bulk material (255.65 Å^3). For NMF(010) domain, all the lattice parameters were relaxed with a unit cell volume of 255 ± 2 Å^3. In table 4.2 we also compare results from $b_\circ$ in-plane and the bulk lattice parameters from the literature (Ref. [10]). It appears that the $b_\circ$ in-plane domains are even more orthorhombic than the out-of-plane domains.

A series of films with different thicknesses were grown on STO(001) to investigate the thickness dependent strain (figure 4.18). All the films were grown on the same $T_s = 250$ °C. The out-of-plane lattice parameters for 10, 20, 25, 50 and 150 nm films were found to be 3.954 Å, 3.976 Å, 3.980 Å, 3.982 Å and 3.988 Å respectively.

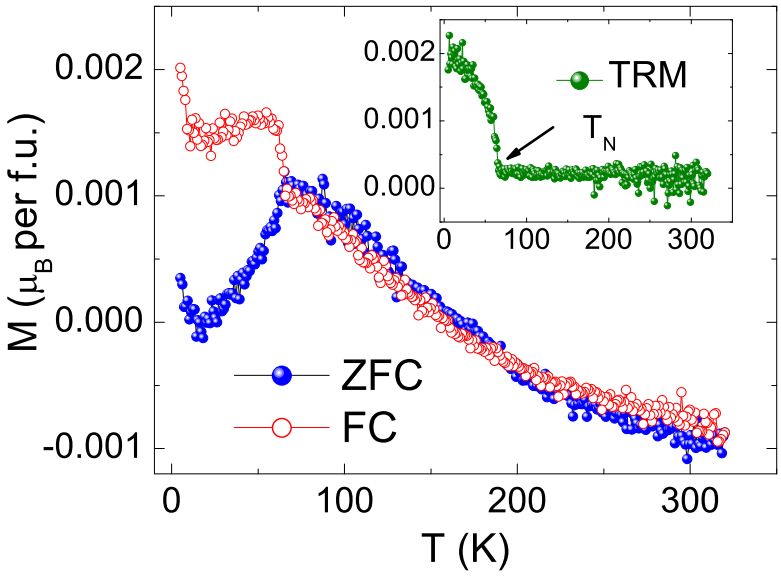

Figure 4.19: Magnetic behavior of a 50 nm NMF/STO thin film: FC and ZFC. Inset shows TRM data. The negative FC and ZFC background is likely a result of an imperfect subtraction of the substrate signal.

This indicates all the films experience compressive strain of 1% or less. However, films above 20 nm are almost fully relaxed because in an ideal situation NMF film (pseudocubic lattice parameter $a_{pc} = 3.995$ Å) would have 2.3% compressive strain when it is grown on STO ($a_{STO} = 3.905$ Å).

4.4.2 Magnetic Characterization

The magnetic properties of 50 nm NMF films grown at $T_s = 250 - 300$ °C were measured. The temperature-dependent magnetization measurements on NMF/STO were carried out by first cooling the samples from room temperature to 5 K in $H = 0$, and then measuring the magnetic moment m as a function of T in $H = 1$ kOe applied in-plane along the STO [001] direction while warming up to 320 K (zero-field cooled,

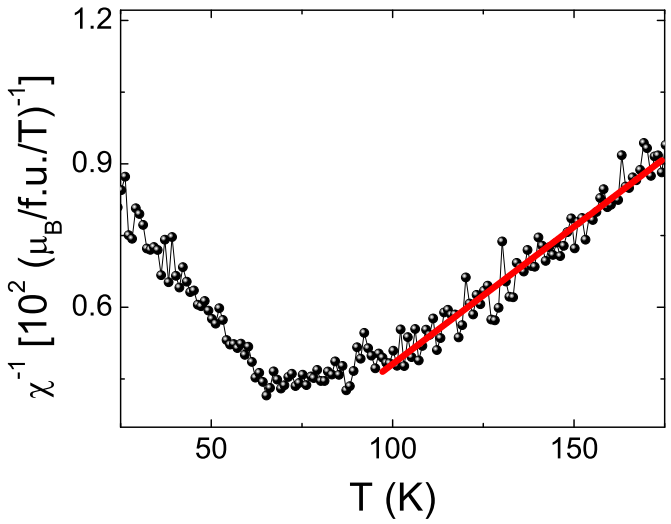

Figure 4.20: Inverse magnetic susceptibility χ^{-1} vs. T of NMF/STO sample. The straight red line is the Curie-Weiss fit for the ZFC data above the Neel temperature of the sample.

ZFC). Then the measurements were continued while cooling in the same H down to 5 K (field cooled, FC). Subsequently, the thermoremanent magnetization (TRM) was measured while warming in $H = 0$. All magnetization data were corrected for the substrate magnetic response, measured separately under identical conditions, and normalized to the film volume. ZFC and FC data in figure 4.19 (a) show a Curie-Weiss-like increase with decreasing temperature until the ZFC data peak at $T_N \approx 66$ K. On the other hand, the FC m decreases sharply below $T_N \approx 66$ K, in good agreement with theory [11] and previous experimental work [100–104]. This split between ZFC and FC magnetizations below 66 K is consistent with weak FM below T_N, in agreement with previous studies of NMF nanoparticles and nanoplates [104,105]. The upturn in the ZFC and FC curves (figure 4.19) at low temperatures ($<$ 20 K) is most likely due to the impurities in the substrate and imperfect background

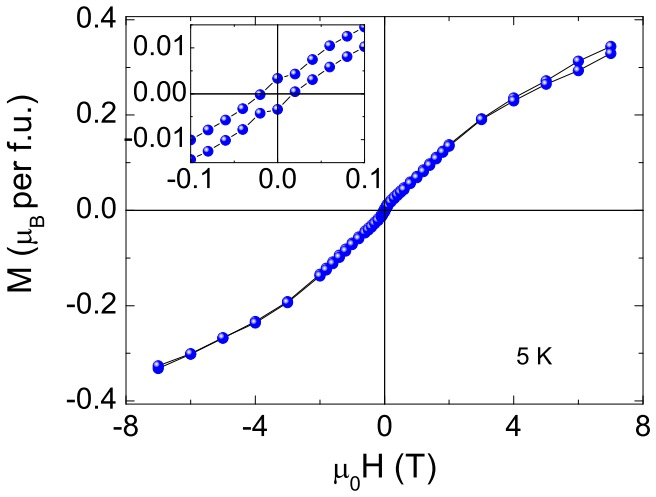

Figure 4.21: Magnetic behavior of a 50 nm NMF/STO thin film: In-plane magnetization M as a function of the applied magnetic field $\mu_0 H$ at 5 K. Inset shows close-up view of the low-field region.

subtraction. A second transition previously reported in bulk NMF at $T \approx 145$ K was not observed [102]. Because bulk MnF_2 has collinear antiferromagnet order below $T_N \approx 67$ K [111], and no indication of the MnF_2 crystalline order was found in the XRD scans, we can exclude this possibility. The inverse magnetic susceptibility vs. T for ZFC data is plotted on figure 4.20. The diamagnetic background from the substrate was subtracted, and a small offset of 4×10^{-7} emu was added to m to make data positive before taking m inverse. The straight red line is the best fit obtained using Curie-Weiss law [$\chi = C/(T - \theta)$] above T_N which yielded Curie constant C and θ to be 1.63 $[\mu_B/(\text{f.u.}\cdot\text{T}\cdot\text{K})]^{-1}$ and 18 ± 3 [K] respectively with coefficients of determination, $R^2 = 0.95$. This result is thus indicative of the Curie-Wiess behavior of NMF film above the Néel temperature. After FC (high to low temperature in field) measurement, the spins within the Mn octahedra have non-zero net magnetization due to canting of the spins below the T_N (see figure 2.4 for illustration). Once the

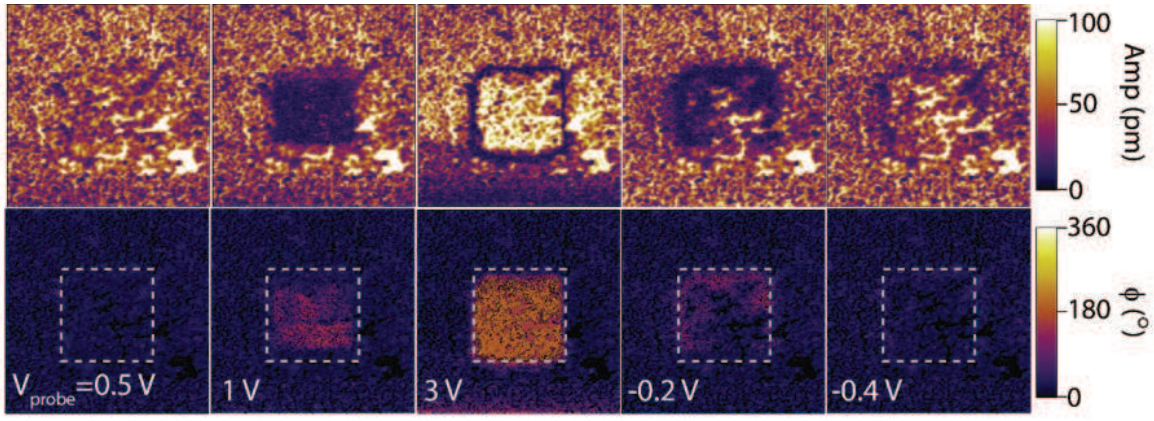

Figure 4.22: Ferroelectric switching by biased scanning probe PFM amplitude (top) and phase (bottom) images of a 3 μm $\times$ 3 μm area consecutively taken after scanning over the center 1.5 μm square (marked with dashed line) with different probe biases [112].

temperature is above the T_N, the spontaneous weak ferromagnetic order is destroyed by the thermal energy. Therefore, the TRM data have a Brillouin-like increase below T_N (figure 4.19 inset), confirming the weak ferromagnetic nature of the transition in NMF film. Figure 4.21 shows the in-plane magnetization hysteresis loop $M(H)$ measured at 5 K with the diamagnetic response from the substrate subtracted. The $M(H)$ behavior is consistent with weak FM, including an S-shaped loop with a lack of saturation in magnetic fields of up to 7 T and a remanent magnetization $M(H = 0) \approx 0.003\ \mu_B$/f.u. in the low field region (figure 4.21 inset).

4.4.3 Electrical Characterization

Piezo-response Force Microscopy (PFM)

To investigate the ferroelectric properties of 50 nm NMF/STO film, our collaborator Cheng Cen and Ming Yang (WVU) conducted local switching measurements

with biased scanning probe using PFM (figure 4.22).

A series of contact mode images were taken in the same 1.5 μm $\times$ 1.5 μm area of the film. With general DC probe (V_{probe}) sequence 0 V $\rightarrow$ 10 V $\rightarrow$ -10 V $\rightarrow$ 0 V was applied on each scans. PFM was measured at $V_{probe} = 0$ after each bias scan to investigate the persistent polarization in the region. A clear 180° rotation of the phase was observed after bias scan ramp up (0 V to 10 V) and ramp down (10 V to -10 V) indicating ferroelectric (FE) switching behavior in the film.

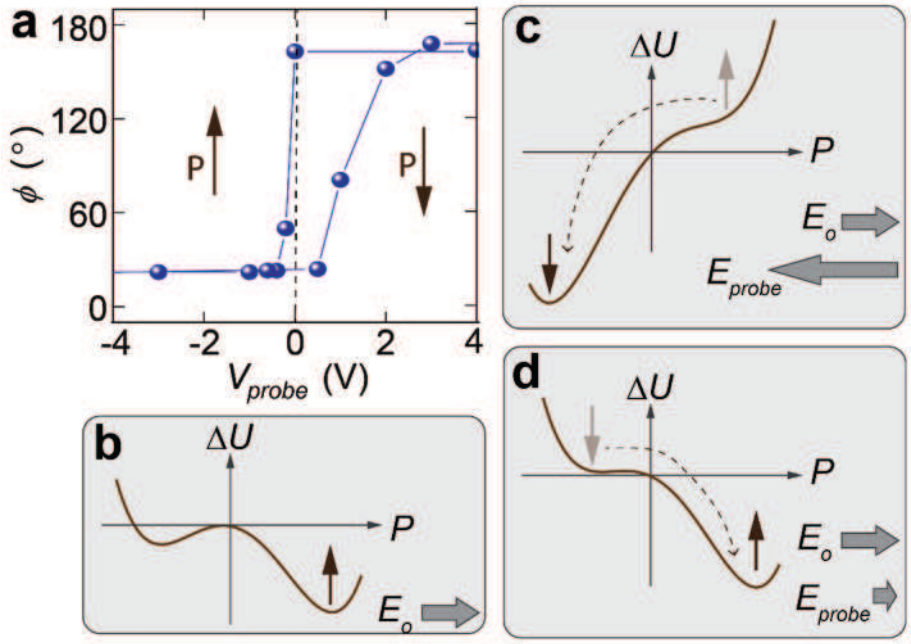

Figure 4.23: Asymmetry in ferroelectric hysteresis loop induced by built-in field (a) Hysteresis of PFM phase as a function of poling probe voltage. (b-d) Illustrations of the ferroelectric double well potential and polarization states affected by the built-in field (E_o) and external probe fields [112].

PFM phase (obtained by averaging the phase of each pixel of the image in the biased region) as a function of bias V_{probe} gives a hysteresis curve (figure 4.23 (a)). Interestingly, the hysteresis loop has an asymmetric shape suggesting the presence of

preferred polarization on the film. The positive bias voltage of 3 V almost completely reversed the polarization, however, a negative bias voltage as small as -0.2 V reverses back the polarization. This suggests that the film has a preferred up (out-of-plane) polarization. FE switching in the thin films is very sensitive to the boundary condition at the film surface and the interface with the substrate [113–118]. The built-in field in our film could be due to many factors such as band bending due to surface charge and charged states created by defects.

A ferroelectric material shows double well potential as ground state energy [40]. But the presence of built-in field (E_o) could create a shallow well on one side of the curve as shown in figure 4.23 (b) which causes the presence of thermodynamically preferred polarization. A larger field is required opposite to the built-in field to reverse the preferred polarization in the film (figure 4.23 (c)). However, a small field is enough to switch back the polarization to its original state due to the assistance by the built-in field as shown in the figure 4.23 (d). The hysteresis loop measured in NMF film shows that it is shifted horizontally to the positive biased side with E_o very close to the coercive field. Such a small coercive field on the positive biased side means the down polarization obtained by positive bias can thermodynamically flip back to it preferred up polarization. It was found that down polarization typically flips back within approximately 30 min in air.

To further investigate the FE behavior of the film, two 200 μm $\times$ 200 μm Ti/Au electrodes with 40 μm gap were deposited on top of the film surface by photolithography (figure 4.24). It was found that the application of in-plane electric field can revert the down polarization faster than unperturbed gradual reversion. Figure 4.9 (a) (left)

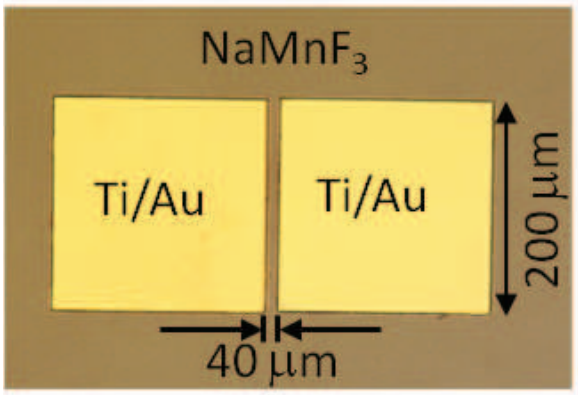

Figure 4.24: Microscope image of two 200 μm $\times$ 200 μm Ti/Au electrodes with 40 μm gap to apply in-plane electric field for PFM measurement.

shows the PFM images taken immediately taken after poling the center square by 10 V tip bias. The imaging region was in the middle of the gap between the Ti/Au electrodes. The polarization reverses back to its preferred up polarization after the application of 200 V (5×10^6 V/m) for 30 seconds (please see figure 4.25, right images). The reversal of the polarization was slower with smaller field. An in-plane field of 50 V took 120 seconds for it to flip the polarization (figure 4.25 (b)). The observed polarization reversal was confirmed to be independent of the direction of the in-plane electric field. It has been previously shown that it is possible to switch the polarization with biased in-plane field applied *via* surface electrode if the polarization has in-plane component [119–121].

According to the computational work, the ferroelectric polarization points along the long axis b in NMF with lattice parameter $a = c$. The structural characterizations of NMF have shown the presence of two different domains in the same film- one domain with long axis in-plane [NMF$(101)_o$] and other with long axis out-of-plane [NMF$(010)_o$], but both of these domains are orthorhombic. NMF$(101)_o$ domain was

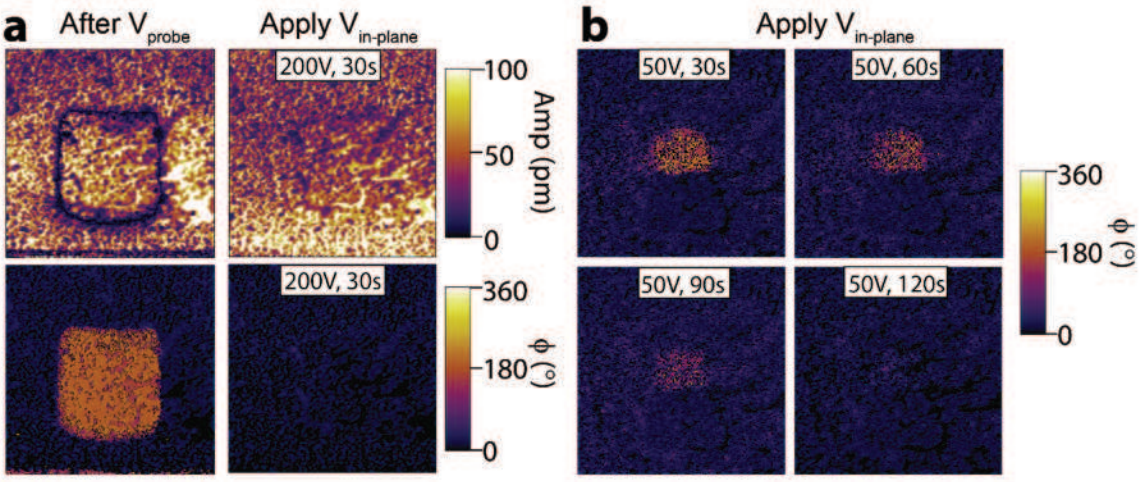

Figure 4.25: Restoration of up polarization by in-plane field. (a) PFM amplitude (top) and phase (bottom) measured right after the biased probe poling (left) and after the application of 200 V across the two surface contacts for a duration of 30 s (right). (b) PFM phase measured following applications of 30 s 50 V bias between the surface electrodes, showing the graduate reversion of the center 500 nm probe poled down-polarized region [112].

found to be more orthorhombic than the bulk NMF. However, in NMF$(010)_o$ domains, the lattice parameters a and c are strained such that their ratio $a/c \approx 1.035$, suggesting there might be regions where their ratio is closer to one. In these regions, ferroelectricity develops with or without strain as NMF undergoes structural transform from non-polar $Pnma$ to the polar $Pna2_1$ phase. Interfacial effects, grain boundaries or the presence of defects can contribute to compressive strain; in such a case ferroelectricity becomes more robust.

It should also be noted that the slightest variation of the rate during the growth of NMF gives rise to unidentified impurities in NMF film. Impurities peaks can be observed by XRD scans and usually have small intensity. However, they have a profound effect on magnetization data (especially ZFC-FC curves) and ferroelectricity.

Samples with impurities peaks show additional features in the ZFC-FC curves such as ZFC-FC splitting at a higher temperature ($T > T_N$). Also, there was the absence of ferroelectricity in these samples.

Same thickness (50 nm) NMF films were also grown on different substrates: $LaAlO_3$, $(LaAlO_3)_{0.3}(Sr_2TaAlO_6)_{0.7}$ (LSAT), and $KTaO_3$ in order to study the strain effect on ferroelectricity. However, out of a total of fourteen samples characterized by PFM, only three films that were directly grown on STO showed ferroelectric behavior. Films grown on other substrates did not show ferroelectric switching.

Chapter 5

Exhange Bias and Short Range Polar Order in $NaMnF_3$ grown on $SrRuO_3$ Bottom Layer

5.1 Introduction

The group of perovskite materials shows a wide range of technologically important phenomena, including ferroelectricity, ferromagnetism, multiferroicity and superconductivity. One of the ways to utilize these materials in device applications is to make heterostructures. It is possible to fabricate heterostructures due to strutural and chemical similarities between the materials (film and substrate) along with advances in thin film growth techniques. In addition to device applications, heterostructures also enable the study of fundamental issues such as interfacial interaction and artificial multifunctional electronic properties [122, 123]. Here the discussion

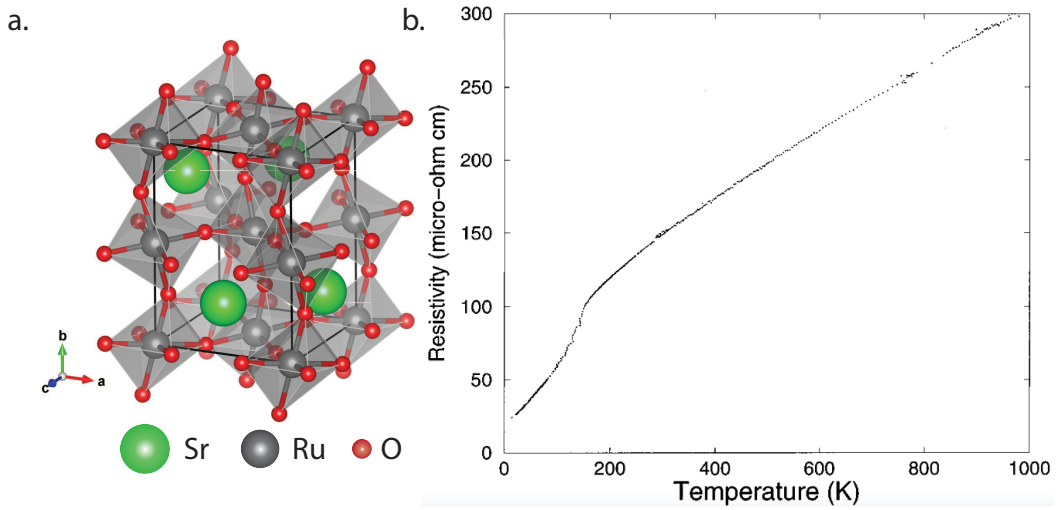

Figure 5.1: a) Schematic representation of perovskite structure of $SrRuO_3$. b) Resistivity as a function of temperature of $SrRuO_3$ (taken from Ref. [124]).

on the growth, structural, magnetic and dielectric properties of NMF film deposited on $SrRuO_3$/STO(001) is presented.

$SrRuO_3$ belongs to an interesting class of ruthenates (e.g., $CaRuO_3$ and Sr_2RuO_4). Similar to most of the perovskites, $SrRuO_3$ has an orthorhombic crystal structure at room temperature with a $GdFeO_3$ structure [125]. $SrRuO_3$ belongs to *Pnma* space group with lattice parameters: $a = 5.5670$ Å, $b = 7.8446$ Å, and $c = 5.5304$ Å [125]. The pseudo-cubic lattice parameter is 3.93 Å with a lattice mismatch of about 0.64% with STO(001) substrate. $SrRuO_3$ is a useful electrode for microelectronics because it is chemically stable with metallic behavior at room temperature [52, 124]. It is also known to go through a ferromagnetic transition with a Curie temperature $T_C \approx 160$ K [126]. $SrRuO_3$ has been successfully grown in thin film form using 90° magnetron sputtering [127], MBE [128], and PLD [52, 53]. The commonly reported substrate temperatures and oxygen partial pressures range from $600 - 700$ °C and

$1 - 300$ mTorr of O_2 respectively [129]. There are several advantages of epitaxial $SrRuO_3$ conducting bottom layer: (a) it allows for the application of an out-of-plane electric field, (b) it can strain NMF film because of the lattice mismatch (strain is necessary for NMF to be ferroelectric), and (c) it shows good conductivity on variety of conditions unlike Nb-doped STO which shows unusual conductivity [130, 131].

$SrRuO_3$ was grown using a PLD system manufactured by Neocera LLC. The growth was monitored *in-situ* using RHEED. The sample was then transferred to MBE chamber for the growth of NMF. After the NMF growth, the film quality was monitored using *in-situ* RHEED. The film was further characterized by *ex-situ* AFM, XRD and SQUID magnetometry. Exchange-bias was also measured using SQUID magnetometry. Ferroelectric and dielectric measurements were undertaken to investigate the dielectric properties of the film. The dielectric constant was measured using a lock-in amplifier in the frequency range of 100 Hz to 100 kHz from 10 K to room temperature using a cryostat and an ac voltage amplitude of $V_{ac} = 100$ mV. Similar results were obtained for $V_{ac} = 10$ mV.

5.2 Experimental Procedures

5.2.1 Growth

$SrRuO_3$

Before the growth of $SrRuO_3$ (SRO), STO(001) single crystal substrates obtained from MTI Corporation were ultrasonically clean in acetone and IPA. Single TiO_2 terminated substrates were then prepared by two thermal annealing and DI water

leaching process as described in section 4.1.1. The substrates were then loaded into the PLD chamber for the growth of SRO.

The SRO film was grown at 600 °C in 100 mTorr of O_2 partial pressure. The frequency and energy of the laser were set to 5 Hz and 320 mJ respectively during the growth. The growth was monitored by RHEED. After the SRO growth, the temperature was slowly dropped to room temperature at 5 °C per minute at the same 100 mTorr of O_2 partial pressure.

NMF

Immediately after the growth of SRO, the sample was transferred to ultra-high vacuum MBE chamber for the growth of NMF. The substrate temperature was kept at 250 °C during the growth. The rate of NaF and MnF_2 was maintained at ~ 0.050 Å/s and ~ 0.035 Å/s with 750.8 °C and 770.0 °C K-cell temperatures, respectively.

5.3 Results and Discussion

5.3.1 Structural Characterization

Figure 5.2 (top) shows the RHEED image of STO before growth. The bottom left image shows the RHEED image at 250 seconds into the growth and bottom right image shows the RHEED image after the growth of SRO. The streaky-spotty RHEED image after the growth means the SRO film is crystalline but little rough. From the RHEED oscillations and XRD finite size oscillations (figure 5.4), the SRO thickness was calculated to be 30 nm. Figure 5.3 shows the RHEED image after the growth

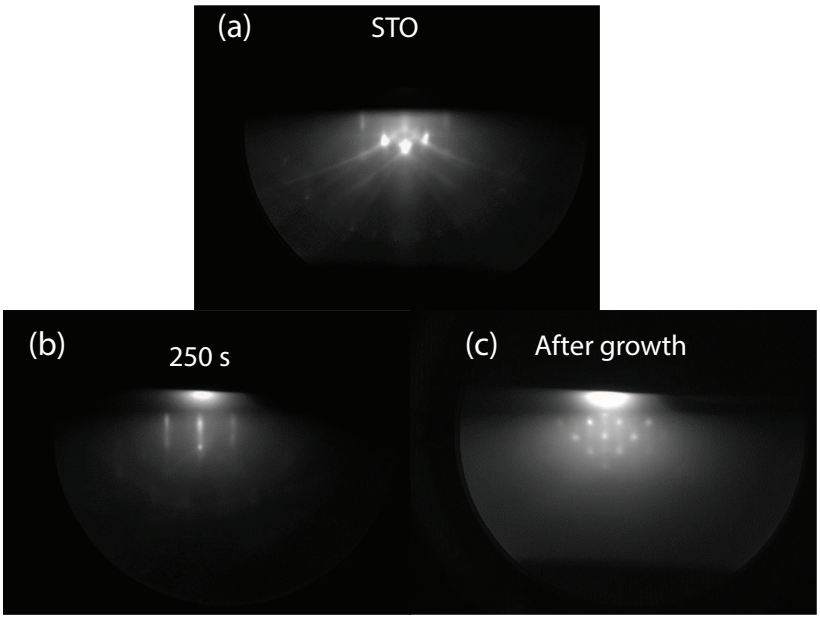

Figure 5.2: RHEED images during and after the growth of $SrRuO_3$: (a) RHEED of STO before the $SrRuO_3$ growth, (b) RHEED image during the growth (at 250 seconds) and (c) RHEED image after the growth.

of 150 nm of NMF film on top of SRO. The streaky pattern with somewhat fuzzy background suggests that the film is crystalline with some defects.

Figure 5.4 shows $\theta - 2\theta$ XRD scan of 150 nm of NMF on SRO (NMF/SRO). First and second order peaks for SRO are observed at 21.99° and 44.84° and for NMF at 22.32° and 45.35° respectively. The positions of the SRO peaks were consistent with the data in the literature [107]. Finite size oscillations from SRO can also be observed on either side of the SRO peaks which indicates the high quality of SRO film. The out-of-plane lattice parameters were computed to be 3.989 Å and 3.982 Å for SRO and NMF respectively.

Rocking curve measurements were also performed around the SRO and NMF $(001)_{pc}$ peaks (figure 5.5). The FWHMs were found to be 0.16° and 1.85°, respectively,

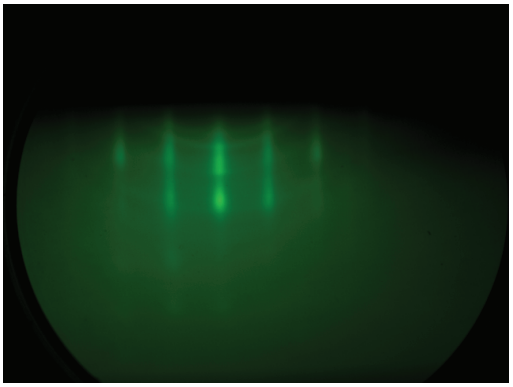

Figure 5.3: RHEED image after the growth of 150 nm of NMF on top of SRO.

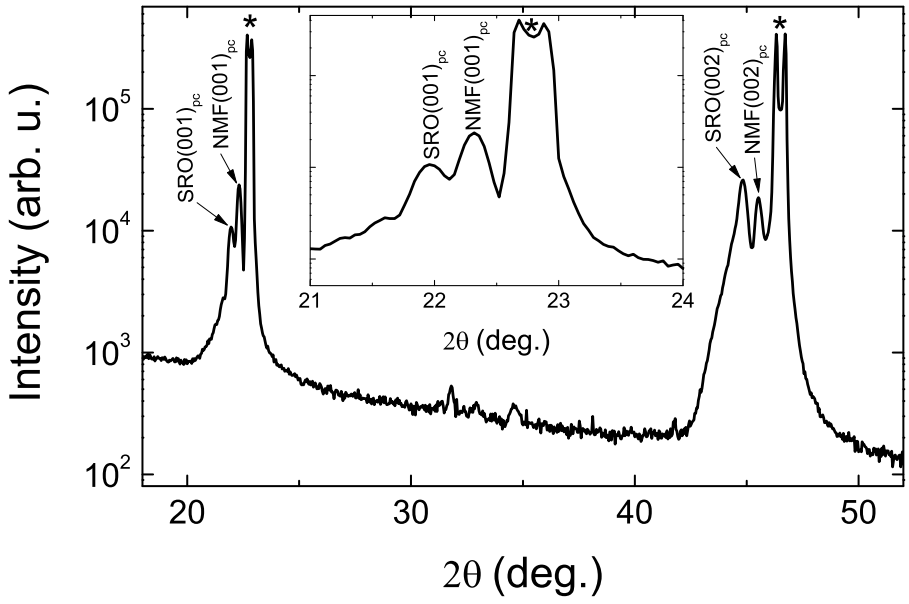

Figure 5.4: $\theta-2\theta$ XRD scan scan of NMF/SRO film. The asterisks mark the substrate peaks. Double peak in the substrate is due to intensity saturation in the detector.

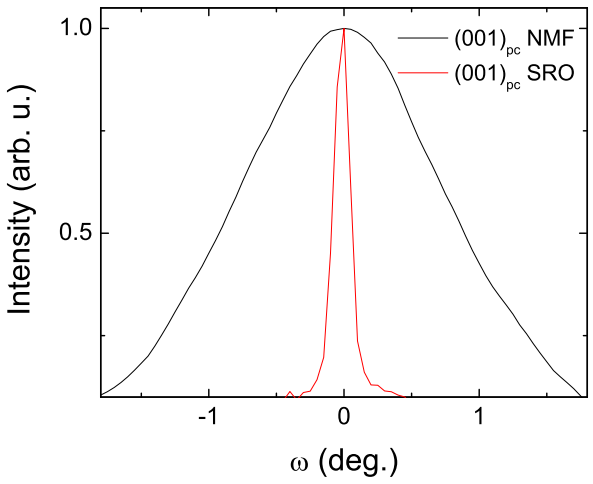

Figure 5.5: Rocking curve of the $(001)_{pc}$ peak of SRO and NMF.

with the Lorentzian fit. The wide rocking curve peak observed in NMF indicates that the mosaic spread larger than the one observed in 50 nm NMF on STO (NMF/STO) (FWHM = 1.32°) most likely due to introduction of the bottom SRO layer. Figure 5.6 shows the 2 μm × 2 μm AFM topography image of the film. The image shows randomly shaped small (tens of nm) grain-like structures forming the surface. The rms roughness of the image area was approximately 4 nm.

For the NMF/SRO sample, epitaxy could not be confirmed by ϕ, off-axis $\theta - 2\theta$ scans or RSM, despite the streaky RHEED pattern in figure 5.3. This indicates that the bulk of NMF was highly disordered, with small domains. Because of the similarity between STO and SRO, however, it is reasonable to assume that the strain in the NMF/SRO sample was not too different from the NMF/STO.

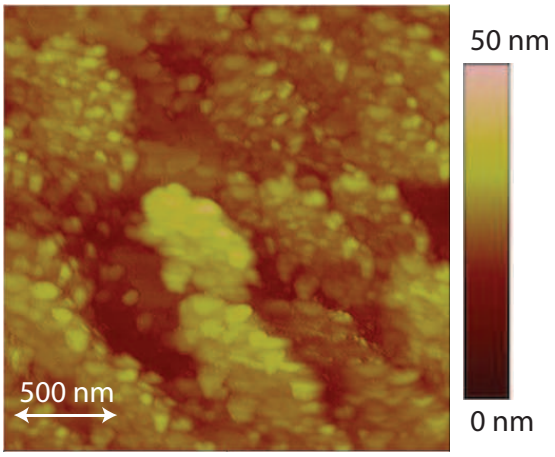

Figure 5.6: 2 μm $\times$ 2 μm AFM topography image of NMF/SRO.

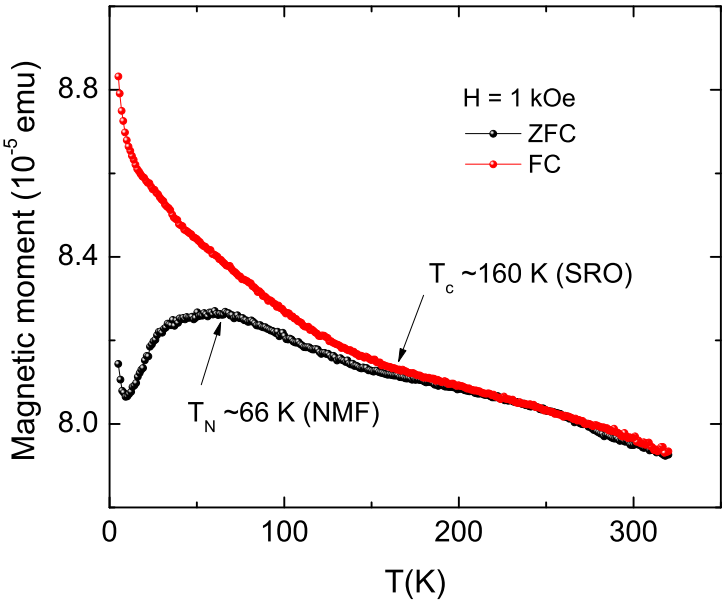

Figure 5.7: Magnetic response of NMF/SRO thin film: ZFC and FC. Both the ferromagnetic transition of SRO and antiferromagnetic transition of NMF are labeled.

5.3.2 Magnetic Characterization

The temperature-dependent magnetization measurements on NMF/SRO were carried out by first cooling the samples from room temperature to 5 K in $H = 0$, and then measuring the magnetic moment m as a function of temperature T in $H = 1$ kOe applied in-plane along the STO [001] direction while warming up to 320 K (zero-field cooled, ZFC). Then the measurements were continued while cooling in the same H down to 5 K (field cooled, FC).

Figure 5.7 shows the ZFC and FC magnetic moment curves. The splitting of ZFC and FC at around 160 K corresponds to the T_C of SRO and is in good agreement with the literature [126]. This divergence in ZFC and FC curves gradually increases with decerasing temperature even though the overall magnetic moment of the system increases. However, a cusp in the ZFC curve is observed around the Néel temperature ($\sim$ 66 K) of NMF. This indicates the existence of a distribution of transition temperatures which is likely due to presence of small particles, domains and/or domains walls in the system. In other words, there is a high level of disorder (randomness in the exchange interactions-long range order) in the system which is also supported by the dielectric measurements (discussed in the section 5.3.3). Interestingly, the ZFC and FC data look are qualitatively similar to blocking process-type behavior observed in antiferromagnetic materials γ-Fe_2O_3 at 72 K [132] and $BiFeO_3$/SRO at 30 K [133].

Exchange bias in the NMF/SRO heterostructure was measured after field cooling the sample in 30 kOe. Figure 5.8 shows the magnetic field dependence magnetic moment measurements carried between 5 K and 55 K ($T < T_N$ of NMF). The data

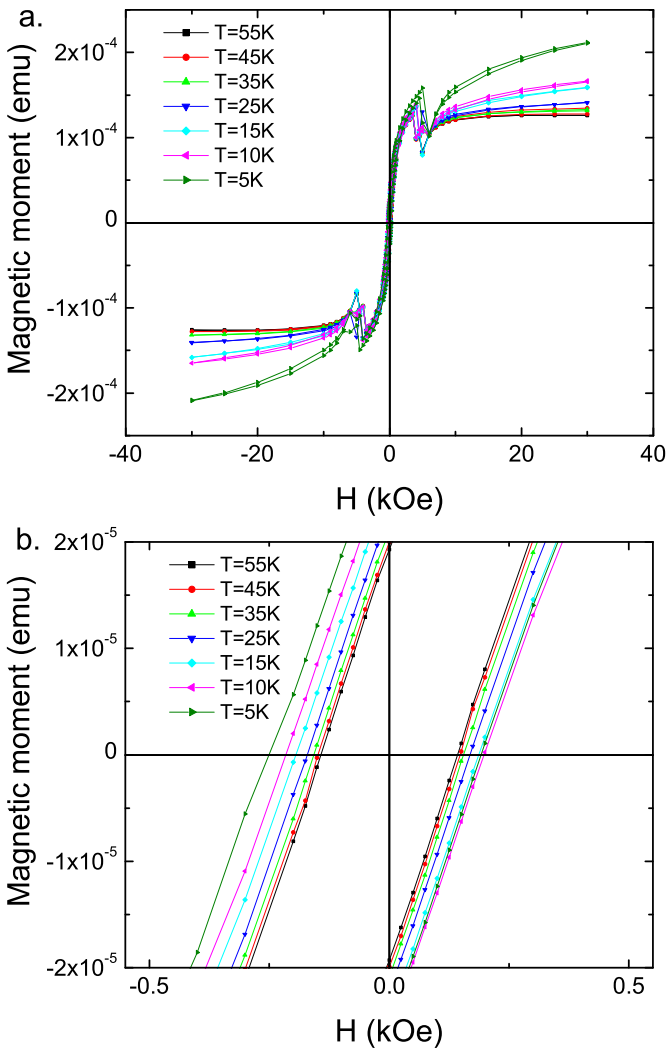

Figure 5.8: (a) Exchange bias hysteresis loops of NMF/SRO heterostructure at different temperatures after field cooling. The jumps of the magnetic moment in the loops are due the crossings through $H = 0$. (b) Low field zoom of (a).

in figure 5.8 are plotted after the subtraction of the linear background from the substrate. The coercive field as a function of temperature can be satisfactorily fitted by exponential equation $H = H_0 + Ae^{(R_0 \cdot T)}$ (figure 5.9 (a) red curve) which yields negative R_0 indicating exponential decay of the field with the increase of temperature. The fit yields $H_0 = 131 \pm 2$ Oe, $A = 114 \pm 1$ Oe and $R_0 = -0.042 \pm 0.002$ with

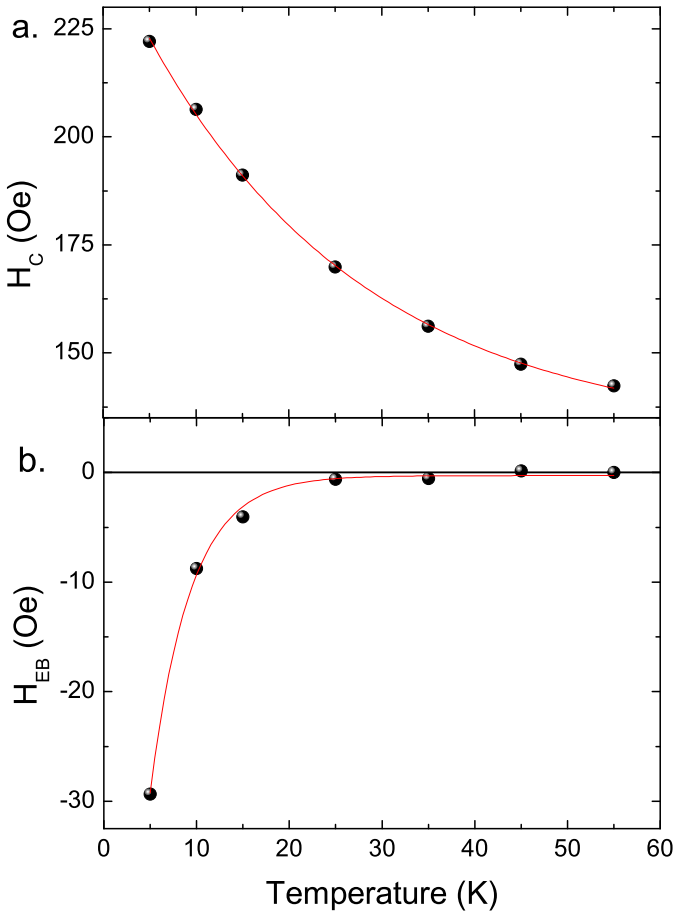

Figure 5.9: Coercive field (a) and exchange bias field (b) as a function of temperature. Black dots are the data points and red curves are the fits.

coefficient of determination $R^2 = 0.9993$. It was found that the system has negative exchange bias due to the shift of hysteresis loops along the negative magnetic field axis (figures 5.8 (b) and 5.9 (b)) with blocking temperature (T_B) close to 45 K. The exchange bias field as a function of temperature can be satisfactorily fitted by exponential equation $H = Ae^{(R_0 \cdot T)}$ (figure 5.9 (b) red curve). The fit yields $A = -90 \pm 5$ Oe and $R_0 = -0.23 \pm 0.01$ with coefficient of determination $R^2 = 0.9968$.

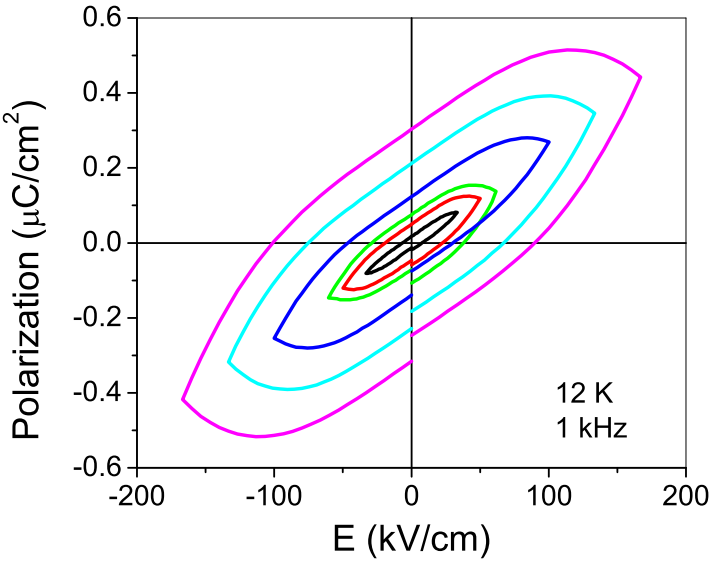

Figure 5.10: $P-E$ hysteresis loops of NMF/SRO film.

5.3.3 Electrical Characterization

Ferroelectric Testing

Polarization as a function of the electric field ($P-E$) was measured on the film with bottom conducting SRO layer. Ti/Au contacts of 250 μm square deposited on film were used as top electrodes. The contacts were deposited using a e-beam evaporation with help of a shadow mask. Figure 5.10 shows the hysteresis loops up to 160 kV/cm measured at 12 K at a frequency of 1 kHz. It also found that the shape of loop was dependent on the frequency of applied field, and for field greater than 200 kV/cm, there was resistive leakage from the sample indicated by football-shaped loops (not shown) [63]. Moreover, NMF/SRO $P-E$ loops lacked some of the charateristics that are expected in a ferroelectric hysteresis loop. The loops were not saturated and they also did not show a prominant concave region in the loops; these

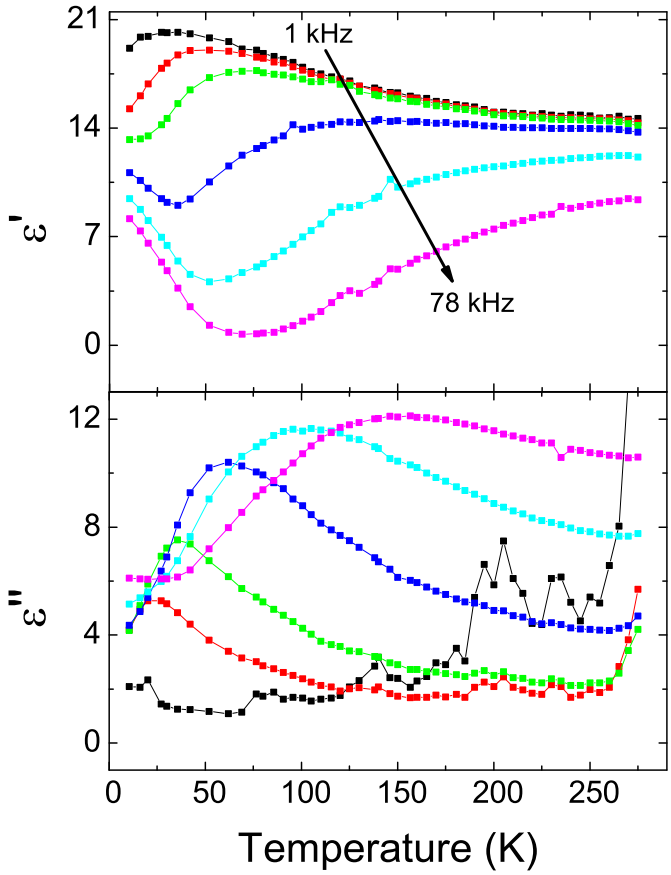

Figure 5.11: Real (top panel) and imaginary (bottom panel) parts of ε as a function of temperature at different frequency, f = 1, 5, 10, 25, 50 and 78 kHz. The arrow in top panel points to the direction of increasing f.

loops cannot be interpreted as ferroelectric loops [15] without further analysis such as dielectric measurements as a function of temperature.

Dielectric Properties

Dielectric measurements of 150 nm thick NMF/SRO were carried out in the frequency range of 100 Hz to 100 kHz from 10 K to room temperature. Figure 5.11 shows the dielectric permittivity [$\varepsilon(\omega) = \varepsilon'$ - iε''] as a function of temperature for NMF/SRO

film at frequencies from 1 to 78 kHz. The response at 0.1 kHz almost overlaps with that at 1 kHz, so it is not shown. At large frequencies, the increase of the real part of the dielectric permittivity $\varepsilon'(T)$ at low T is superimposed with a broad maximum whose position shifts to lower T with decreasing frequency f. The imaginary part of the dielectric permittivity, $\varepsilon''(T)$, also shows a peak that shifts to lower T and becomes narrower with decreasing f. This behavior implies a strong relaxation of the dielectric permittivity and resembles properties of relaxor ferroelectrics, [**?**] but the frequency dependence of the position of the maximum of $\varepsilon'(T)$, T_m, is much stronger than is typically observed in relaxors [134]. In our case, T_m shifts more than 200 K in only two frequency decades.

To gain more insight in relaxation dynamics, we analyzed frequency dependence of ε (see figure 5.12. At low frequency, $\varepsilon''(f)$ follows a $1/f$ dependence which is due to a non-zero dc conductivity (figure 5.12 bottom panel). Also, a typical relaxation maximum is observed for $f > 3$ kHz, whose position shifts to lower frequency as temperature decreases. The $\varepsilon'(f)$ behavior shows a step-like increase at frequencies where $\varepsilon''(f)$ is a maximum. As T decreases below 52 K, another relaxation peak seems to appear at a higher frequency. This can be clearly seen on the Cole-Cole plot (figure 5.13) where $\varepsilon'(f)$ vs. $\varepsilon''(f)$ below 52 K shows a section of semicircle (at low frequency) with a tail at higher frequency. However, the peak at higher frequency in ε'' *vs.* f plot (figure 5.12, bottom panel) was not within our experimental window down to the lowest temperature measured, and only the low-frequency wing is visible.

Assuming a Debye-like dielectric relaxation, the broad peaks (steps) in the $\varepsilon''(f)$

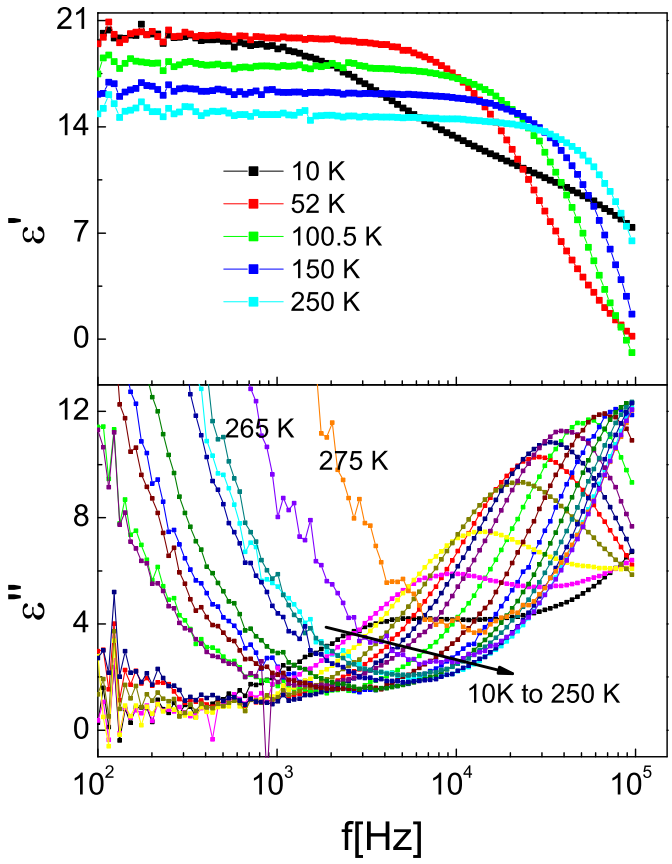

Figure 5.12: Real (top panel) and imaginary (bottom panel) parts of the dielectric constant ε of the 150 nm NMF/SRO film as a function of frequency f at different temperatures T.

($\varepsilon'(f)$) data indicate the existence of a distribution of relaxation times. In this case, $\varepsilon'(f)$ and $\varepsilon''(f)$ are expressed as 2.40 and 2.41 respectively. Using the Cole-Cole dispersion law [46],

$$\varepsilon(f) = \varepsilon_\infty + \frac{\Delta\varepsilon}{1 + (i2\pi f\tau_{\text{eff}})^\beta}, \tag{5.1}$$

where τ_{eff} is an effective characteristic relaxation time, ε_∞ is the dielectric permittivity at very high frequencies, $\Delta\varepsilon$ is the relaxation strength, and β ($0 < \beta \leq 1$) indicates the width of the relaxation time distribution ($\beta = 1$ corresponds to a Debye relaxation

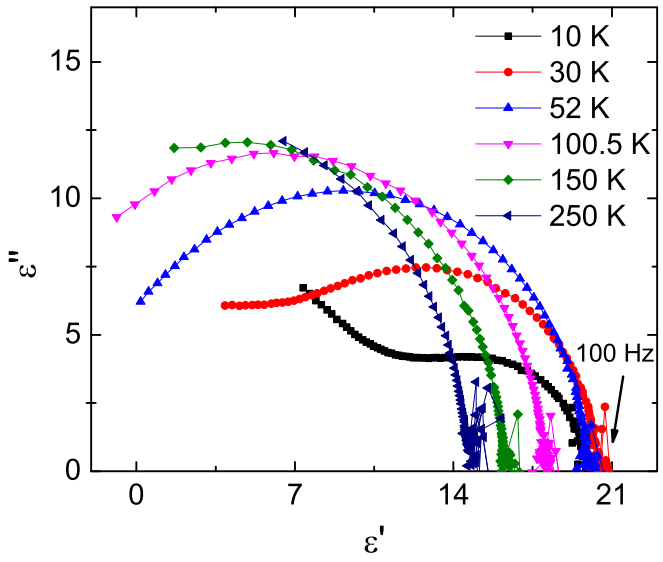

Figure 5.13: Cole-Cole plot: Real part of dielectric ε' vs. imaginary part of dielectric ε".

with a single relaxation time). The values of $\tau_{\text{eff}}(T)$, extracted from the position of the maximum of $\varepsilon''(f)$, $\tau_{\text{eff}} = (2\pi f_m)^{-1}$, are shown in figures 5.14 and 5.15. $\tau_{\text{eff}}(T)$ is fitted by an Arrhenius law,

$$\tau_{\text{eff}}(T) = \tau_0 \exp\left(\frac{-E_a}{kT}\right), \tag{5.2}$$

where k is Boltzmann's constant, τ_0 is the high temperature limit of dielectric relaxation time ($1/\tau_0$ is the attempted frequency), and E_a is activation energy, as seen in figure 5.14 (b). E_a, at a microscopic level, is the amount of energy required by the dipole to overcome the mean height of potential barrier in order to flip. The poor quality of fit to equation 5.2 shows a significant deviation in relaxation time from the Arrhenius law. This kind of non-Arrhenius law behavior of relaxation time suggests that the system has a high level of disorder in the structure and/or phase transformation such as in orientational glasses [135] and relaxor ferroelectrics [136].

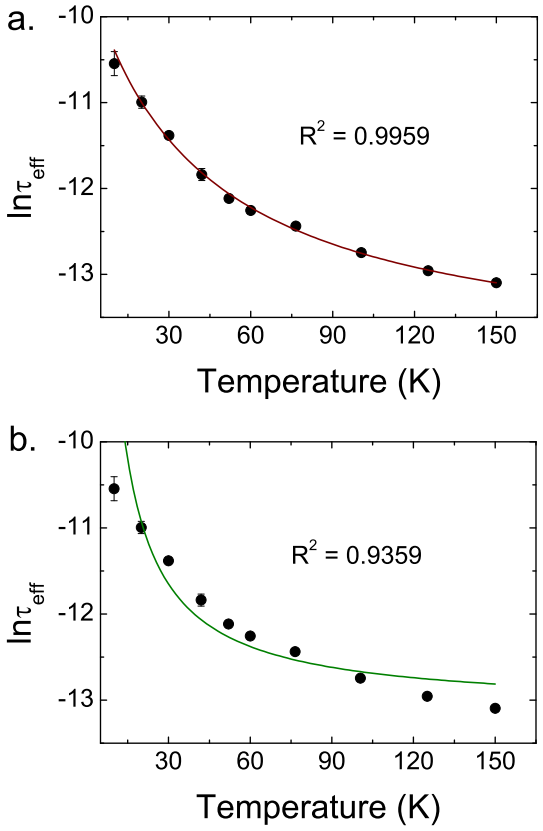

Figure 5.14: Dielectric relaxation time corresponding to the dielectric permittivity ε'' maximum as a function of temperature: black dots are data points and lines are fits corresponding to (a) Vogel-Fulcher law (wine curve) and (b) Arrhenius law (olive curve).

As a result, we employed a Vogel-Fulcher law applicable to typical relaxor FE,

$$\tau_{\text{eff}}(T) = \tau_0 \exp\left[\frac{-E_a}{k(T - T_f)}\right], \tag{5.3}$$

where T_f is the freezing temperature of the system, as seen in figure 5.14. When the system approaches the freezing temperature, there is gradual broadening in the relaxation spectrum. However, the fit to equation. 5.3 resulted in an unphysical negative value of the freezing temperature, T_f which indicates that the Vogel-Fulcher law is not valid for the temperature dependent relaxation time of the NMF/SRO thin

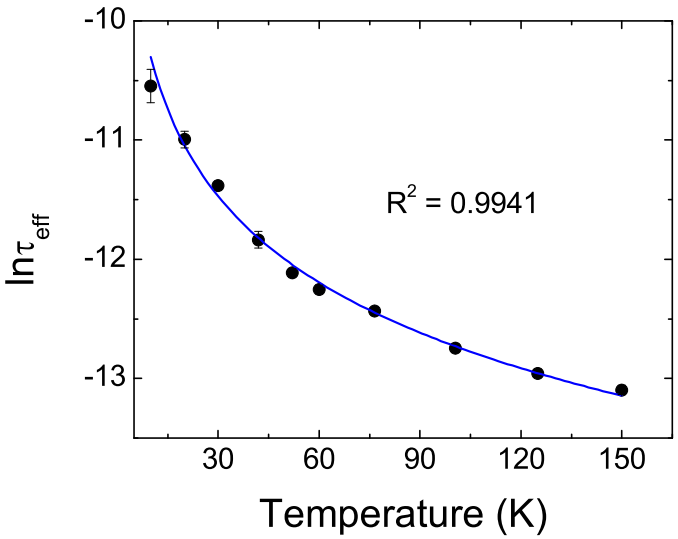

Figure 5.15: Dielectric relaxation time corresponding to the dielectric permittivity ε'' maximum as a function of temperature: black dots are data points, and the blue line is power law fit.

film system.

Interestingly, it was found that $\tau_{\text{eff}}(T)$ is described well by the power law equation

$$\tau_{\text{eff}}(T) = \tau_0 \left(\frac{T}{T_0} - 1 \right)^{\nu}. \tag{5.4}$$

The best fit (figure 5.15) yields $\nu = -0.90 \pm 0.07$, $\tau_0 = (2.8 \pm 1.5) \times 10^{-5}$ s, and a transition temperature $T_0 = 8$ K. The value of ν is close to $\nu = -1$ that describes

Table 5.1: Different parameters obtain after fitting the dielectric relaxation time as a function of temperature with corresponding models (left column).

	τ_0 [s]	E_a [eV]	T_f [K]	T_0 [K]	R^2
Arrhenius law	$(1.7 \pm 0.1) \times 10^{-6}$	$(5 \pm 0.4) \times 10^{-3}$			0.9358
Vogel-Fulcher law	$(8 \pm 1) \times 10^{-7}$	$(1.5 \pm 0.2) \times 10^{-2}$	-35 ± 6		0.9959
Power law	$(2.8 \pm 1.5) \times 10^{-5}$			8 ± 3	0.9941

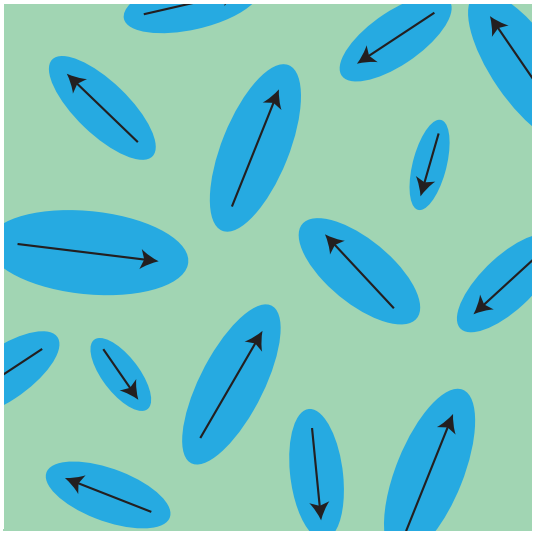

Figure 5.16: Schematic representation of "superparaelectric dipoles". Arrows represent total dipole moments of unit cells (or spins).

the divergence of the relaxation time for an order-disorder phase transition in the classical mean-field approximation [40]. The actual transition temperature could be much lower than 8 K because only the behavior for $T > T_0$ was observed. Table 5.1 summarizes the results of the fits of the data to the different models.

Interestingly, in canonical ferroelectrics the relaxation dynamics corresponding to order-disorder transition are typically observed in the GHz frequency range, indicating that relaxing dipolar entities are relatively large and slowly fluctuating microscopic regions spanning several unit cells. This observation confirms the presence of short-range dipolar order rather than long-range FE order. The local ordering of dipoles results in the formation of "superparaelectric dipoles" that extend over several unit cells and can be compared with polar nanoregions in relaxors (figure 5.16).

Chapter 6

Conclusions

In conclusion, we have successfully grown first-ever orthorhombic perovskite $NaMnF_3$ thin films on $SrTiO_3(001)$ single crystal using molecular beam epitaxy. The best film grew at substrate temperature $T_s = 250 - 300$ °C with twin domains. Domains with long axis (b) pointing in-plane and out-of-plane of the substrate were confirmed by off-axis $\theta - 2\theta$ and reciprocal space mapping. Previous computational work showed isotropic strain $a = c$ freezes soft ferroelectric mode driving the system through ferroelectric transition [11, 12]. However, both of the twin domains in the samples measured were confirmed to be orthorhombic. It was found that domain with the long axis pointing out-of-plane had a small compressive strain with $a/c \approx 1.035$ which close to one. The magnetic and piezoresponse force microscopy of the film confirm multiferroic order consistent with the computational prediction. In-plane SQUID magnetometry showed antiferromagnetic ordering at the Neel temperature T_N of 66 K. However, the splitting of ZFC-FC curves at the T_N and magnetization measurement as the function of magnetic field at 5 K showed that there is weak ferromagnetic

canting below the antiferromagnetic ordering temperature consistent with bulk magnetization measurement. Reproducible room temperature ferroelectric switching by voltage-biased scanning probe was detected with preferred up (out-of-plane) polarization using piezoresponse force microscopy. The preferred polarization is due to the presence of built-in field presumably due to interfacial effect with the substrate and electrical boundary condition at the surface of the film. An interesting 180° out-of-plane polarization flip by the application of an in-plane electric field was also observed which indicates the presence of an in-plane component of the polarization.

Dielectric and exchange bias measurements were performed on 150 nm of $NaMnF_3$ grown on 30 nm $SrRuO_3$ thin films. Magnetization measurement as a function of field at different temperatures showed negative exchange bias field with blocking temperature (T_B) close to 45 K. Dielectric spectroscopy indicated strong Debye-like relaxation contribution characterized by a distribution of relaxation time. Real and imaginary parts of dielectric permittivity showed broad peaks that shifted to a lower temperature similar to relaxor ferroelectrics. To better understand the relaxation dynamics, the values of characteristic relaxation time $\tau_{eff}(T)$, extracted from the position of the maximum of the imaginary part of dielectric permittivity, were fitted with Arrhenius, Vogel-Fulcher, and Power law. The quality of Arrhenius law fit was poor suggesting a high degree of disorder in the system. Usually, in such a case, characteristic relaxation time as a function of temperature can be fitted with Vogel-Fulcher law to obtain a freezing temperature of the relaxing polar entities. However, the fit of $\tau_{eff}(T)$ using Vogel-Fulcher resulted in an unphysical negative freezing temperature. Interestingly, $\tau_{eff}(T)$ is found to be well described by power law with ν, which mea-

sures the diffusiveness of a transition, close to one indicating the system goes through an order-disorder transition in classical mean-field approximation. The order-disorder transition temperature was found to be 8 K from the fit. This observation suggests the relaxing dipolar entities are slowly fluctuating microscopic regions spanning several unit cells which confirms short-range polar order rather than long-range ferroelectric order.

We have demonstrated the multiferrocity in our $NaMnF_3$ thin films grown on $SrTiO_3$. However, magnetoelectric coupling have yet to be demonstrated which will need further studies. The work in this thesis have shown that the perovskite fluorides are as interesting as oxides counterparts possibly with different functionalities. It is our hope that this work will inspire more research on perovskite fluorides.

Bibliography

[1] M. Fiebig. Revival of the magnetoelectric effect. Journal of Physics D: Applied Physics, 38(8):R123, 2005.

[2] W. Eerenstein, N.D. Mathur, and J. F. Scott. Multiferroic and magnetoelectric materials. Nature, 442(7104):759–765, 2006.

[3] S. Cherepov, P. Khalili Amiri, J. G. Alzate, K. Wong, M. Lewis, P. Upadhyaya, J. Nath, M. Bao, A. Bur, T. Wu, G. P. Carman, A. Khitun, and K. L. Wang. Electric-field-induced spin wave generation using multiferroic magnetoelectric cells. Applied Physics Letters, 104(8), 2014.

[4] S-W. Cheong and M. Mostovoy. Multiferroics: A magnetic twist for ferroelectricity. Nature materials, 6(1):13–20, 2007.

[5] P. Hayes, S. Salzer, J. Reermann, E. Yarar, V. Röbisch, A. Piorra, D. Meyners, M. Höft, R. Knöchel, G. Schmidt, et al. Electrically modulated magnetoelectric sensors. Applied Physics Letters, 108(18):182902, 2016.

[6] J. F. Scott and R. Blinc. Multiferroic magnetoelectric fluorides: Why are

there so many magnetic ferroelectrics? Journal of Physics: Condensed Matter, 23(11):113202, 2011.

[7] R. E. Cohen. Origin of ferroelectricity in perovskite oxides. Nature, 358(6382):136–138, 1992.

[8] J. Ravez. Ferroelectricity in solid state chemistry. Comptes Rendus de l'Académie des Sciences-Series IIc-Chemistry, 3(4):267–283, 2000.

[9] P. Borisov, T. A. Johnson, A. C. García-Castro, A. KC, D. Schrecongost, C. Cen, A. H. Romero, and D. Lederman. Multiferroic $BaCoF_4$ in thin film form: Ferroelectricity, magnetic ordering, and strain. ACS applied materials & interfaces, 8(4):2694–2703, 2016.

[10] A. Ratuszna, K. Majewska, and T. Lis. Structure of $NaMnF_3$ at room temperature. Acta Crystallographica Section C, 45(4):548–551, Apr 1989.

[11] A. C. Garcia-Castro, N. A. Spaldin, A. H. Romero, and E. Bousquet. Geometric ferroelectricity in fluoroperovskites. Phys. Rev. B, 89:104107, Mar 2014.

[12] A. C. Garcia-Castro, A. H. Romero, and E. Bousquet. Strain-engineered multiferroicity in *pnma* $NaMnF_3$ fluoroperovskite. Phys. Rev. Lett., 116:117202, Mar 2016.

[13] K. A. Müller and H. Burkard. $SrTiO_3$: An intrinsic quantum paraelectric below 4 K. Phys. Rev. B, 19:3593–3602, Apr 1979.

[14] J. Hemberger, P. Lunkenheimer, R. Viana, R. Böhmer, and A. Loidl. Electric-

field-dependent dielectric constant and nonlinear susceptibility in $SrTiO_3$. Phys. Rev. B, 52:13159–13162, Nov 1995.

[15] J. F. Scott. Ferroelectrics go bananas. Journal of Physics: Condensed Matter, 20(2):021001, 2007.

[16] N. A. Hill. Why are there so few magnetic ferroelectrics? The Journal of Physical Chemistry B, 104(29):6694–6709, 2000.

[17] C. Kittel. Introduction to solid state physics. Wiley, 2005.

[18] L. Kantorovich. Quantum theory of the solid state: An introduction, volume 136. Springer Science & Business Media, 2004.

[19] J. B. Ketterson. The Physics of Solids. Oxford University Press, 2016.

[20] A. H. Morrish et al. The physical principles of magnetism, volume 74. Wiley Online Library, 1965.

[21] E. O. Wollan and W. C. Koehler. Neutron diffraction study of the magnetic properties of the series of perovskite-type compounds [(1 - x)La, xCa]MnO_3. Physical Review, 100(2):545, 1955.

[22] C. G. Shull, W. A. Strauser, and E. O. Wollan. Neutron diffraction by paramagnetic and antiferromagnetic substances. Phys. Rev., 83:333–345, Jul 1951.

[23] I. Dzyaloshinsky. A thermodynamic theory of "weak" ferromagnetism of antiferromagnetics. Journal of Physics and Chemistry of Solids, 4(4):241–255, 1958.

[24] T. Moriya. Anisotropic superexchange interaction and weak ferromagnetism. Physical Review, 120(1):91, 1960.

[25] T. Moriya. Theory of magnetism of NiF_2. Physical Review, 117(3):635, 1960.

[26] W. H. Meiklejohn and C. P. Bean. New magnetic anisotropy. Phys. Rev., 102:1413–1414, Jun 1956.

[27] W. H. Meiklejohn. Exchange anisotropy-a review. Journal of Applied Physics, 33(3):1328–1335, 1962.

[28] J. Nogués and I. K. Schuller. Exchange bias. Journal of Magnetism and Magnetic Materials, 192(2):203 – 232, 1999.

[29] D. S. Geoghegan, P. G. McCormick, and R. Street. Mechanically alloyed antiferromagnetic-ferromagnetic exchange coupled nano-composites. In Mechanically Alloyed and Nanocrystalline Materials, volume 179 of Materials Science Forum, pages 629–634. Trans Tech Publications, 2 1995.

[30] W. H. Meiklejohn. Exchange anisotropy in the iron-iron oxide system. Journal of Applied Physics, 29(3):454–455, 1958.

[31] F. J. Darnell. Exchange anisotropy in oxidized iron-cobalt particles. Journal of Applied Physics, 32(3):S186–S187, 1961.

[32] H. Morita, H. Hiroyoshi, and K. Fukamichi. Field cooling effect on magnetic anisotropy of amorphous $Fe_{91.4}Zr_{86}$ alloy. Journal of Physics F: Metal Physics, 16(4):507, 1986.

[33] J Nogués, D. Lederman, T. J. Moran, I. K. Schuller, and K. V. Rao. Large exchange bias and its connection to interface structure in FeF_2-Fe bilayers. Applied Physics Letters, 68(22):3186–3188, 1996.

[34] B. Y. Wong, C. Mitsumata, S. Prakash, D. E. Laughlin, and T Kobayashi. Structural origin of magnetic biased field in NiMn/NiFe exchange coupled films. Journal of Applied Physics, 79(10):7896–7904, 1996.

[35] M. S. Lund, W. A. A. Macedo, K. Liu, J. Nogués, I. K. Schuller, and C. Leighton. Effect of anisotropy on the critical antiferromagnet thickness in exchange-biased bilayers. Phys. Rev. B, 66:054422, Aug 2002.

[36] R. E. Fontana Jr, B. A. Gurney, T. Lin, V. S. Speriosu, C. H. Tsang, and D. R. Wilhoit. Spin valve magnetoresistive sensor with antiparallel pinned layer and improved exchange bias layer, and magnetic recording system using the sensor, December 23 1997. US Patent 5,701,223.

[37] S. S. P. Parkin, K. P. Roche, M. G. Samant, P. M. Rice, R. B. Beyers, R. E. Scheuerlein, E. J. O'Sullivan, S. L. Brown, J. Bucchigano, D. W. Abraham, Y. Lu, M. Rooks, P. L. Trouilloud, R. A. Wanner, and W. J. Gallagher. Exchange-biased magnetic tunnel junctions and application to nonvolatile magnetic random access memory (invited). Journal of Applied Physics, 85(8):5828–5833, 1999.

[38] V. Wadhawan. Introduction to ferroic materials. CRC press, 2000.

[39] J. Valasek. Piezo-electric and allied phenomena in rochelle salt. Physical review, 17(4):475, 1921.

[40] M. E. Lines and A. M. Glass. Principles and applications of ferroelectrics and related materials. Claredon Press, Oxford, 2004.

[41] D. Fu and M. Itoh. Role of Ca off-centering in tuning ferroelectric phase transitions in $Ba(Zr,Ti)O_3$ system. In Aime Pelaiz Barranco, editor, Ferroelectric Materials - Synthesis and Characterization, chapter 05. InTech, Rijeka, 2015.

[42] A. A. Bokov and Z-G. Ye. Dielectric relaxation in relaxor ferroelectrics. Journal of Advanced dielectrics, 2(02):1241010, 2012.

[43] H. Fröhlich. Theory of dielectrics. Mono. Phys. Chem. Mater. Clarendon Press, Oxford, 1949.

[44] Agilent Application Note. Agilent basics of measuring the dielectric properties of materials. Agilent Literature Number, 2006.

[45] K. S. Cole and R. H. Cole. Dispersion and absorption in dielectrics I. Alternating current characteristics. The Journal of chemical physics, 9(4):341–351, 1941.

[46] F. Kremer and A. Schönhals, editors. Broadband Dielectric Spectroscopy. Springer, Berlin, Heidelberg, 2003.

[47] M. A. Herman and H. Sitter. Molecular beam epitaxy: Fundamentals and current status, volume 7. Springer Science & Business Media, 2012.

[48] M. Rodahl, F. Höök, A. Krozer, P. Brzezinski, and B. Kasemo. Quartz crystal microbalance setup for frequency and Q-factor measurements in gaseous and liquid environments. Review of Scientific Instruments, 66(7):3924–3930, 1995.

[49] R. Eason. Pulsed laser deposition of thin films: Applications-led growth of functional materials. John Wiley & Sons, 2007.

[50] D. Bäuerle. Thermal, Photophysical, and Photochemical Processes, pages 13–38. Springer Berlin Heidelberg, Berlin, Heidelberg, 2011.

[51] M. Stafe, A. Marcu, and N. N. Puscas. Introduction, pages 1–13. Springer Berlin Heidelberg, Berlin, Heidelberg, 2014.

[52] C. L. Chen, Y. Cao, Z. J. Huang, Q. D. Jiang, Z. Zhang, Y. Y. Sun, W. N. Kang, L. M. Dezaneti, W. K. Chu, and C. W. Chu. Epitaxial $SrRuO_3$ thin films on (001) $SrTiO_3$. Applied Physics Letters, 71(8):1047–1049, 1997.

[53] X. D. Wu, S. R. Foltyn, R. C. Dye, Y. Coulter, and R. E. Muenchausen. Properties of epitaxial $SrRuO_3$ thin films. Applied Physics Letters, 62(19):2434–2436, 1993.

[54] G. S. May and C. J. Spanos. Fundamentals of semiconductor manufacturing and process control. John Wiley & Sons, 2006.

[55] W. Braun. Applied RHEED: Reflection high-energy electron diffraction during crystal growth, volume 154. Springer Science & Business Media, 1999.

[56] P. Eaton and P. West. Atomic force microscopy. Oxford University Press, 2010.

[57] A. Gibaud and S. Hazra. X-ray reflectivity and diffuse scattering. Current Science, pages 1467–1477, 2000.

[58] M. Björck and G. Andersson. *GenX*: An extensible X-ray reflectivity refinement program utilizing differential evolution. Journal of Applied Crystallography, 40(6):1174–1178, Dec 2007.

[59] J. Clarke and A. I. Braginski. The SQUID Handbook: Applications of SQUIDs and SQUID Systems. John Wiley & Sons, 2006.

[60] J. Clarke. SQUIDs. Scientific American, 271(2):46–53, 1994.

[61] B. D. Cullity and C. D. Graham. Introduction to magnetic materials. John Wiley & Sons, 2011.

[62] D. A. Hall, M. Cain, M. Stewart, Teddington (United Kingdom). Centre for Materials Measurement National Physical Lab., and Technology. Ferroelectric hysteresis measurement & analysis. In Minutes of the NPL CAM7 IAG Meeting, 1998.

[63] J. T. Evans. Characterizing ferroelectric materials. In Proc. IEEE ISAF, pages 1–123, 2011.

[64] C. B. Sawyer and C. H. Tower. Rochelle salt as a dielectric. Physical review, 35(3):269, 1930.

[65] A. F. Devonshire. Theory of ferroelectrics. Advances in physics, 3(10):85–130, 1954.

[66] A. Gruverman, S. V. Kalinin, et al. Piezoresponse force microscopy and recent advances in nanoscale studies of ferroelectrics. Journal of Materials Science, 41(1):107–116, 2006.

[67] R. Proksch and S. Kalinin. Piezoresponse force microscopy with asylum research AFMs. PFM App Note, 2008.

[68] H. Unoki and T. Sakudo. Electron spin resonance of Fe^{3+} in $SrTiO_3$ with special reference to the 110 K phase transition. Journal of the Physical Society of Japan, 23(3):546–552, 1967.

[69] G. Shirane and Y. Yamada. Lattice-dynamical study of the 110 K phase transition in $SrTiO_3$. Physical Review, 177(2):858, 1969.

[70] K. A. Müller and H. Burkard. $SrTiO_3$: An intrinsic quantum paraelectric below 4 K. Physical Review B, 19(7):3593, 1979.

[71] P. A. Fleury and J. M. Worlock. Electric-field-induced raman scattering in $SrTiO_3$ and $KTaO_3$. Physical Review, 174(2):613, 1968.

[72] J. Hemberger, P. Lunkenheimer, R. Viana, R. Böhmer, and A. Loidl. Electric-field-dependent dielectric constant and nonlinear susceptibility in $SrTiO_3$. Physical Review B, 52(18):13159, 1995.

[73] T. Mitsui and W. B. Westphal. Dielectric and X-ray studies of $Ca_xBa_{1-x}TiO_3$ and $Ca_xSr_{1-x}TiO_3$. Physical Review, 124(5):1354, 1961.

[74] W. J. Burke and R. J. Pressley. Stress induced ferroelectricity in $SrTiO_3$. Solid State Communications, 9(3):191–195, 1971.

[75] R. Uecker, R. Bertram, M. Brützam, Z. Galazka, T. M. Gesing, C. Guguschev, D. Klimm, M. Klupsch, A. Kwasniewski, and D. G. Schlom. Large-lattice-parameter perovskite single-crystal substrates. Journal of Crystal Growth, 457:137–142, 2017.

[76] A. Ohtomo and H. Y. Hwang. A high-mobility electron gas at the $LaAlO_3/SrTiO_3$ heterointerface. Nature, 427(6973):423–426, 2004.

[77] M. Kawasaki, K. Takahashi, T. Maeda, R. Tsuchiya, M. Shinohara, O. Ishiyama, T. Yonezawa, M. Yoshimoto, and H. Koinuma. Atomic control of the $SrTiO_3$ crystal surface. Science, 266(5190):1540–1542, 1994.

[78] M. Kareev, S. Prosandeev, J. Liu, C. Gan, A. Kareev, J. W. Freeland, M. Xiao, and J. Chakhalian. Atomic control and characterization of surface defect states of TiO_2 terminated $SrTiO_3$ single crystals. Applied Physics Letters, 93(6):061909, 2008.

[79] J. G. Connell, B. J. Isaac, G. B. Ekanayake, D. R. Strachan, and S. S. A. Seo. Preparation of atomically flat $SrTiO_3$ surfaces using a deionized-water leaching and thermal annealing procedure. Applied Physics Letters, 101(25), 2012.

[80] J. H. Ngai, T. C. Schwendemann, A. E. Walker, Y. Segal, F. J. Walker, E. I. Altman, and C. H. Ahn. Achieving A-site termination on $La_{0.18}Sr_{0.82}Al_{0.59}Ta_{0.41}O_3$ substrates. Advanced Materials, 22(26-27):2945–2948, 2010.

[81] J. M. D. Coey, M. Venkatesan, and P. Stamenov. Surface magnetism of strontium titanate. Journal of Physics: Condensed Matter, 28(48):485001, 2016.

[82] W. Kleemann, J. Dec, Y. G. Wang, P Lehnen, and S. A. Prosandeev. Phase transitions and relaxor properties of doped quantum paraelectrics. Journal of Physics and Chemistry of Solids, 61(2):167 – 176, 2000.

[83] C. Ang, Z. Yu, P. M. Vilarinho, and J. L. Baptista. Bi:$SrTiO_3$: A quantum ferroelectric and a relaxor. Physical Review B, 57(13):7403, 1998.

[84] H. W. Jang, A. Kumar, S. Denev, M. D. Biegalski, P. Maksymovych, C. W. Bark, C. T. Nelson, C. M. Folkman, S. H. Baek, N. Balke, C. M. Brooks, D. A. Tenne, D. G. Schlom, L. Q. Chen, X. Q. Pan, S. V. Kalinin, V. Gopalan, and C. B. Eom. Ferroelectricity in strain-free $SrTiO_3$ thin films. Phys. Rev. Lett., 104:197601, May 2010.

[85] G. A. Samara. The relaxational properties of compositionally disordered ABO_3 perovskites. Journal of Physics: Condensed Matter, 15(9):R367, 2003.

[86] G. A. Samara and L. A. Boatner. Ferroelectric-to-relaxor crossover and oxygen vacancy hopping in the compositionally disordered perovskites $KTa_{1-x}Nb_xO_3$:Ca. Phys. Rev. B, 61:3889–3896, Feb 2000.

[87] H. Uwe, K. B. Lyons, H. L. Carter, and P. A. Fleury. Ferroelectric microregions and raman scattering in $KTaO_3$. Phys. Rev. B, 33:6436–6440, May 1986.

[88] J. J. van der Klink, S. Rod, and A. Chtelain. Local properties, long-range order, and quantum ferroelectricity in $KTa_{1-x}Nb_xO_3$. Phys. Rev. B, 33:2084–2087, Feb 1986.

[89] L. G. Tejuca and J. L. G. Fierro. Properties and applications of perovskite-type oxides. CRC Press, 2000.

[90] C. Zener. Interaction between the *d*-shells in the transition metals. II. Ferromagnetic compounds of manganese with perovskite structure. Phys. Rev., 82:403–405, May 1951.

[91] R. Haumont, J. Kreisel, and P. Bouvier. Raman scattering of the model multiferroic oxide $BiFeO_3$: effect of temperature, pressure and stress. Phase Transitions, 79(12):1043–1064, 2006.

[92] J. Wang, J. B. Neaton, H. Zheng, V. Nagarajan, S. B. Ogale, B. Liu, D. Viehland, V. Vaithyanathan, D. G. Schlom, U. V. Waghmare, N. A. Spaldin, K. M. Rabe, M. Wuttig, and R. Ramesh. Epitaxial $BiFeO_3$ multiferroic thin film heterostructures. Science, 299(5613):1719–1722, 2003.

[93] Y. M. Chiang, G. W. Farrey, and A. N. Soukhojak. Lead-free high-strain single-crystal piezoelectrics in the alkaline-bismuth-titanate perovskite family. Applied Physics Letters, 73(25):3683–3685, 1998.

[94] J. B. Torrance, P. Lacorre, A. I. Nazzal, E. J. Ansaldo, and Ch. Niedermayer. Systematic study of insulator-metal transitions in perovskites $r\mathrm{NiO}_3$ (R=Pr, Nd, Sm, Eu) due to closing of charge-transfer gap. Phys. Rev. B, 45:8209–8212, Apr 1992.

[95] A. M. Glazer. The classification of tilted octahedra in perovskites.

Acta Crystallographica Section B: Structural Crystallography and Crystal Chemistry, 28(11):3384–3392, 1972.

[96] A. M. Glazer. Simple ways of determining perovskite structures. Acta Crystallographica Section A: Crystal Physics, Diffraction, Theoretical and General Crystallography, 31(6):756–762, 1975.

[97] N. A. Benedek and C. J. Fennie. Why are there so few perovskite ferroelectrics? The Journal of Physical Chemistry C, 117(26):13339–13349, 2013.

[98] W. Zhong, D. Vanderbilt, and K. M. Rabe. First-principles theory of ferroelectric phase transitions for perovskites: The case of $BaTiO_3$. Phys. Rev. B, 52:6301–6312, Sep 1995.

[99] D. Babel. Structural chemistry of octahedral fluorocomplexes of the transition elements, pages 1–87. Springer Berlin Heidelberg, Berlin, Heidelberg, 1967.

[100] S. J. Pickart, H. A. Alperin, and R. Nathans. Magnetic structure of binary fluorides containing Mn^{2+}. Journal de Physique, 25(5):565–566, 1964.

[101] J. R. Shane, D. H. Lyons, and M. Kestigian. Antiferromagnetic resonance in $NaMnF_3$. Journal of Applied Physics, 38(3):1280–1282, 1967.

[102] D. T. Teaney, J. S. Blackburn, and R. W. H. Stevenson. Antiferromagnetic resonance of three $XMnF_3$ single crystals. Bull. Am. Phys. Soc., 7:201, 1962.

[103] P. Daniel, M. Rousseau, A. Desert, A. Ratuszna, and F. Ganot. Raman scattering study and lattice-dynamics investigation of the $NaMnF_3$ perovskite. Phys. Rev. B, 51:12337–12346, May 1995.

[104] E. E. Carpenter, C. Sangregorio, and C. J. O'connor. Synthesis of antiferromagnetic macromolecular particles. Molecular Crystals and Liquid Crystals Science and Technology. Section A. Molecular Crystals and Liquid Crystals, 334(1):641–649, 1999.

[105] Y. P. Du, Y. W. Zhang, Z. G. Yan, L. D. Sun, S. Gao, and C. H. Yan. Single-crystalline and near-monodispersed NaMF$_3$ (M = Mn, Co, Ni, Mg) and LiMAlF$_6$ (M = Ca, Sr) nanocrystals from cothermolysis of multiple trifluoroacetates in solution. Chemistry-An Asian Journal, 2(8):965–974, 2007.

[106] J. B Nelson and D. P. Riley. An experimental investigation of extrapolation methods in the derivation of accurate unit-cell dimensions of crystals. Proceedings of the Physical Society, 57(3):160, 1945.

[107] S. S. Kim, T. S. Kang, and J. H. Je. Structural evolution of epitaxial $SrRuO_3$ thin films grown on $SrTiO_3$(001). Journal of Applied Physics, 90(9):4407–4410, 2001.

[108] X. Martí, F. Sánchez, V. Skumryev, V. Laukhin, C. Ferrater, M. V. García-Cuenca, M. Varela, and J. Fontcuberta. Crystal texture selection in epitaxies of orthorhombic antiferromagnetic $YMnO_3$ films. Thin Solid Films, 516(15):4899 – 4907, 2008.

[109] C. J. M. Daumont, D. Mannix, S. Venkatesan, G. Catalan, D. Rubi, B. J. Kooi, J. T. M. D. Hosson, and B. Noheda. Epitaxial $TbMnO_3$ thin films on $SrTiO_3$ substrates: a structural study. Journal of Physics: Condensed Matter, 21(18):182001, 2009.

[110] J. Scola, P. Boullay, W. Noun, E. Popova, Y. Dumont, A. Fouchet, and N. Keller. Microstructure and self-exchange coupling in a $YFeO_3$ film. Journal of Applied Physics, 110(4), 2011.

[111] C. Leighton, J. Nogués, H. Suhl, and I. K. Schuller. Competing interfacial exchange and zeeman energies in exchange biased bilayers. Phys. Rev. B, 60:12837–12840, Nov 1999.

[112] M. Yang, A. KC, A. C. Garcia-Castro, P. Borisov, E. Bousquet, D. Lederman, A. H. Romero, and C. Cen. Room temperature ferroelectricity in fluoroperovskite thin films. Scientific Reports, 7(1):7182, 2017.

[113] M. D. Glinchuk, E. A. Eliseev, and A. N. Morozovska. Influence of built-in internal electric field on ferroelectric film properties and phase diagram. Ferroelectrics, 354(1):86–98, 2007.

[114] N. Tayebi, S. Kim, R. J. Chen, Q. Tran, N. Franklin, Y. Nishi, Q. Ma, and V. Rao. Tuning the built-in electric field in ferroelectric $Pb(Zr_{0.2}Ti_{0.8})O_3$ films for long-term stability of single-digit nanometer inverted domains. Nano Letters, 12(11):5455–5463, 2012. PMID: 23043427.

[115] Y. Liu, X. Lou, M. Bibes, and B. Dkhil. Effect of a built-in electric field in asymmetric ferroelectric tunnel junctions. Phys. Rev. B, 88:024106, Jul 2013.

[116] C. Lichtensteiger, C. Weymann, S. Fernandez-Pena, P. Paruch, and J.-M. Triscone. Built-in voltage in thin ferroelectric $PbTiO_3$ films: the effect of electrostatic boundary conditions. New Journal of Physics, 18(4):043030, 2016.

[117] C. Lichtensteiger, S. Fernandez-Pena, C. Weymann, P. Zubko, and J.-M. Triscone. Tuning of the depolarization field and nanodomain structure in ferroelectric thin films. Nano Letters, 14(8):4205–4211, 2014. PMID: 24983128.

[118] M. Stengel, D. Vanderbilt, and N. A. Spaldin. Enhancement of ferroelectricity at metal–oxide interfaces. Nature Materials, 8:392 EP –, 04 2009.

[119] Z. Chen, X. Zou, W. Ren, L. You, C. Huang, Y. Yang, P. Yang, J. Wang, T. Sritharan, L. Bellaiche, and L. Chen. Study of strain effect on in-plane polarization in epitaxial $BiFeO_3$ thin films using planar electrodes. Phys. Rev. B, 86:235125, Dec 2012.

[120] N. Balke, M. Gajek, A. K. Tagantsev, L. W. Martin, R. Chu, Y.-H.and Ramesh, and S. V. Kalinin. Direct observation of capacitor switching using planar electrodes. Advanced Functional Materials, 20(20):3466–3475, 2010.

[121] S. Y. Yang, J. Seidel, S. J. Byrnes, P. Shafer, C.-H. Yang, M. D. Rossell, P. Yu, Y.-H. Chu, J. F. Scott, J. W. Ager III, L. W. Martin, and R. Ramesh. Above-bandgap voltages from ferroelectric photovoltaic devices. Nature Nanotechnology, 5:143 EP –, 01 2010.

[122] P. Zubko, S. Gariglio, M Gabay, P Ghosez, and J.-M. Triscone. Interface physics in complex oxide heterostructures. Annual Review of Condensed Matter Physics, 2(1):141–165, 2011.

[123] K.-J. Jin, H.-B. Lu, K. Zhao, C. Ge, M. He, and G.-Z. Yang. Novel multifunc-

tional properties induced by interface effects in perovskite oxide heterostructures. Advanced Materials, 21(45):4636–4640, 2009.

[124] P. B. Allen, H. Berger, O. Chauvet, L. Forro, T. Jarlborg, A. Junod, B. Revaz, and G. Santi. Transport properties, thermodynamic properties, and electronic structure of $SrRuO_3$. Phys. Rev. B, 53:4393–4398, Feb 1996.

[125] C. W. Jones, P. D. Battle, P. Lightfoot, and W. T. A. Harrison. The structure of $SrRuO_3$ by time-of-flight neutron powder diffraction. Acta Crystallographica Section C: Crystal Structure Communications, 45(3):365–367, 1989.

[126] A. Callaghan, C. W. Moeller, and R. Ward. Magnetic interactions in ternary ruthenium oxides. Inorganic Chemistry, 5(9):1572–1576, 1966.

[127] C. B. Eom, R. J. Cava, R. M. Fleming, J. M. Phillips, R. B. Van Dover, J. H. Marshall, J. W. P. Hsu, and J. J. Krajewski. Single-crystal epitaxial thin films of the isotropic metallic oxides $Sr_{1-x}Ca_xRuO_3$ ($0 \leq x \leq 1$). Science, 258:11, 1992.

[128] M. Naito, H. Yamamoto, and H. Sato. Reflection high-energy electron diffraction and atomic force microscopy studies on homoepitaxial growth of $SrTiO_3$(001). Physica C: Superconductivity, 305(3):233 – 250, 1998.

[129] G. Koster, L. Klein, W. Siemons, G. Rijnders, J. S. Dodge, C.-B. Eom, D. H. A. Blank, and M. R. Beasley. Structure, physical properties, and applications of $SrRuO_3$ thin films. Rev. Mod. Phys., 84:253–298, Mar 2012.

[130] Yukio Watanabe. Electrical transport through $Pb(Zr,Ti)O_3$ p-n and p-p heterostructures modulated by bound charges at a ferroelectric surface: Ferroelectric p-n diode. Phys. Rev. B, 59:11257–11266, May 1999.

[131] Y Watanabe. Reproducible memory effect in the leakage current of epitaxial ferroelectric/conductive perovskite heterostructures. Applied Physics Letters, 66(1):28–30, 1995.

[132] B. Martínez, X. Obradors, Ll. Balcells, A. Rouanet, and C. Monty. Low temperature surface spin-glass transition in γ-Fe_2O_3 nanoparticles. Phys. Rev. Lett., 80:181–184, Jan 1998.

[133] C. Ostos, O. Raymond, N. Suarez-Almodovar, D. Bueno-Baqués, Mestres. L., and J. M. Siqueiros. Highly textured Sr, Nb co-doped $BiFeO_3$ thin films grown on $SrRuO_3$/Si substrates by rf-sputtering. Journal of Applied Physics, 110(2):024114, 2011.

[134] G. A. Samara. The relaxational properties of compositionally disordered ABO_3 perovskites. Journal of Physics: Condensed Matter, 15(9):R367, 2003.

[135] U. T. Höchli, K. Knorr, and A. Loidl. Orientational glasses. Advances in Physics, 39(5):405–615, 1990.

[136] A. E. Glazounov and A. K. Tagantsev. Direct evidence for Vögel-Fulcher freezing in relaxor ferroelectrics. Applied Physics Letters, 73(6):856–858, 1998.

[137] A. A. Bokov and Z.-G. Ye. Recent progress in relaxor ferroelectrics with perovskite structure. Journal of Materials Science, 41(1):31–52, 2006.